

論文 / 著書情報
Article / Book Information

題目(和文)	
Title(English)	Design and Magnetic Characterization of L10-FePt Based Nano-heterostructures
著者(和文)	GAOTENGHUA
Author(English)	Tenghua Gao
出典(和文)	学位:博士(工学), 学位授与機関:東京工業大学, 報告番号:甲第10304号, 授与年月日:2016年9月20日, 学位の種別:課程博士, 審査員:史蹟,中村 吉男,村石 信二,三宮 工,中川 茂樹
Citation(English)	Degree:., Conferring organization: Tokyo Institute of Technology, Report number:甲第10304号, Conferred date:2016/9/20, Degree Type:Course doctor, Examiner:,,,,,
学位種別(和文)	博士論文
Type(English)	Doctoral Thesis

**Design and Magnetic Characterization of L1₀-FePt
Based Nano-heterostructures**

Tenghua GAO

Doctoral Dissertation

Directed by: Prof. Yoshio NAKAMURA

Prof. Ji SHI

**Department of Metallurgy and Ceramics Science
Tokyo Institute of Technology**

August, 2016

Preface

$L1_0$ FePt has drawn a considerable research interest as a potential candidate for perpendicular recording system due to its high magnetocrystalline anisotropy. The corresponding value is $7 \times 10^6 \text{ J/m}^3$ with its easy axis along c axis. However, compared with single layer material, interface phenomena originated from heterostructures plays a more important role in modern information technology. Moreover, the challenges involved in understanding the physics behind the interface phenomena have made it become a promising area for both theoreticians and experimentalists.

In this work, the structural and magnetic interaction in $L1_0$ FePt based nano-heterostructures has been studied. For structural interaction, we investigated the effect of the interfaces and strain/stress in ultrathin FePt layer using FePt/AlN multilayer structure. In order to study the coupling at ferromagnetic (FM)/antiferromagnetic (AFM) interface, we have designed and fabricated perpendicular exchange biased FePt/NiO bilayer structure and “naturally” 90° FM interlayer coupled FePt/NiO/FePt trilayer structure. With the assistance of strong uniaxial magnetic anisotropy in ordered FePt, the coupling configuration at FM/AFM interface has been investigated through different experimental approaches. Based on our results, we find that the angle between FM and AFM spin at interface is not exact 90° , which may unravel the origin of exchange bias in coupled FM/AFM structure with compensated AFM interface.

Contents

Preface	i
Contents	ii
Chapter 1 Introduction	1
1.1 Magnetic recording technologies	1
1.1.1 Fundamental magnetism of magnetic recording media.....	2
1.1.1.1 Signal to noise ratio (<i>SNR</i>).....	2
1.1.1.2 Thermal limit	3
1.1.2 Chemically ordered L1 ₀ FePt media and corresponding study	4
1.1.2.1 Basic knowledge on FePt ordering phase transformation.....	4
1.1.2.2 Role of composition on ordering transformation in FePt thin film near the equiatomic ratio.....	7
1.1.2.3 Dimensional dependence of FePt ordering phase transformation	8
1.2 Read head associated ferromagnetic-antiferromagnetic interaction	10
1.2.1 The AFM domain wall parallel to the ferromagnetic/antiferromagnetic interfaces ³¹	11
1.2.2 Random field arising from interface roughness in ferromagnetic/ antiferromagnetic structure.....	13
1.2.3 Ferromagnetic/antiferromagnetic interfacial interaction at compensated antiferromagnetic interfaces	16
1.3 Objectives of this study	19
1.4 Organization of this thesis.....	20
Chapter 2 Preparation and characterization of L1₀ FePt based ultrathin structures	25
2.1 Preparation of L1 ₀ FePt based ultrathin structures.....	25
2.2 Structural characterization.....	28
2.2.1 Conventional and Grazing incidence in-plane x-ray diffraction	28
2.2.2 Selected-area diffraction patterns	29
2.3 Crystal and magnetic structure of NiO.....	32

2.4 Magnetic characterization	33
2.4.1 Vibrating sample magnetometer.....	33
2.4.2 Superconducting quantum interference device (SQUID) magnetometer....	34
2.4.3 Magnetic force microscopy (MFM)	35
Chapter 3 Effect of nitrogen upon structural and magnetic properties of FePt in FePt/AlN multilayer structures	38
3.1 Introduction	38
3.2 Fabrication of FePt/AlN multilayer films	39
3.3 Structural characterization.....	40
3.3.1 X-ray reflectivity (XRR) patterns.....	40
3.3.2 Conventional XRD profiles	41
3.3.3 Determination of in-plane strain in FePt layer	42
3.3.4 Effect of in-plane strain on FePt (111) texture	44
3.3.5 Grazing incidence in-plane XRD profiles	45
3.3.6 Calculation of long range order parameter S	46
3.4 Magnetic properties of FePt/AlN multilayer films	49
3.4.1 Annealing temperature dependence of coercivity and degree of FePt order in FePt/AlN multilayer films	49
3.4.2 Effect of nitrogen on magnetic properties for FePt layer in FePt/AlN multilayer films	51
3.5 Summary	55
Chapter 4 Off-easy-plane antiferromagnetic spin canting in coupled FePt/NiO bilayer structure with perpendicular exchange bias	58
4.1 Introduction	58
4.2 Preparation of FePt/NiO bilayer structure on MgO(001) single crystal substrate	60
4.3 Determination of crystallographic orientation of FePt/NiO bilayer structure....	61
4.3.1 Preferred growth orientation and chemical order in FePt layer.....	61
4.3.2 In-plane crystallographic orientation of FePt/NiO bilayer structure and the cross-section TEM image	62
4.3.3 Further confirmation of in-plane epitaxial relationship.....	63

4.4 Discussions on the relationship between the magnetic structure of NiO and epitaxial strain	64
4.5 Magnetic hysteresis loops and initial magnetization curves	65
4.6 Magnetic domain imaging.....	67
4.7 Proposed interfacial AFM spin of NiO canting mechanism	68
4.8 Calculation of stripe domain width in ultrathin FePt layer	70
4.9 Summary	72
Chapter 5 Field cooling driven magnetic anisotropy and stripe domain evolution in FePt/NiO/FePt trilayer structure	76
5.1 Introduction	76
5.2 Details on FePt/NiO/FePt trilayer structure preparation	78
5.3 Structural characterization.....	79
5.3.1 X-ray diffraction profiles.....	79
5.3.2 X-ray diffraction 180° ϕ -scan plots	81
5.4 Magnetic hysteresis loops	83
5.4.1 Out-of-plane Magnetic hysteresis loops.....	83
5.4.2 In-plane magnetic hysteresis loops for FePt _{tp} /NiO/FePt _{tp} structure.....	84
5.4.3 In-plane magnetic hysteresis loops for FePt _{oop} /NiO/FePt _{tp} structure	86
5.5 Discussions on interfacial FM/AFM coupling configuration	88
5.6 Magnetic domain imaging for FePt _{oop} /NiO/FePt _{tp} structure	91
5.7 Summary	93
Chapter 6 Conclusions.....	98
6.1 The FePt/AlN multilayer structure	98
6.2 The FePt/NiO bilayer structure	99
6.3 FePt/NiO/FePt trilayer structure.....	100
Publications	102
Acknowledgements	104

Chapter 1 Introduction

1.1 Magnetic recording technologies

Magnetic storage is an extremely important technology, which is widely used to store computer data as well as audio and video signals and has become a necessity in our daily life. The history of magnetic storage could be dated to its invention by Valdemar Poulsen more than hundred years ago.¹ In 1956 the first magnetic hard disk drive (HDD) was invented featuring a total storage capacity of 5 MB at a recording density of 2 Kbit/in².² From then on, HDD went on its historical stage as a dominate

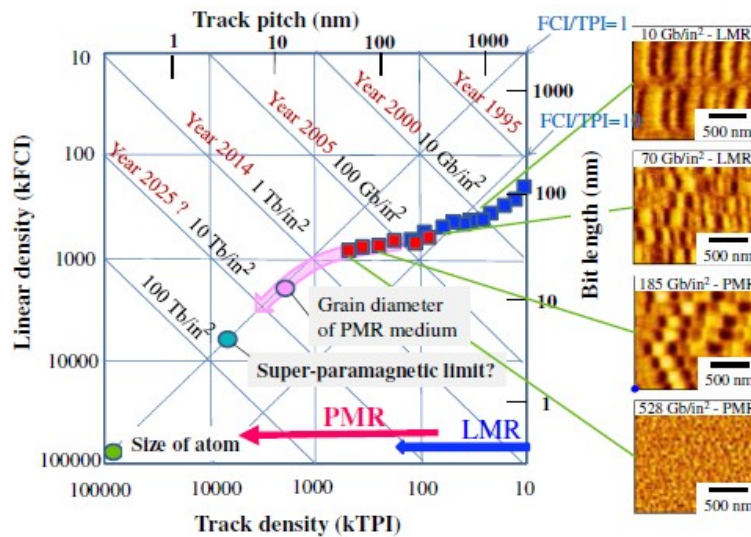


FIG 1-1 Development of areal density and decreasing trend of bit size in hard disk drives.³

device for external storage of data, primarily used in computers, until nowadays. In the quest to maintain this position and keep pace with the requirement of external storage, the areal density of HDD has been increasing at 25-35% per year with decreasing the bit size (see Fig 1-1).³ In the year of 2011, Toshiba has claimed a

recording density of 744Gb/in², and the pursuit of higher areal densities will still continue.

However, continued growth in areal density is suffering from a bottleneck limited by superparamagnetic effect in modern recording media. In order to push further out the confining limitation of media thermal instabilities, some significant improvements of the recording media have been achieved by using new thin film materials or architectures, for instance, antiferromagnetically coupled (AFC) media,^{4,5} perpendicular⁶ and thermal assisted recording (TAR)⁷ *et al.*

1.1.1 Fundamental magnetism of magnetic recording media

1.1.1.1 Signal to noise ratio (SNR)

SNR is a measure of the read back voltage strength relative to the background noise, and is one of important parameters determining the error rate of HDD systems and limiting the final areal density. For current HDD system, media noise is a dominate effect on the SNR, which is mainly composed of DC noise and transition noise. The DC noise is directly caused by the granularity of the media. It produces a variable magnetization and signal amplitude with different grain diameter and grain orientation. The transition noise is generated by the transition region and increases linearly with the transition density, which is mainly determined by intergranular exchange coupling and magnetostatic interaction.

SNR can be roughly estimated by the equation below,⁸ which is valid only for uncorrelated noise:

$$SNR \approx \frac{0.31PW_{50}BW_{read}}{\alpha^2 D(1+\sigma^2)} \approx \frac{B^2W_{read}}{\alpha^2 D^3(1+\sigma^2)} \quad (1.1)$$

Where $PW_{50}/B = 3$, $\alpha = \alpha/D$;⁹ σ is the normalized grain size distribution width and W_{read} is the read width of the head; a is the transition parameter, characterizing the magnetic width of the transitions. From Eq (1.1), it is clearly seen that SNR is inversely proportional to the 3rd power of grain diameter D . Therefore, by reducing the grain diameter, SNR can be significantly improved.

1.1.1.2 Thermal limit

To reduce the grain volume in the scaling process, the magnetization of grains will become unstable because of thermal fluctuation. As a consequence, the magnetization decays with time, which may cause data loss. This phenomenon, also referred to as superparamagnetic effect, is realized important to achieve higher recording densities in HDD products.

As the weak intergranular exchange coupling, the longitudinal recording medium can be approximated formed by independent particles. Thus, the following simple model can describe these thermal effects. The energy barrier for magnetization reversal with an external magnetic field is given by the equation below²

$$E(H, V) = K_u V \left(1 - \frac{H}{H_0}\right)^n \quad (1.2)$$

K_u is the magnetic anisotropy and H_0 is the intrinsic switching field; the index n is a factor depending on the easy axis orientation of the grains. When considering a certain temperature, the energy barrier needs to be compared to the thermal activation energy $k_B T$, where k_B is Boltzmann's constant and T is absolute temperature. The relaxation time τ is an exponential function given by the Arrhenius-Neel law¹⁰

$$\tau = \frac{1}{f_0} \exp\left(\frac{E_B}{k_B T}\right) \quad (1.3)$$

Here, f_0 is the attempt frequency. From Eq (1.2) and (1.3), it can be seen that the relaxation time decreases with reducing grain volumes, which leads to potential data loss as the medium is thermally demagnetized.

Theoretical¹¹ and experimental¹² analyses predict that at the thermal stability condition $K_u V > 55k_B T$ and the drive working temperature about 340K, the signal stability can be sufficiently sustained over at least five years for data storage. This criterion sets the limitation of minimum grain volume and is the basic predictions for areal densities limited by thermal activation of the grains.¹¹

1.1.2 Chemically ordered L1₀ FePt media and corresponding study

As mentioned in section 1.1.1, approaching areal density toward 1Tb/in² by decreasing the grain size, the recording media is predicted to encounter the superparamagnetic instability. In order to overcome this issue, materials possessing high magnetic anisotropy (k_u) must be utilized as recording media. Recently, L1₀ chemically ordered FePt film with face centered tetragonal (fct) structure has drawn a considerable attention as a potential candidate for ultrahigh density recording media due to its high magnetic anisotropy and its value is 7×10^6 J/m³. However, when the FePt film is deposited at RT, it exhibits fcc structure. A high temperature annealing treatment is needed to trigger the phase transformation from disordered A1 to ordered L1₀ structure, namely, ordering phase transformation.

1.1.2.1 Basic knowledge on FePt ordering phase transformation

In most substitutional solid solutions, the two kinds of atoms A and B are arranged more or less randomly on the atomic sites of lattice. In this type of solution, the dominate effect of a change in temperature is to increase or decrease the amplitude

of thermal vibration.¹³ However, there are also some solutions which have this random structure only at elevated temperatures, e.g., FePt alloys. As these solutions are cooled down below a critical temperature T_c , the A and B atoms arrange themselves at certain lattice sites with periodic manner. This type of solution then appears to be ordered or possess a superlattice. When this periodic arrangement of A and B atoms persists over a long distances in the crystal, it is defined as long range order. If the ordered solution is heated up above T_c , the atoms of A and B rearrange themselves at a random manner, i.e., disordered structure.

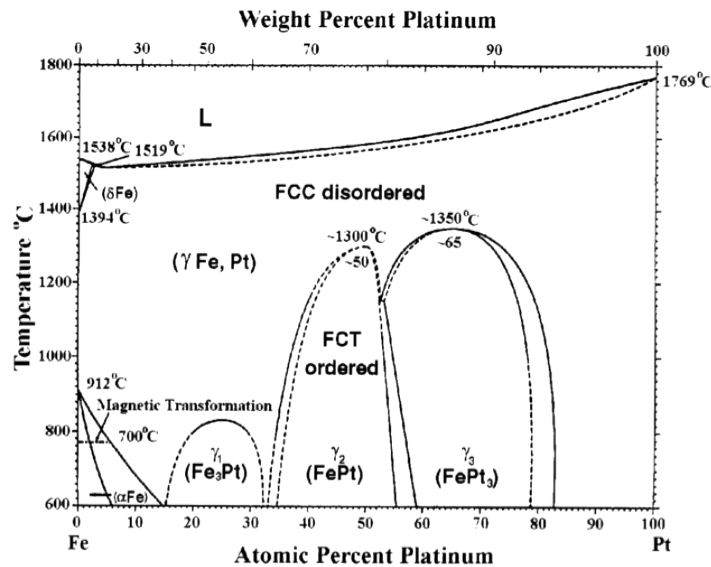


FIG 1-2 Binary phase diagram of Fe-Pt.¹⁴

The Fe-Pt phase diagram is shown in Fig 1-2.¹⁴ The melted stoichiometric FePt solidifies into a disordered fcc phase (Fig 1-3a) and then transforms into an ordered fct phase (Fig 1-3b) near 1300°C. This transformation shows characteristics that it takes place at a very high temperature and does not require a long range diffusion process (interface control growth).¹⁵ For ordered FePt, Fe and Pt atoms are stacked in alternative layers along c axis as shown in figure 1-3b. In the Fe-Pt phase diagram, the $L1_0$ phase region is surrounded by narrow two phase regions, indicating that the

ordering phase transformation of FePt may be characterized by a first order phase transformation.¹⁶

To describe the state of chemical order in FePt films, an order parameter is quantified as follow¹⁷

$$S = r_{Pt} + r_{Fe} = \frac{r_{Pt} - x_{Pt}}{y_{Fe}} = \frac{r_{Fe} - x_{Fe}}{y_{Pt}} \quad (1.4)$$

Where x_{Pt} and x_{Fe} are the atomic fraction of Fe and Pt; r_{Pt} and r_{Fe} are the fraction of Pt and Fe sites occupied by the correct atom in the L1₀ structure; y_{Pt} and y_{Fe} are the fraction of correct Pt-sites and Fe-sites and both equal to 0.5 in the L1₀ structure. When the chemical order is perfect, i.e., $S = 1$, all Pt-sites and Fe-sites are occupied by the correct atoms. While for complete disorder, all sites are equally occupied by Pt and Fe and $S = 0$. From the definition of S above, it is known that the perfect order can be obtained only at the equiatomic composition. For other cases, the maximum S shows a dependence on composition and can be expressed as $S_{max} = 1-2x$, in which x is the compositional deviation from 0.5.¹⁸

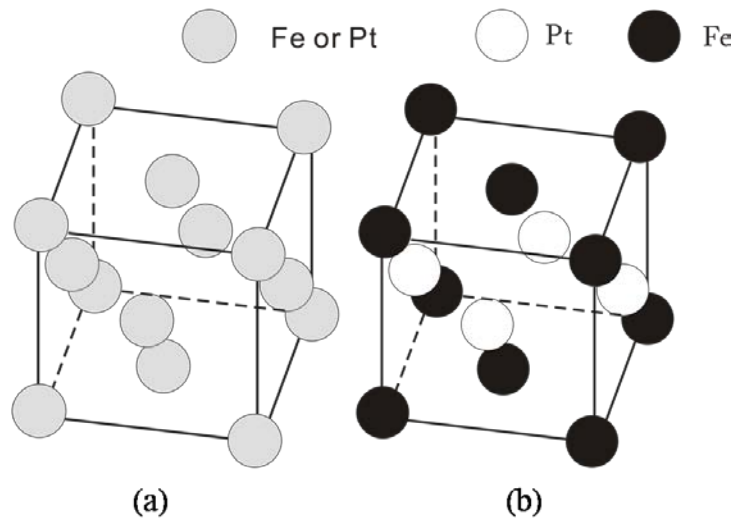


FIG 1-3 Schematic drawing of FePt crystallographic structures of (a) A1 phase (b) L1₀ phase.

For application of FePt in magnetic recording system, the main task is to achieve the ordered phase in reducing dimension. In such issue, some parameters determine the ordering phase transformation, which must be taken into account. In the following sections, the fundamental influential factors of composition and thickness on FePt ordering phase transformation in thin film will be given.

1.1.2.2 Role of composition on ordering transformation in FePt thin film near the equiatomic ratio

K. Barmak¹⁹ and D.C. Berry²⁰ *et al.* have investigated the kinetics and thermodynamics of the A1 to L1₀ transformation in FePt films near the equiatomic ratio by using differential scanning calorimetry (DSC). Fig 1-4b shows that the activation energy for the transformation is in the range of 1.4 to 2.0eV and shows a minimum at the atomic ratio of Fe around 52%. This minimum value of activation energy reflects the greater ease of nucleation of the L1₀ phase and transport of atoms across the A1-L1₀ interface in this composition. As seen in Fig 1-4b, the kinetic ordering temperature decreases as the Pt content is increased and reaches a minimum temperature at 357°C near 46% Pt. Through the critical point, it increases more rapidly for Pt-rich films than the Fe-rich films. The decrease in the kinetic ordering temperature suggests the increase in driving force for the transformation. Based on the

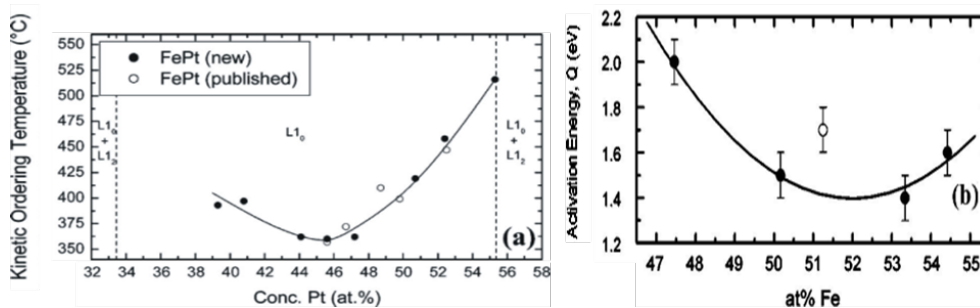


FIG 1-4 (a) Kinetic ordering temperature as a function of composition for A1 to L1₀ transformation in FePt,²⁰ (b) activation energy as a function of Fe content in the films.¹⁹

result (in Fig 1-4b), it indicates that the largest driving force over this composition range is near 46% Pt. Taking into account the influence of composition on the activation energy and kinetic ordering temperature, the off stoichiometric Fe-rich films requires a relatively low temperature for the ordering phase transformation.

1.1.2.3 Dimensional dependence of FePt ordering phase transformation

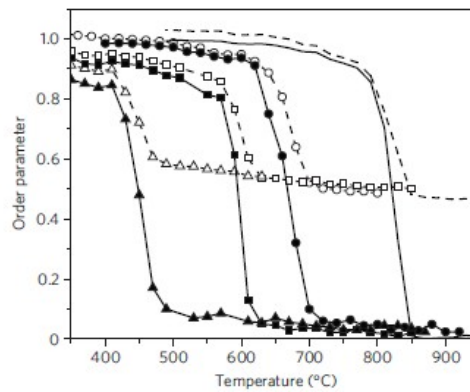


FIG 1-5 Long range order parameter (filled symbols/solid lines) for various temperatures calculated by Monte Carlo simulations of bulk CoPt (no symbol), a 3 nm diameter isotropic truncated octahedral (circle), 2.5 nm (squares), and 2 nm (triangles).²³

For spherical nanoparticles without considering their morphology, the ordered phase is inhibited by the nanoparticle dimensions. This size effect can be attributed to a decrease of the phase transition temperature when the particle size is below a few nanometers. This effect has been realized by numerous theoretical studies.^{21, 22} More recently, the influence of size and morphology on the order-disorder phase transition temperature of CoPt nanoparticles have been investigated both experimentally and theoretically by D. Alloyeau *et al.*²³ Figure 1-5 shows the ordering parameter of CoPt nanoparticles as a function of temperature by using Monte Carlo simulation. The critical order-disorder temperature of a nanoparticle with given size was estimated

from the inflexion point on the curve. From this curve, it can be seen that the critical temperature is shifted towards lower temperatures with decreasing cluster size. For instance, a 3 nm diameter particle has an order-disorder transition temperature of 175°C lower than that of bulk, in which the phase transition occur around 650°C. Besides, in this study they also provide experimental evidence that the critical temperature is uniquely determined by the smallest characteristic length of a nanoparticle.

The effect of film thickness on the order-disorder phase transition of ultrathin FePt films (from 3 to 13 nm) was investigated by Michael F. Toney *et al.*¹⁷ The single layer FePt films were deposited on 1 nm Pt seedlayers at a substrate temperature of 400°C. With increasing thickness, the coercivity (H_c) increases quickly and then plateaus as shown in Fig 1-6a. A very similar tendency is also observed in Figs 1-6b and c. When the thickness increases, the chemically ordered fraction increases and hence the volume average ordering parameter also increases. From these experimental results, it verifies that the layer thickness has a strong effect on the order-disorder phase transition for ultrathin FePt films.

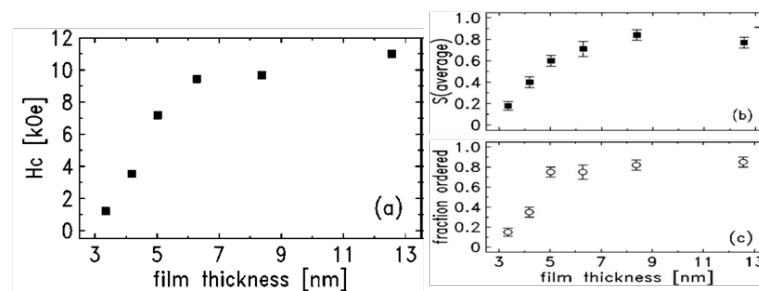


FIG 1-6 Dependence of various parameters on FePt film thickness: (a) H_c , (b) volume average ordering parameter, and (c) ordered fraction.¹⁷

1.2 Read head associated ferromagnetic-antiferromagnetic interaction

In hard disk drives, the spintronic devices with giant magnetoresistive (GMR) or magnetic tunnel junction (MTJ) structure are dominating applied to read heads. As shown in Fig 1-7, the spin valve consists of two ferromagnetic layers, one of the two magnetic layers being “pinned”, i.e., the magnetization in that layer is relatively insensitive to moderate magnetic fields.²⁵ The other magnetic layer is named as “free layer”, whose magnetization can be changed by a relatively small external magnetic fields. The exchange bias effect²⁶ originated from ferromagnetic (FM)/antiferromagnetic (AFM) interfacial coupling refers to a horizontal shift in the hysteresis loop, and it has been used to pin the FM magnetization in spintronic devices since the development of spin valves.²⁵ Very recently, the spin-orbit torque

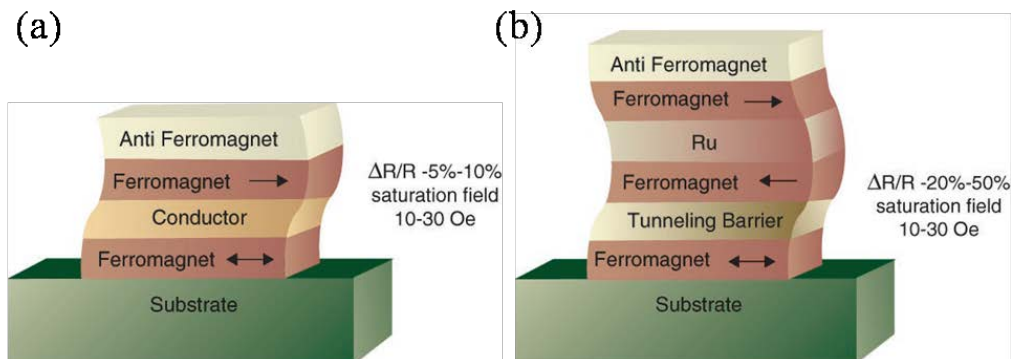


FIG 1-7. Spin-dependent transport structures. (A) Spin valve, (B) Magnetic tunnel junction.²⁴

(SOT)-induced magnetization switching was realized in a FM/AFM bilayer structure,²⁷ which may stimulate a great interest to develop modern spintronic devices using such structure. Although the FM/AFM structure is widely used in magnetic recording technology, the mechanism of exchange bias is still open to debate.²⁸ In

proceeding sections, we have introduced the magnetic recording media of ordered FePt alloy. Owing to the large magnetocrystalline anisotropy along c axis, if the ordered FePt is grown as a (001) textured film, it will exhibit strong perpendicular magnetic anisotropy. Through using FePt(L1₀)/AFM structure, the feature of perpendicular magnetization may facilitate the theoretical study of exchange bias, especially the effect of AFM spins on FM spin alignment during magnetization switching in domain imaging experiments.^{29,30} In order to study the mechanism of exchange bias, it is highly required to understand the existing models in detail. In the following sections, several important models which are in the attempt to explain the exchange bias effect will be given.

1.2.1 The AFM domain wall parallel to the ferromagnetic/antiferromagnetic interfaces³¹

In FM/AFM bilayer structure, the exchange interaction JS_1S_2 at interface favors parallel alignment of the spins S_1 and S_2 in the FM or AFM layer, respectively. To simplify this interaction, the anisotropy in FM layer is assumed to be parallel to that of AFM layer or sufficiently small. If the AFM layer has an uniaxial anisotropy and exhibits a single-domain state, the FM layer is completely magnetized in the direction of AFM uniaxial anisotropy. In this case, to reverse the FM magnetization, a magnetic field H_{ex} must be applied, which is called the effective exchange field, namely exchange bias field. With JS_1S_2 the energy per pair of FM and AFM spins and $1/a^2$ the number of pairs per unit area (a is the lattice parameter), the exchange bias field can be simply estimated as $H_{ex} = 2JS_1S_2/a^2Mt$, where t is the thickness of FM layer. However, the calculated value of H_{ex} using this formula is too large by orders of magnitude if one assumes bulk values for the exchange parameter J .

Besides the poor interface coupling, Mauri *et al.* point out that the fundamental reason for this discrepancy is the formation of AFM domain wall reversing the spins at interface, and the proposed simple model is shown in Fig 1-8. The AFM layer is assumed to have an uniaxial anisotropy with infinite layer thickness. The FM spins all show same angle β with the z axis, while the AFM spins in the last layer show the angle α with the z axis. If $\alpha \neq 0$, a domain wall extends into the AFM layer. The total magnetic energy of this interface is

$$\begin{aligned} \delta^* = & 2\sqrt{AK}(1 - \cos \alpha) + A_{12}/\xi[1 - \cos(\alpha - \beta)] \\ & + K_F t \cos^2 \beta + HMt(1 - \cos \beta) \end{aligned} \quad (1.5)$$

The first term is the energy of AFM domain wall, in which A and K are the exchange stiffness and crystalline anisotropy in the AFM layer, respectively, the second term is exchange energy at interface, and the thickness of interface region is denoted as ξ with A_{12} the exchange stiffness, the third term is the anisotropy energy in FM layer with anisotropy constant K_F ; the last term is the magnetostatic energy. The energy in units of $2\sqrt{AK}$, the expression for δ is

$$\begin{aligned} \delta = & (1 - \cos \alpha) + \lambda[1 - \cos(\alpha - \beta)] \\ & + \mu \cos^2 \beta + \kappa(1 - \cos \beta) \end{aligned} \quad (1.6)$$

Here, the interface exchange denotes $\lambda = A_{12}/\xi 2\sqrt{AK}$, the anisotropy in FM layer is $\mu = K_F t / 2\sqrt{AK}$, and the external magnetic field is $\kappa = HMt / 2\sqrt{AK}$. By using $\lambda = 0.25$ and various λ value, the magnetization curves of the FM layer are calculated from Eq (1.6). Extracted detailed information from this numerical calculation, some special features on H_{ex} can be obtained based on this simple AFM domain wall model.

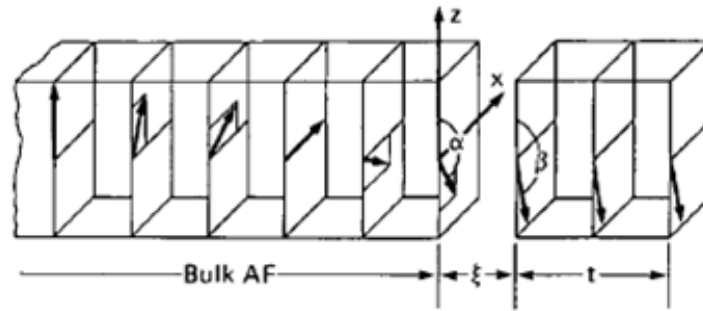


FIG 1-8 Magnetic model for the interface of FM/AFM structure. The uniaxial anisotropy of AFM layer is along the z axis. The spin structures in this figure are in response to an external magnetic field applied opposite to z direction. The spins of only one sublattice in AFM layer are shown.³¹

They showed that in this simple model the exchange field can be classified into two distinct regimes, i.e., weak coupling ($\lambda \ll 1$) and strong coupling regime ($\lambda \gg 1$). In weak coupling regime, the exchange field is only determined by the interfacial coupling. In strong coupling regime, the exchange field is not proportional to the interfacial coupling but rather reaches a limit value corresponding to the formation of 180° planar domain in AFM layer. The significance of this simple model is the explanation for the limit value of exchange field through the formation of AFM domain wall, which deepens the understanding of interfacial FM/AFM interaction.

1.2.2 Random field arising from interface roughness in ferromagnetic/antiferromagnetic structure³²

In proceeding section, we have introduced Mauri's AFM domain wall model for exchange bias. However, this simple model only focuses on the spins in one AFM sublattice without considering the interface roughness related effect, which strongly affects the FM/AFM interfacial coupling. Since the atomistically perfect uncompensated AFM interface is unlikely in practice, a more sophisticated model is needed. Analogous to the classic Imry-Ma domains of the random field problem,³³

Malozemoff proposed a random field model for the interaction at FM/AFM interface arising from interface roughness.

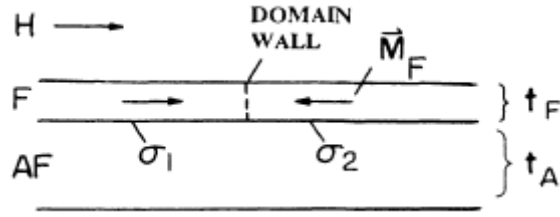


FIG 1-9 Schematic illustration of FM/AFM structure with FM domain wall driven by an external field H .³²

The basic idea of this model is shown in Fig 1-9, where an in-plane external field is applied in the uniaxial direction of FM layer. If the FM/AFM interfacial energy differs for two FM domains, the exchange field is determined by the interfacial energy difference $\Delta\sigma$ between two opposite FM configuration

$$H_E = \Delta\sigma / 2M_F t_F \quad (1.7)$$

M_F and t_F are the magnetization and thickness of FM layer, respectively. Assuming an in-plane AFM spin alignment with FM/AFM collinear coupling, the exchange field in the case of idealized compensated or uncompensated AFM interface can be simply estimated using Eq (1.7). For fully compensated AFM interface, as shown in Fig 1-10a, the equal number of two opposite directions of AFM spins at interface lead to a zero interfacial energy difference before and after magnetic reversal of FM layer. As a consequence, the exchange field should be zero. On the other hand, for uncompensated AFM interface, as shown in Fig 1-10b, there is an interfacial energy difference favoring one FM orientation over the other. Assuming a simple cubic structure, Eq (1.7) gives $H_E = J_i / a^2 M_F t_F$, where J_i is the exchange parameter across the interface and a is lattice constant. However, in practical case, by using relevant parameters, the predicted values of H_E are two orders of magnitude too large. Since

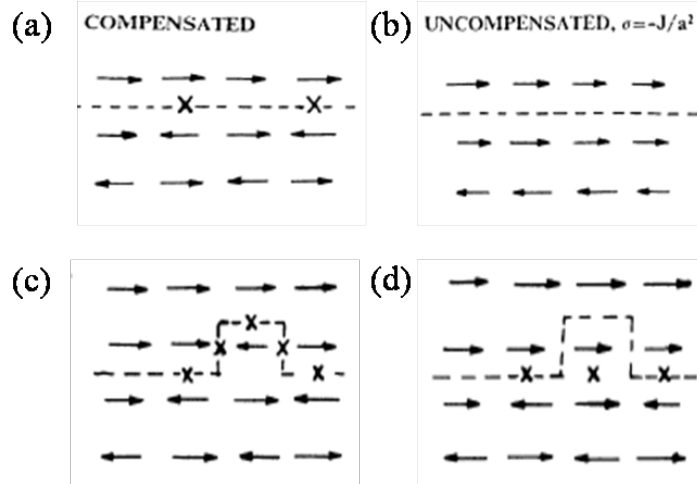


FIG 1-10 Schematic illustration of possible spin configuration at FM/AFM interface. (a) Compensated AFM interface, (b) uncompensated AFM interface, (c) compensated AFM interface with atomic bump, and (d) a lower energy state of (c). Frustrated bonds are indicated by crosses. While in the case of (c) and (d), the bump should be visualized on a two dimensional interface.³²

any monatomic step at interface will change the sign of the interaction and consequently affect the interfacial energy, it is essential to study the influence of interface roughness. A rough AFM interface is then considered by introducing a single monatomic bump at compensated interface as shown in Fig 1-10c. This configuration gives one FM coupled spin pair across the interface replaced by five AFM coupled pairs, consequently a net AFM deviation of 6 away from compensation. If AFM spins remain fixed, after magnetic reversal of FM layer, it gives a net FM deviation of 6 away from compensation. Therefore, the interfacial energy difference is $z_i J_i$, with $z_i = 12$. This energy difference can be reduced from generating one frustrated AFM spin pair under the bump as shown in Fig 1-10d. Finally, the interfacial energy difference after magnetic reversal of FM layer reduces to $2J_i + 2J_A$ or roughly $4J_i$, if $J_i \sim J_A$. Here J_A is the AFM exchange constant.

In consideration of localized canting of the spins, the interfacial energy difference is expected to reduce somewhat further. To simplify this issue, it assumes

that associated with each interface irregularity is a local energy difference and its average value is $2zJ$, where z is a number of order unit as given above, and J exchange constant assumed to be same at and on either side of interface. Another key physical insight is that if an interface is random on an atomic scale, the local unidirectional interface energy $\sigma_l = \pm zJ/a^2$ will also be random. Similar with the Imry-Ma random field problem, the average σ in a region of area L_2 will become $\sigma \propto \sigma_l/\sqrt{N}$. Here $N = L^2/a^2$ is the number of sites projected onto the interface plane. Realize the random field and assume a region with a single domain in FM layer, giving rise to the formation of domain like region in AFM layer. Correspondingly, the interfacial energy can be determined by three terms: unidirectional interface energy, competing exchange energy in AFM layer, and AFM in-plane anisotropy energy. For such case, the competing exchange energy and in-plane anisotropy energy show a tendency for the lateral dimension of AFM domain L to expand and contract, respectively. To balance the competing energies, it gives $L \propto \pi\sqrt{A/K}$. Once these domains are fixed, the energy difference per unit area before and after magnetic reversal of FM layer is $\Delta\sigma = 4zJ/\pi aL$. Finally, Eq (1.7) estimates the exchange field

$$H_E = 2z\sqrt{AK}/\pi^2 M_F t_F \quad (1.8)$$

By using this formula, the exchange field can be plausibly estimated. On the other hand, the most interesting feature of this model is the extension of classic random field concepts to the interface roughness related exchange bias effect.

1.2.3 Ferromagnetic/antiferromagnetic interfacial interaction at compensated antiferromagnetic interfaces³⁴

The above two classic models, which provide physical origins, have successfully

reduced the discrepancy between the predicted and observed exchange field. However, by simply assuming a collinear coupling between FM and AFM spins, what happens at fully compensated interfaces can be hardly addressed. Based on the results of full micromagnetic numerical calculations on FM/AFM structure with compensated AFM interfaces, N. C. Koon found that the interfacial exchange coupling is relatively strong with a perpendicular orientation between the FM/AFM axis directions, similar to the classic “spin flop” state in bulk antiferromagnets.

To study the FM/AFM exchange interaction at compensated AFM interface, it assumes a simple body centered tetragonal magnetic structure with exchange interactions along the body diagonals, and $J_{FF} = -J_{AA} = -J_{FA} = 1$ meV. Meanwhile, a simple case of (110) oriented FM and AFM layer with thickness of 15 monolayers each is considered, which is convenient for calculation by using relaxation methods. In each of FM and AFM layer all the spins are constrained to be aligned in the same axis, with an angle φ between the axes of two layers. The results show that, for pure FM or AFM films the minimum energy occurs at $\varphi_0 = 0^\circ$, while the film with FM/AFM interface has a minimum at $\varphi_0 = 90^\circ$. In both case, the angular dependence of energy can be well fitted by a polynomial of the form $c(\varphi - \varphi_0)$. In the case of film with FM/AFM interface $c = 1.98 \times 10^{-5}$ meVdeg⁻², and for pure FM or AFM film $c = 2.1 \times 10^{-5}$ meVdeg⁻². Since c is proportional to the exchange constant J , a striking conclusion can be drawn: besides the 90° FM/AFM coupling configuration, the magnitude of effective exchange coupling is reduced by a relatively small amount compared to a homogeneous (FM or AFM) film with the same magnitude of exchange and thickness. Figure 1-11 shows the configuration of spins near the FM/AFM interface at minimum energy angle $\varphi = 90^\circ$. If J_{FA} is antiferromagnetic, the AFM spins will cant away from the FM direction as shown. This canting angle is

because of the competing interfacial energy and antiferromagnet energy,³⁵ and decays rapidly as a function of distance from the interface, giving rise to a macroscopic 90° FM/AFM coupling.

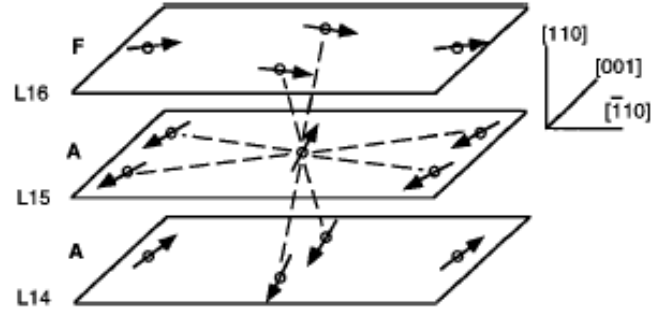


FIG 1-11 Spin configuration near the interface plane for a 15/15 ML FM/AFM structure with lowest energy orientation ($\varphi = 90^\circ$).³⁴

It is well known that the essential pinning for exchange bias in FM/AFM structure comes from the uniaxial anisotropy of AFM layer. Assuming an uniaxial anisotropy K_U along [001] axis in AFM layer, the angular θ dependence of energy per unit area for various AFM layer thickness has been calculated, in which θ denotes the angle between the FM spin and [001] axis in the (110) plane and the initial angle is $\theta_0 = 90^\circ$. By changing the angle θ incremented away 90° , the results of calculation show that for t_A much less than the AFM domain wall width w [$\sim (4J/K_U)^{1/2} = 9$ ML] the angular dependence of the energy is reversible and the energy curves exhibit mirror symmetry about $\theta = 0^\circ$ and 180° . However, for $t_A \geq w$, the energies increase smoothly as the FM spins rotate through $\theta = 0^\circ$ and 180° , and the energy curves no longer have mirror symmetry. Further increasing the angle θ , the FM spins are blocked by an energy barrier for the transition to a lower energy branch until $\theta = \theta_{CR}$. Note that this critical angle increases with the AFM layer thickness. More importantly, the change of energy curves for various AFM layer thickness indicates that only for t_A ($\theta > 90^\circ$) can lead to exchange bias.

According to the results of calculation given above, this study predicts a macroscopic 90° FM/AFM coupling at AFM compensated interface, which sheds a particular light on the complex mechanism of exchange bias. Assuming a rotation magnetization of FM layer, the physical picture emerging from this model is that exchange bias results from the formation of AFM parallel domain wall as suggested in section 1.2.1. With reasonable parameters the calculations predict exchange field comparable to those observed. Moreover, such macroscopic 90° FM/AFM coupling was further studied by R. L. Stamps.³⁶

1.3 Objectives of this study

Realizing the background given in sections 1.1 and 1.2, we considered to do some theoretical study with the assistance of strong uniaxial anisotropy in $L1_0$ FePt. By using $L1_0$ FePt based structures, it may facilitate the understanding of an interesting theme, namely, the FM/AFM interfacial coupling, especially the mechanism of exchange bias for some particular cases. Therefore, the objectives of this study are as follows:

- (1) To investigate the influential factors of FePt ordering and preferred growth orientation in FePt/AlN multilayer structures;
- (2) With the well understanding of FePt ordering, to establish perpendicular exchange bias in FePt/NiO bilayer structure on MgO(001) single crystal substrate and study the mechanism of exchange bias in the view point of FM/AFM interfacial coupling configuration;
- (3) To further study the FM/AFM interfacial coupling in FePt/NiO/FePt trilayer structures with special design.

1.4 Organization of this thesis

Chapter 1 Introduction

The background of this study is briefly introduced. Correspondingly, two interesting research topics related to the magnetic storage and magnetic reading technologies are discussed: one is the FePt ordering phase transformation; the other is the mechanism of exchange effect. For the former topic, some important studies focusing on the influential factors of FePt ordering phase transformation are reviewed. For the latter topic, several classic models with respect to the explanation of the mechanism of exchange bias are given.

Chapter 2 Preparation and characterization of L1₀ FePt based ultrathin structures

The sample preparation methods and its corresponding characterization approaches are introduced. In order to provide a better description, the basic working principle of the instruments utilized in this thesis and some experimental results are given.

Chapter 3 Effect of nitrogen upon structural and magnetic properties of FePt in FePt/AlN multilayer structures

Experimental results on the structural and magnetic properties of FePt/AlN multilayer films are shown. To obtain different strain condition during FePt ordering phase transformation, two kinds of samples were prepared, i.e., the FePt layers deposited without and with nitrogen atoms. By varying the layer thickness and annealing temperature, the influential factors of the (111) texture evolution and ordering phase transformation in FePt layers are discussed.

Chapter 4 Off-easy-plane antiferromagnetic spin canting in coupled FePt/NiO bilayer structure with perpendicular exchange bias

Owing to the strong uniaxial anisotropy of L1₀ FePt along *c* axis, perpendicular exchange bias is realized in FePt(001)/NiO($\bar{1}\bar{1}1$) orthogonal exchange coupling structure. From magnetization measurement and magnetic domain imaging, we compared three different structures: FePt single layer, FePt/NiO bilayers before and after field cooling. Based on the obtained results, the mechanism of exchange bias arising from compensated AFM interface is carefully discussed.

Chapter 5 Field cooling driven magnetic anisotropy and stripe domain evolution in FePt/NiO/FePt trilayer structure

In this chapter, we further study the FM/AFM interfacial coupling through fabricating a FePt_{Oop}/NiO/FePt_{Ip} trilayer structure, where the magnetization of bottom and upper layer lies along film normal and in the film plane with in-plane isotropy, respectively. By performing special field cooling treatment, the changes on the magnetic behavior of both FM layers were observed. In the view point of FM/AFM coupling configuration, the origin of observed results is carefully discussed.

Chapter 6 Conclusions

The achievements or findings are summarized from each chapter.

References

- ¹Dennis E. Speliotis, *J. Magn. Magn. Mater.* **193**, 29 (1999).
- ²Andreas Moser et al, *J. Phys. D: Appl. Phys.* **35**, R157 (2002).
- ³Masaaki Futamoto, *ECS Trans.* **50** (10), 59 (2012).
- ⁴Eric E. Fullerton, D. T. Margulies, M. E. Schabes, M. Carey, B. Gurney, A. Moser, M. Best, G. Zeltzer, K. Rubin, H. Rosen, and M. Doerner, *Appl. Phys. Lett.* **77**, 3806 (2000).
- ⁵E. N. Abarra, A. Inomata, H. Sato, I. Okamoto, and Y. Mizoshita, *Appl. Phys. Lett.* **77**, 2581 (2000).
- ⁶S. Iwasaki and Y. Nakamura, *IEEE Trans. Magn.* **13**, 1272 (1977).
- ⁷Hideki Saga, Hiroaki Nemoto, Hirofumi Sueda and Masahiko Takahashi, *Jpn. J. Appl. Phys.* **38**, 1839 (1999).
- ⁸H. Zhou, H. N. Bertram, M. F. Doerner, and M. Mirzamaani, *IEEE Trans. Magn.* **35**, 2712 (1999).
- ⁹H. N. Bertram, H. Zhou, and R. Gustafson, *IEEE Trans. Magn.* **34**, 1845 (1998).
- ¹⁰L. Néel, *Ann. Geophys.* **5**, 99 (1949).
- ¹¹S. H. Charap, Pu-Ling Lu and Yanjun He, *IEEE Trans. Magn.* **33**, 978 (1997).
- ¹²A. Moser and D. Weller, *IEEE Trans. Magn.* **35**, 2808 (1999).
- ¹³B. D. Cullity, *Elements of X-Ray Diffraction* (1956).
- ¹⁴T. B. Massalski, J. L. Murray, L. H. Bennet, and H. (ed.) Baker, *Binary Phase Diagrams*. ASM International, Materials Park, Ohio, 1096 (1986).
- ¹⁵S. H. Whang, Q. Feng and Y. Q. Gao, *Acta Mater.* **46** (18), 6485 (1998).
- ¹⁶A. Kussman and G. Z. Rittberg, *Metallk* **10**, 243 (1953)
- ¹⁷Michael F. Toney, Wen- Yaung Lee, Jonathan A. Hedstrom, and Andrew Kellock, *J. Appl. Phys.* **93**, 9902 (2003).

- ¹⁸R. F. C. Farrow et al., *Appl. Phys. Lett.* **69**, 1166 (2002).
- ¹⁹K. Barmak, J. Kim, D. C. Berry, and W. N. Hanani, *J. Appl. Phys.* **97**, 024902 (2005).
- ²⁰D. C. Berry and K. Barmak, *J. Appl. Phys.* **102**, 024912 (2007).
- ²¹R. V. Chepulsii and W. H. Butler, *Phys. Rev. B* **72**, 134205 (2005).
- ²²Bo Yang, Mark Asta, O. N. Mryasov, T. J. Klemmer, and R. W. Chantrell, *Acta Mater.* **54**, 4201 (2006).
- ²³D. Alloyeau, C. Ricolleau, C. Mottet, T. Oikawa, C. Langlois, Y. Le Bouar, N. Braidy, and A. Loiseau, *Nat. Mater.* **8**, 940 (2009).
- ²⁴S. A. Wolf, D. D. Awschalom, R. A. Buhrman, J. M. Daughton, S. von Molnár, M. L. Roukes, A. Y. Chtchelkanova, D. M. Treger, *Science* **294**, 1488 (2001).
- ²⁵B. Dieny, V. S. Speriosu, S. S. P. Parkin, B. A. Gurney, P. Baumgart, and D. R. Wilhoit, *J. Appl. Phys.* **69**, 4774 (1991).
- ²⁶W. H. Meiklejohn and C. P. Bean, *Phys. Rev.* **102**, 1413 (1956).
- ²⁷Shunsuke Fukami, Chaoliang Zhang, Samik DuttaGupta, Aleksandr Kurenkov, and Hideo Ohno, *Nat. Mater.* **15**, 535 (2016).
- ²⁸J. Nogués and I. K. Schuller, *J. Magn. Magn. Mater.* **192**, 203 (1999).
- ²⁹P. Kappenberger, S. Martin, Y. Pellmont, H. J. Hug, J. B. Kortright, O. Hellwig, and Eric E. Fullerton, *Phys. Rev. Lett.* **91**, 267202 (2003).
- ³⁰I. Schmid, M. A. Marioni, P. Kappenberger, S. Romer, M. Parlinska-Wojitan, H. J. Hug, O. Hellwig, M. J. Carey, and E. E. Fullerton, *Phys. Rev. Lett.* **105**, 197201 (2010).
- ³¹D. Mauri, H. C. Siegmann, P. S. Bagus, and E. Kay, *J. Appl. Phys.* **62**, 3047 (1987).
- ³²A. P. Malozemoff, *Phys. Rev. B* **35**, 3679(R) (1987).
- ³³Y. Imry and S. K. Ma, *Phys. Rev. Lett.* **35**, 1399 (1975).

³⁴N . C. Koon, Phys. Rev. Lett. **78**, 4865 (1997).

³⁵M. D. Stiles and R. D. McMichael, Phys. Rev. B **59**, 3722 (1999).

³⁶R. L. Stamp, J. Phys. D **33**, R247 (2000).

Chapter 2 Preparation and characterization of L1₀ FePt based ultrathin structures

In this chapter, the preparation and characterization methods of L1₀ FePt based ultrathin structures are covered, and the content will be organized as follows. In this thesis, the samples were fabricated by direct current (DC) magnetron sputtering. In the first section, the basic information on sputtering apparatus and some experimental parameters are given. Then, in the second section, the characterization methods subdivided into structural and magnetic characterization are introduced. Since the structural features in ultrathin structures play a key role to determine the magnetic properties, many characterization methods including conventional x-ray diffraction (XRD), tilted angle XRD, grazing incidence in-plane XRD, XRD φ scan, and transmission electron microscopy (TEM) were utilized in this thesis. Some of these methods are selectively described in this chapter. For magnetic characterization, the technologies used in this thesis were vibrating sample magnetometer (VSM), superconducting quantum interference device (SQUID) magnetometer, and magnetic force microscopy (MFM), which are also introduced in this chapter.

2.1 Preparation of L1₀ FePt based ultrathin structures

The L1₀ FePt based ultrathin structures were prepared by utilizing DC magnetron sputtering in this thesis and the basic working principle is shown in Fig 2-1a. Compared with simple DC sputtering, magnetron sputtering, benefiting from an applied magnetic field above the target surface to constraint electron motions (Fig 2-1b), possesses some admirable advantages, e.g., the higher deposition rates and stable

discharge at lower pressure.¹ Therefore, this method can improve the film quality with high sputtering efficiency.

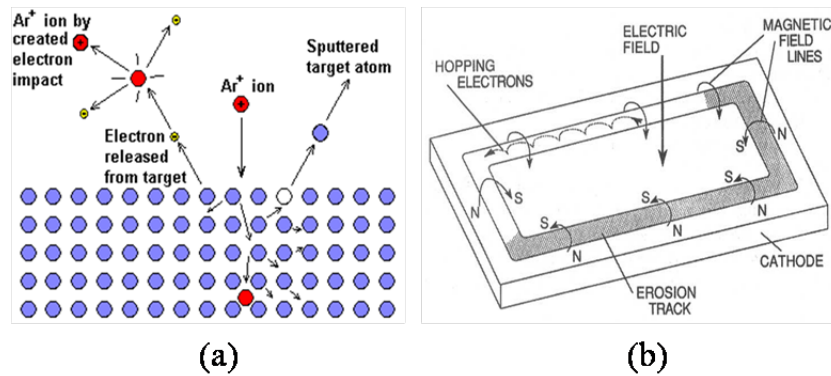


FIG 2-1 (a) Schematic illustration of sputtering process, (b) applied field and electron motion in the planar magnetron.¹

Figure 2-2a shows a schematic illustration of DC magnetron sputtering apparatus used in this work. The pumping system consists of a turbo-molecular pump backed by

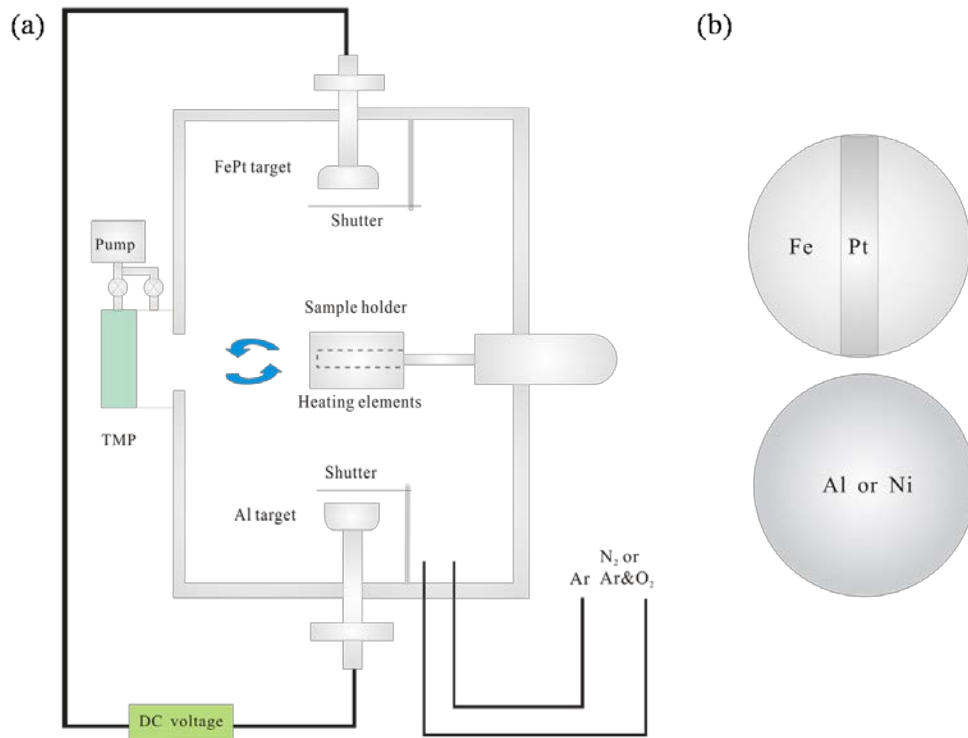


FIG 2-2 (a) Schematic illustration of DC magnetron sputtering system. (b) FePt and Al (Ni) targets.

a rotary pump. The rotary pump firstly evacuate the chamber to a low vacuum of about 10^{-1} Pa, and then open the valve of turbo-molecular pump to obtain a base pressure below 5×10^{-5} Pa. There are three kinds of targets mounted on the sputtering guns. The upper target is fixed as FePt target composed of a Pt chip on the top of Fe plate and the areal ratio is 1:4.3 (Fig 2-2b). On the other hand, the bottom target is either pure Al or Ni target. For the deposition of FePt/AlN multilayer structures as shown in Fig 2-3a, the FePt layers were deposited in an atmosphere of pure Ar or Ar mixed with N₂, while the AlN layers were deposited by reactive sputtering in a mixture atmosphere of Ar and N₂. The Ar/N₂ flow ratio was controlled by mass flow controller. After the film deposition, an *ex situ* annealing was performed in a high vacuum tube furnace to trigger the FePt ordering phase transformation. For the deposition of FePt/NiO bilayer and FePt_{Oop}/NiO/FePt_{Ip} trilayer structure as shown in Figs 2-3b and 2-3c, unlike the FePt/AlN multilayer structure, the FePt layer was deposited at elevated substrate temperature on MgO(001) single crystal substrate to induce epitaxial growth. The heating elements are embedded in the sample holder. By subsequently performing an *in situ* annealing, the partially ordered FePt layer was obtained. Then the NiO layer was subsequently deposited on the top of partially ordered FePt layer at 230°C in a mixture atmosphere of Ar and O₂.

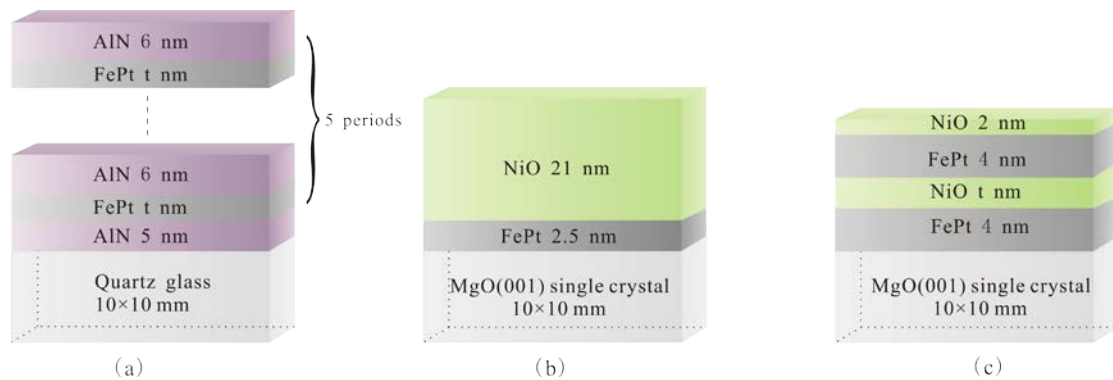


FIG 2-3 Schematic drawing of L1₀ based ultrathin structures: (a) FePt/AlN multilayer structure, (b) FePt/NiO bilayer structure, (c) FePt_{Oop}/NiO/FePt_{Ip} trilayer structure.

2.2 Structural characterization

2.2.1 Conventional and Grazing incidence in-plane x-ray diffraction

The $\theta/2\theta$ diffractometer is an often-used instrument for measuring the Bragg reflection of thin films and its working principle is visualized in Fig 2-4a. The sample is positioned in the center of the instrument and probing x-ray beam is directed to the sample surface at an angle θ . During the scan the angle of the incoming and exiting beam are continuously varied, but they remain equal throughout the whole scan, i.e., $\theta_{in} = \theta_{out}$.² Since the angles of coming and exiting beam are always specified with respect to the surface plane, the out of plane crystalline interplanar distance d can be calculated from $\theta/2\theta$ scan by using Bragg's law $2d\sin\theta = n\lambda$. The conventional XRD measurements in this thesis were performed on D8 Advance diffractometer with Cu $K\alpha$ irradiation operating at 35 kV and 300 mA. As an instance, the conventional XRD profiles for the NiO films deposited on glass substrate with various substrate temperatures are shown in Fig 2-5.

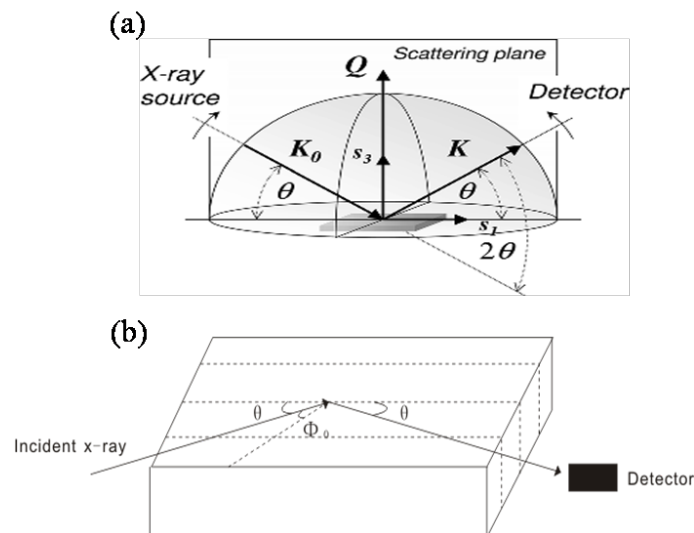


FIG 2-4 Schematic illustration of (a) conventional $\theta/2\theta$ scan,² and (b) grazing incidence in-plane XRD.

Grazing incidence x-ray diffraction (GI-XRD) is a scattering geometry combining the Bragg condition with the conditions for x-ray total external reflection from crystal surfaces (Fig 2-4b). In this thesis, this method is mainly used to investigate the in-plane crystallographic orientation of each layer in ultrathin structures. Since the penetration depth of x-ray inside is reduced by three orders of magnitude compared with the other diffraction schemes, it provides superior features for thin film study. The measurements were performed on D8 discover diffractometer using Cu K α irradiation and operated at 50 kV, 22 mA. The incident angle Φ_0 is fixed about 0.6-0.7°, and two types of scan were used for the measurements. One is detector scan, and the other is $\theta/2\theta$ scan.

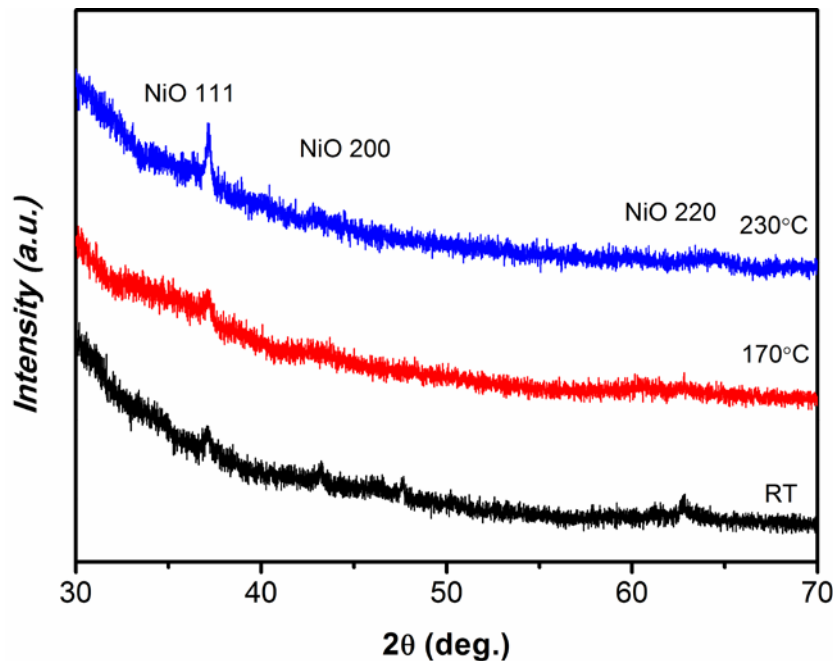


FIG 2-5 XRD profiles for NiO(90 nm) deposited on glass substrate at various temperatures.

2.2.2 Selected-area diffraction patterns

For TEM observation, there are two primary modes, which one can choose either image mode or diffraction mode. Diffraction pattern (DP) corresponding to diffraction

mode is a powerful technique to determine the presented phase in thin film and its growth orientation. Figure 2-6 shows two basic operations of the TEM imaging system. Compared with image mode, the adjustment of the imaging-system lenses is that for diffraction mode, the back-focal plane of the objective lens acts as the object

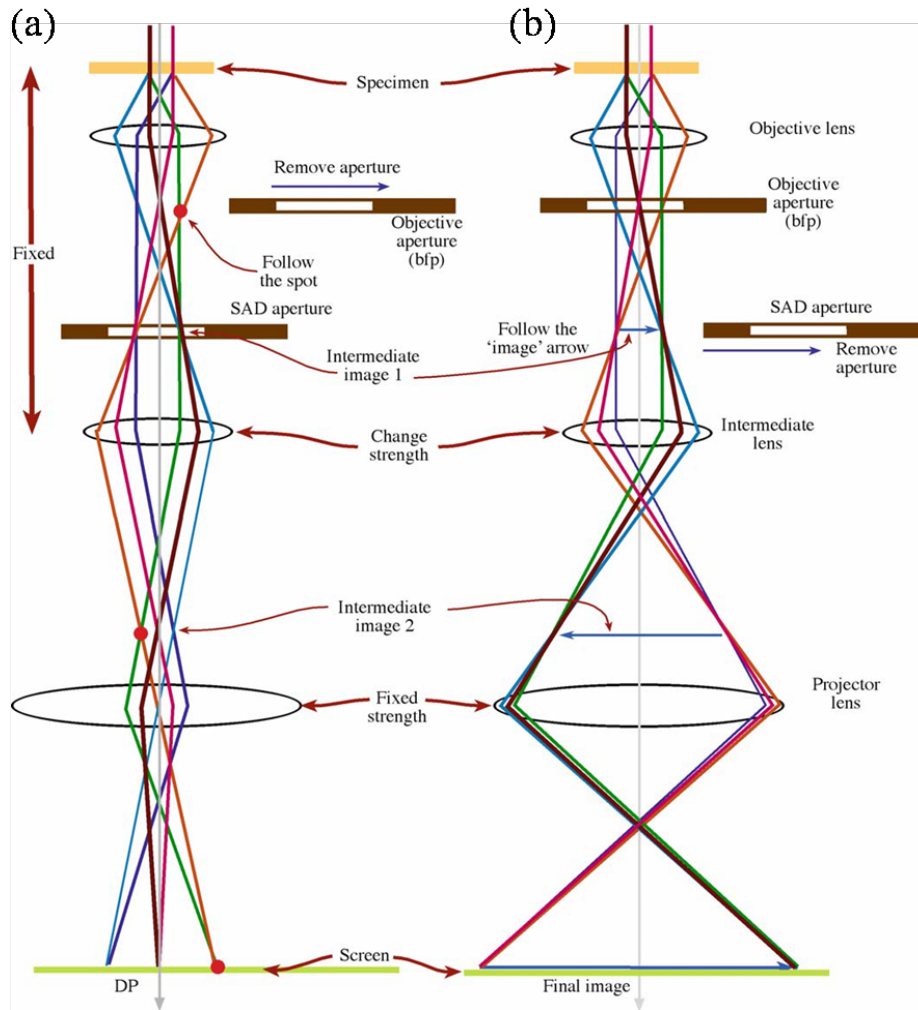


FIG 2-6 The two basic operation of the TEM imaging system: (a) diffraction mode, and (b) image mode.³

plane for the intermediate lens. As seen in Fig 2-6a, the DP projected on the viewing screen/CCD contains electrons from the whole area of the specimen exposed to the illuminated beam. Such pattern is not very useful because the specimen will be often buckled. Furthermore, the direct beam is often so intense that it will damage the

viewing screen or saturate the CCD camera.³ Therefore, through inserting a SAD aperture into the image plane of the objective lenses, the selected-area diffraction pattern (SADP) for a specific area of the specimen can be obtained, which is a basic TEM operation.

In order to determine the in-plane crystallographic orientation of each layer in ultrathin structures, the specimens were prepared for the in-plane TEM observation. The preparation method is briefly given below. Firstly, cut the sample into a 3 mm-diameter specimen by Gatan ultrasonic cutter. Then grind the specimen from substrate side (opposite to the film surface) by sand paper until it is thinner than 60 μm . After that, move the specimen into an acid solution, which is composed of 98% H_3PO_4 and 2% H_2SO_4 . Note that in our case, the MgO substrate is soluble in the acid solution that we use, whereas the film containing FePt and NiO is not such sensitive to this solution. By heating up the solution to around 70°C and holding this temperature for 30 min, the MgO substrate is partially dissolved. Finally, remove the specimen out of the solution and support it on the Mo grid. Figure 2-7 shows in-plane SADP for FePt/NiO bilayer structure grown on MgO(001) single crystal substrate. The result suggests that the FePt layer is partially ordered and epitaxially grown on MgO(001) substrate, while the NiO layer shows (111) texture with in-plane twined microstructures.

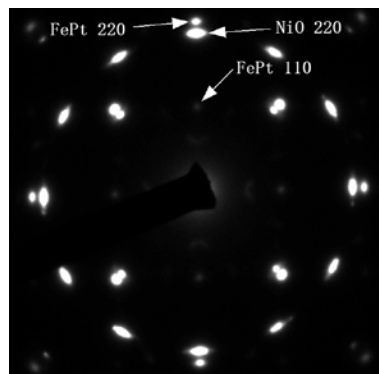


FIG 2-7 SADP for FePt(2.5 nm)/NiO(21 nm) bilayer structure grown on MgO(001) single crystal substrate.

2.3 Crystal and magnetic structure of NiO

In this thesis, the AFM material used in the ultrathin structures is NiO. Therefore, it is essential to have a deep understand on both crystal and magnetic structure of NiO. The crystal structure of NiO is of the NaCl type with the lattice constant $a_0 = 4.117 \text{ \AA}$ (Fig 2-8a). When the temperature is above Néel temperature ($T_N = 523 \text{ K}$), the NiO has a perfect fcc rocksalt structure. After cooling below T_N , a rhombohedral contraction along different $\langle 111 \rangle$ axes occurs resulting from the magnetoelastic forces. While crystallographic twinning leads to so-called T domains with the spins lying in $\{111\}$ planes, perpendicular to the contraction axes. Each T domain may further split into three different S domains with spins along three easy axis directions, e.g., $[\bar{2}11]$, $[1\bar{2}1]$, $[11\bar{2}]$ (Fig 2-8b). Within each S domain the crystal exhibits a triclinic distortion.^{5,6} Besides, another intrinsic magnetic features of NiO is the possession of easy plane anisotropy for $\{111\}$ planes. The reported easy plane anisotropy is $4.96 \times 10^6 \text{ erg/cc}$.⁷ This value is $10^2 \sim 10^3$ of that of the in-plane anisotropy,^{8,9} which is sample dependent.

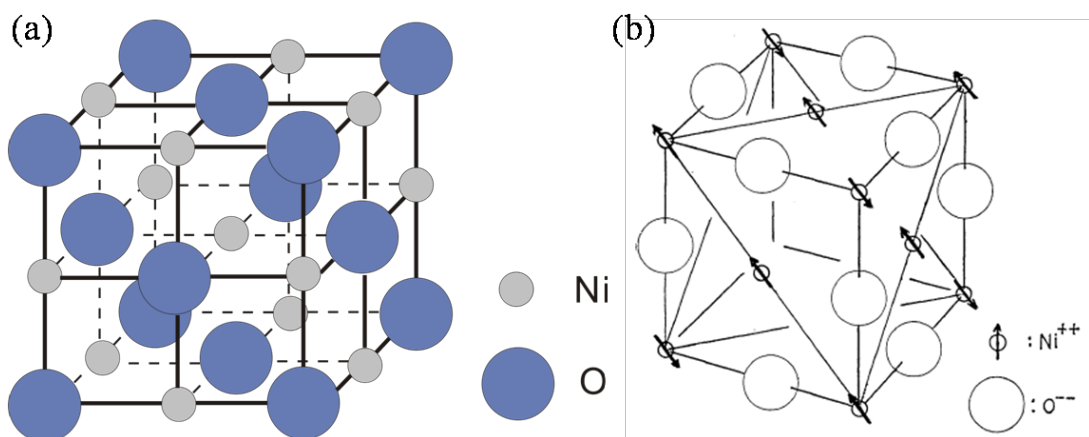


FIG 2-8 (a) The crystal structure of NiO, and (b) the magnetic structure of NiO.⁴

2.4 Magnetic characterization

2.4.1 Vibrating sample magnetometer

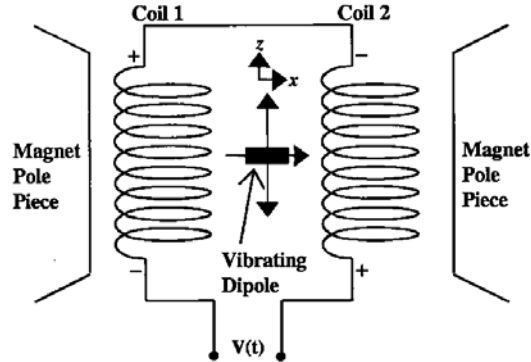


FIG 2-9 Working principle of vibrating sample magnetometer (VSM).¹¹

Vibrating sample magnetometer (VSM) developed originally by Simon Foner¹⁰ is an instrument for the measurement of magnetic moment, which possesses many advantageous, such as simplicity, ease of operation and high measuring sensitivity. The VSM is based on Faraday's law: an electromotive force is induced in a conductor by a time varying magnetic flux. The working principle is illustrated in Fig 3-3.¹¹ A sample magnetized by a homogenous magnetic field is vibrated sinusoidally at small

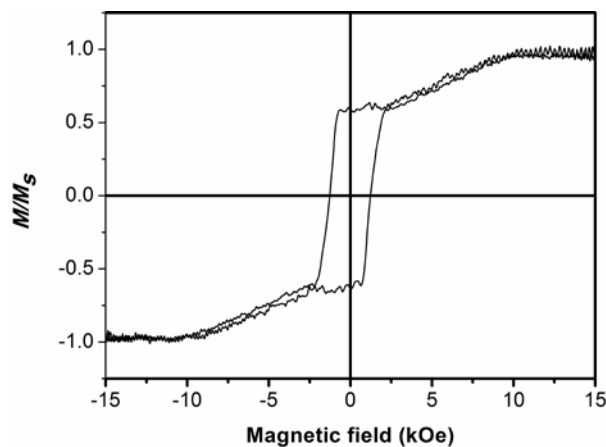


FIG 2-9 Out-of-plane magnetic hysteresis loop of FePt_{Oop}(4 nm)/NiO(2 nm)/FePt_{Ip}(4 nm) trilayer structure measured at RT

fixed amplitude with respect to stationary pick-up coils. Inside the detection coils, there will be an induced voltage, which is determined by the magnetic moment of the sample and the sample position relative to the detection coils. For stationary pick-up coils in a uniform and stable external field, the only effect measured by the coils is that due to the motion of the sample. Thus, this induced voltage is a measure of the magnetic moment of the sample. In this thesis, the magnetic properties of FePt/AlN multilayer and FePt_{Oop}/NiO/FePt_{Ip} trilayer structures were measured by VSM at RT. Figure 2-9 shows the out-of-plane magnetic hysteresis loop of FePt_{Oop}(4 nm)/NiO(2 nm)/FePt_{Ip}(4 nm) trilayer structure.

2.4.2 Superconducting quantum interference device (SQUID) magnetometer¹²

A very magnetic flux can be measured accurately by a superconducting quantum interference device (SQUID) magnetometer, which utilizes the Josephson effect. The

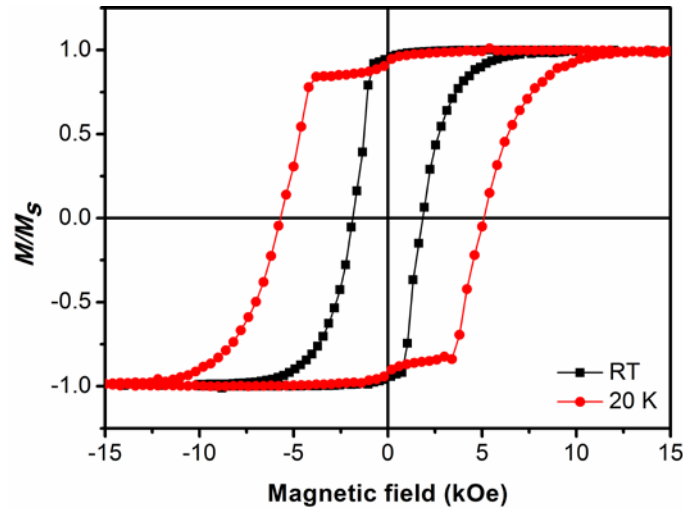


FIG 2-10 Out-of-plane magnetic hysteresis loop of FePt(2.5 nm)/NiO(10 nm) bilayer structure measured at RT and 20 K after field cooling. The field cooling was performed from 540 K to the measuring temperature with a 5 kOe applied field.

Josephson effect is the name given to the fact that the flux change in a superconducting circuit interrupted by an insulating layer about 50 Å thick is

quantized.¹³ Counting these flux quanta gives a very sensitive measurement of the flux change and therefore of the magnetization of the sample. The fact that the measuring apparatus must be at liquid helium temperature is clear a disadvantage, and a SQUID magnetometer requires a long time for each magnetization measurement, especially if the field is changed between readings. The magnetic properties of FePt/NiO bilayer structure in this thesis were characterized by SQUID magnetometer. Figure 2-10 shows the out-of-plane magnetic hysteresis loop of exchange biased FePt(2.5 nm)/NiO(10 nm) bilayer structure at RT and 20 K after field cooling.

2.4.3 Magnetic force microscopy (MFM)

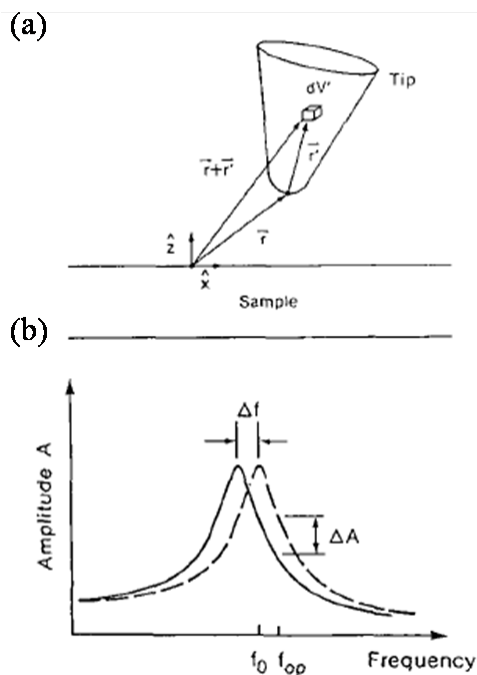


FIG 2-11 (a) Geometry used in calculating the magnetic interaction, (b) frequency or amplitude shift in dynamic mode MFM.¹⁴

Magnetic force microscopy (MFM) detects the force (or force derivate) acting on a small magnetic probe in the stray field close to the specimen, giving a resolution below 20 nm for the magnetic domain imaging.¹⁵ Figure 2-11a shows the

magnetostatic dipole-dipole interaction that leads to measurable forces and force gradients. The force dF_{mag} acting on a volume element dV' of the tip is given¹⁴

$$dF_{\text{mag}} = \nabla_r [M^T(r') \cdot H(r + r')] dV' \quad (2.1)$$

Where $M^T(r')$ is the magnetization of the volume element in the tip, and $H(r + r')$ the is sample stray field; r and r' present the apex and internal coordinate of the tip, respectively.¹⁶ The total force and force gradient acting on the tip can be calculated by integrating Eq (2.1). In the dynamic mode MFM, the cantilever is oscillated at or close to its resonance frequency. When the cantilever experience a force gradient produced by the tip-sample interaction, the cantilever behaves as if it has a modified spring constant, resulting in a shift in the resonant frequency (Fig 2-11b). Correspondingly, the change in the magnetic force exerted on the tip produces changes in resonance frequency, amplitude, and phase of cantilever oscillations, which are all measurable. In this thesis, using the tapping lift mode with a second scan separation above 10 nm and phase detection, the magnetic domain structure of FePt/NiO bilayers and FePt_{0.9}O_{0.1}/NiO/FePt_{0.9} trilayers were studied by MFM. Figure 2-12 shows the MFM image of standard sample.

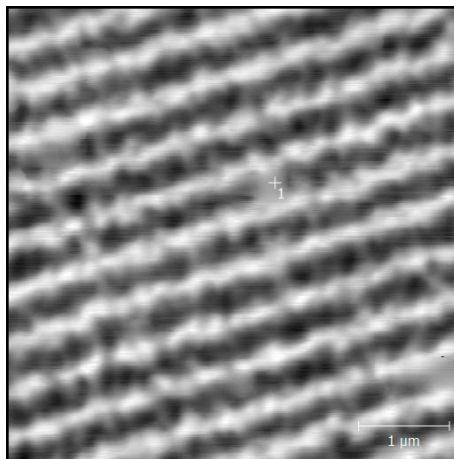


FIG 2-12 MFM image of standard sample (magnetic tape).

References

- ¹Milton Ohring, *Materials Science of Thin Films* (2002).
- ²Mario Birkholz, *Thin Film Analysis by X-Ray Scattering*, Wiley-VCH (2006).
- ³David B. Williams, and C. Barry Carter, *Transmission Electron Microscopy*, Springer (2009).
- ⁴Takemi Yamada, *J. Phys. Soc. Jpn.* **18**, 520 (1963).
- ⁵S. Saito, M. Miura, and K. Kurosawa, *J. Phys. C* **13**, 1513 (1980).
- ⁶H. Ohldag, A. Scholl, F. Nolting, S. Anders, F. U. Hillebrecht, and J. Stöhr, *Phys. Rev. Lett.* **86**, 2878 (2001).
- ⁷Hisamoto Kondoh, *J. Phys. Soc. Jpn.* **15**, 1970 (1960).
- ⁸E. Uchida, N. Fukuoka, H. Kondoh, T. Takeda, Y. Nakazumi, and T. Nagamiya, *J. Phys. Soc. Jpn.* **23**, 1197 (1967).
- ⁹M. T. Hutchings, and E. J. Samuelsen, *Phys. Rev. B* **6**, 3447 (1972).
- ¹⁰Simon Foner, *Rev. Sci. Instrum.* **27**, 548 (1956).
- ¹¹A. Niazi, P. Poddar and A. K. Rastogi, *Current Science* **79**, 99 (2000).
- ¹²Sóshin Chikazumi, *Physics of Ferromagnetism*, Oxford Science (1997).
- ¹³J. Clarke, *Proc. IEEE.* **61**, 8 (1973).
- ¹⁴P. Grütter, D. Rugar, and H. J. Mamin, *Ultramicroscopy* **47**, 393 (1992).
- ¹⁵Steffen Porthun, Leon Abelman, and Cock Lodder, *J. Magn. Magn. Mater.* **182**, 238 (1998).
- ¹⁶D. Rugar, H. J. Mamin, P. Guethner, S. E. Lambert, J. E. Stern, I. R. McFadyen, and T. Yogi, *J. Appl. Phys.* **68**, 1169 (1990).

Chapter 3 Effect of nitrogen upon structural and magnetic properties of FePt in FePt/AlN multilayer structures

3.1 Introduction

The L1₀-ordered FePt films possessing a face-centered tetragonal (fct) structure have drawn considerable research interest as a potential candidate for ultrahigh-density recording media because of their high magnetocrystalline anisotropy (7×10^6 J/m³)^{1,2} and good corrosion resistance. To use FePt alloys in perpendicular recording media applications, the alignment of the magnetic easy axis [001] must be parallel to the film normal. Because FePt thin films directly deposited on polycrystalline or amorphous substrates prefer to grow in a (111) texture, a great deal of work has been devoted on the deposition of c-axis-oriented L1₀-ordered films. Previous reports have shown that the (001) texture can be obtained either by epitaxial³⁻⁵ or nonepitaxial methods.⁶⁻⁸ However, because of its simple process and low expense, the nonepitaxial method is more attractive for practical applications. The main task then becomes the suppression of the tendency for (111) oriented grain growth in the nonepitaxial method, and the facilitation of the (001) texture. Thus, it is important to investigate the evolution mechanism of the (111) texture and to understand the influential factors in detail.

In magnetic recording media, a small magnetic thickness ($M_r t$; where M_r is the remnant moment and t is the magnetic layer thickness) results in the reduction of the transition parameter, which allows for the detection of transitions at higher linear densities and thereby increases the areal density.⁹ Since the magnetic moment in FePt alloys is about 3–4 times larger than the currently used CoCrPt alloys, L1₀ FePt films

can be physically thinner (~3–5 nm).¹⁰ Therefore, it is essential to study the magnetic and structural properties of ultrathin FePt films. In our previous work,^{11,12} we successfully fabricated metal/ceramic multilayer structures that form sharp and abrupt interfaces even after high-temperature annealing. Because the interface effect and strain/stress state are significant in such multilayer thin films owing to the structural interaction between the metal and ceramics layers, the structural characteristics of the multilayer structures provide an efficient method to study the effect of the interfaces and strain/stress in ultrathin metal layers. In addition, it has been reported that a small amount of nitrogen can exist in FePt films deposited in an argon and nitrogen atmosphere after high-temperature annealing,^{13,14} which can act as an interstitial atom to change the strain/stress state.

In this chapter, the effect of the introduction of interstitial nitrogen atoms upon structural and magnetic properties of FePt in FePt/AlN ultrathin multilayer structures was studied. To understand the influence of the interstitial atoms, we vary the layer thickness and annealing temperature and measure induced strain and magnetic properties. Using the results from this systematic study, we discuss the influential factors of the (111) texture evolution and ordering phase transformation.

3.2 Fabrication of FePt/AlN multilayer films

Multilayer films comprising substrate/AlN(5 nm)/[FePt(t)/AlN(6 nm)]₅ were fabricated at the ambient temperature by direct current magnetron sputtering on fused quartz substrates. The base pressure of the system was held below 5×10^{-5} Pa, and a high-purity gas mixture with Ar and N₂ at 0.5 Pa pressure was flowed into the chamber during the sputtering. For FePt deposition, a Fe target with a Pt chip on the top was used, and the N₂ ratio (0%, 24%) was varied in the sputtering gas. The

composition of the FePt layers was kept as $\text{Fe}_{53}\text{Pt}_{47}$ ($\pm 2\%$), as determined by inductively coupled plasma spectrometry (ICP). The AlN layers of the wurtzite structure were deposited by reactive sputtering from metallic Al targets. In order to trigger the FePt ordering phase transformation and study the effect of stress evolution in FePt layer, post-deposition annealing was performed in vacuum (below 1×10^{-4} Pa) at different temperatures for 3 h. A vibrating sample magnetometer with a maximum applied field of 15 kOe was used to measure the hysteresis loops. The structural characterization including the preferred growth orientation, in-plane strain, and degree of order in FePt layer was investigated by X-ray diffraction (XRD). The layer thickness of multilayer films was determined by X-ray reflectivity (XRR) measurements.

3.3 Structural characterization

3.3.1 X-ray reflectivity (XRR) patterns

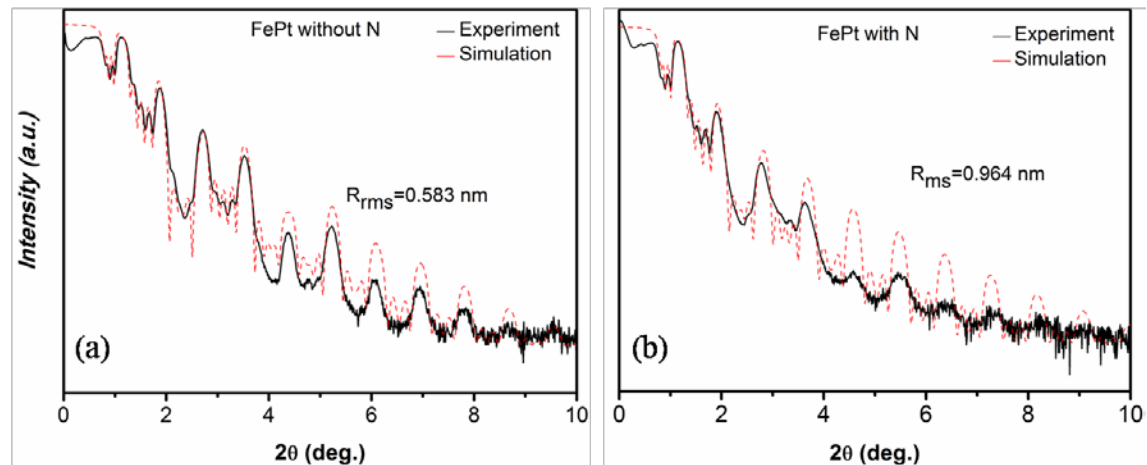


FIG 3-1 XRR patterns of AlN(5 nm)/[FePt(4 nm)/AlN(6 nm)]₅ films annealed at 600°C for 3 h, where the FePt layer was deposited (a) without and (b) with nitrogen. The black patterns are the experimental results, while the red dashed patterns are the simulative results given by LEPTOS software.

Figure 3-1 shows typical XRR patterns for AlN(5 nm)/[FePt(4 nm)/AlN(6 nm)]₅ films annealed at 600°C for 3 h. The layer thickness and interface roughness are obtained by fitting the experimental pattern using LEPTOS software with a simulated annealing method. Very clear XRR oscillations are observed for both samples, in which the FePt layer was deposited without (Fig 3-1a) and with (Fig 3-1b) nitrogen, respectively. Well-defined interfaces are required to produce such oscillations, indicating that the multilayer structure is very stable even annealed at high temperature. It is worth noting that this feature allows the study of FePt ordering in FePt/AlN multilayer structures. In consideration of interface roughness, one may also notice that compared with the case of FePt deposited without nitrogen, it shows a relatively rougher interface for that of FePt deposited with nitrogen.

3.3.2 Conventional XRD profiles

Figure 3-2 shows the XRD profiles of AlN(5 nm)/[FePt(4 nm)/AlN(6 nm)]₅ multilayer films containing FePt layers deposited without and with nitrogen, and annealed at different temperatures for 3 h. In the multilayer structures, the AlN and FePt layers exhibit a preferred orientation along the [002] and [111] directions, respectively. The FePt 111 reflections show satellite peaks around the central peak owing to the periodicity of the FePt/AlN multilayer structure. The intensity of the FePt 111 peaks increases with the annealing temperature, indicating that the crystallinity improves with annealing. Furthermore, the samples with FePt deposited with nitrogen (Fig 3-2b) exhibit shifts in the FePt 111 peak to high angles with increasing annealing temperature. Because the formation enthalpy of FePt is lower than that of the FeN alloy,¹³ the absence of an iron nitride peak in the films annealed at 500 and 600°C indicates that no iron nitride phase exists in the FePt layers, which is

in agreement with previous reports.^{13,15} Another earlier report¹⁴ demonstrated that, even after annealing FePt films at 600°C, 4% of the nitrogen remains. Thus, the nitrogen atoms are believed to be dissolved interstitially in the FePt layers of our annealed films. Because the incorporated N atoms induce lattice expansion while the lattice is restricted in in-plane directions by the AlN interfaces, a compressive stress is predicted to be induced. Therefore, the peak shift in Fig 3-2b can be attributed to the release of the N interstitial atoms during high temperature annealing.

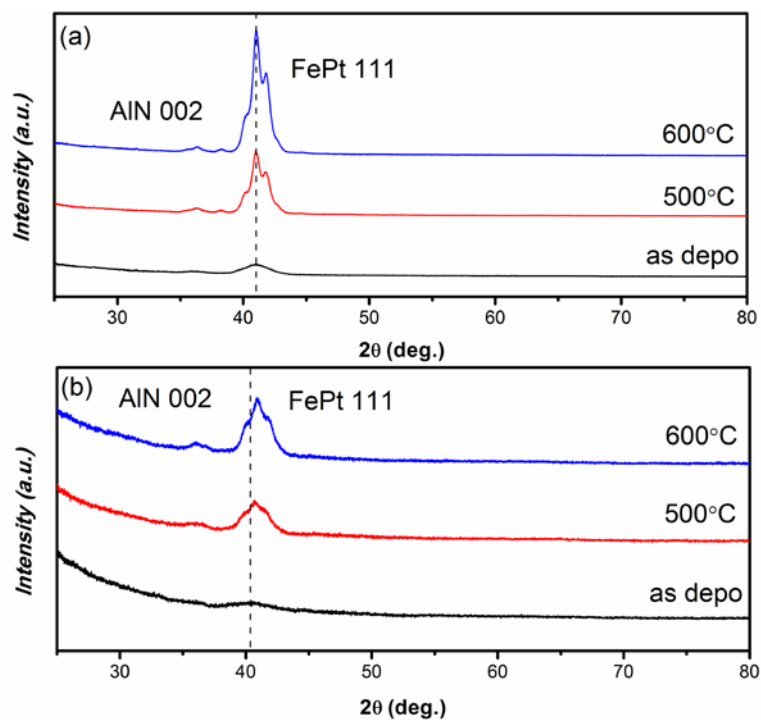


FIG 3-2 Conventional θ - 2θ XRD profiles of AlN(5 nm)/[FePt(4 nm)/AlN(6 nm)]₅ films annealed at different temperatures for 3 h, where the FePt layers are deposited (a) without nitrogen and (b) with nitrogen. The dashed lines show the peak shift.

3.3.3 Determination of in-plane strain in FePt layer

To further investigate the role of in-plane compressive stress during grain growth, we compare the different stress states caused by N addition. Since the FePt ultrathin layers are highly (111) textured, it is reasonable to assume a state of equal

biaxial stress. The measured strain can then be expressed as¹⁶

$$\varepsilon_{\psi} = \frac{d_{\psi} - d_0}{d_{\psi}} = \sigma_{//} \left(\frac{1+\nu}{E} \sin^2 \psi - \frac{2\nu}{E} \right) \quad (3.1)$$

where ε_{ψ} is the measured strain, d_{ψ} and d_0 are the measured and unstrained interplanar distance, respectively, $\sigma_{//}$ is the in-plane stress, ψ is the tilting angle of the film normal with respect to the x-ray incident plane, E is the Young's modulus, and ν is the Poisson's ratio. By using Eq. (3.1) with the correct values for Young's modulus (180 GPa) and Poisson's ratio (0.33),¹⁷ the in-plane strain (ε) of films annealed at 600°C is

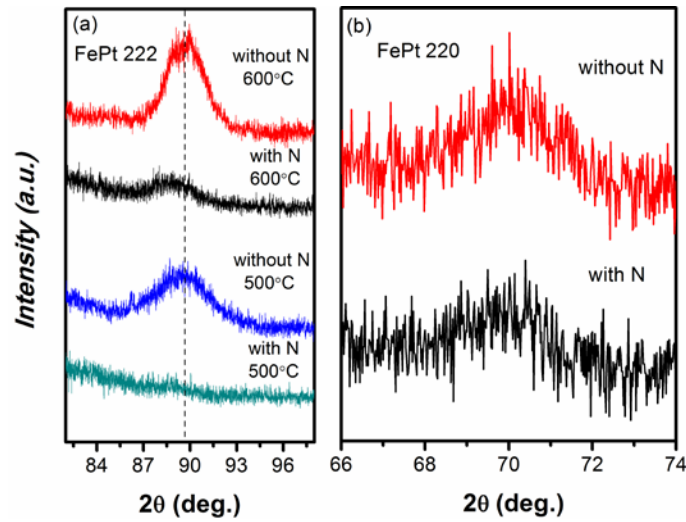


FIG 3-3 (a) Conventional θ -2 θ XRD profiles of AlN(5 nm)/[FePt(4 nm)/AlN(6 nm)]₅ films annealed at 500 and 600°C for 3 h. (b) XRD profiles by tilting (36.264°) scan of AlN(5 nm)/[FePt(4 nm)/AlN(6 nm)]₅ films annealed at 600°C for 3 h.

obtained based upon the 222 and 220 peaks at different tilt angles in Figs. 3-3a and 3-3b, with values of -0.874% and 0.083% for FePt deposited with and without nitrogen, respectively. To estimate ε at the temperature of the grain growth, the measured data was corrected by subtracting the thermal strain, which can be written as $\varepsilon = \Delta T \Delta \alpha$, where $\Delta \alpha$ is the difference in the thermal expansion coefficient values of the AlN and FePt layers. The corrected ε at 600°C is obtained as -1.22% and -0.26% for the FePt deposited with and without nitrogen, respectively. It can be seen that the FePt

deposited with nitrogen experiences much more in-plane compressive strain during grain growth.

3.3.4 Effect of in-plane strain on FePt (111) texture

The structural change seen with the introduction of nitrogen is a weaker (111) texture than that of FePt deposited without nitrogen (Fig 3-3a). This change can be interpreted by grain-orientation-specific driving forces for grain growth. Because of the enhancement of the interface effect and the stress state in ultrathin multilayer structures, FePt grain growth is believed to progress through abnormal grain growth. The driving force (F) for abnormal grain growth may arise from changes in the interface and strain energies, following the relationship:^{18,19}

$$F = \kappa + \Gamma + F_{\epsilon} \quad (3.2)$$

where κ and Γ are the local in-plane and out-of-plane curvatures of the grain boundary, respectively, and F_{ϵ} is the strain energy difference. Because our FePt layers exhibit strong (111) texture, the driving force for FePt (111) grain growth is then taken to be^{18,19}

$$F = \kappa + \frac{1}{\gamma_{gb}} \left[\frac{2(\gamma_0 - \gamma_{111})}{h} + (M_0 - M_{111})\epsilon^2 \right] \quad (3.3)$$

where γ_0 and γ_{111} are the interface energies before grain growth and of grains with (111) orientation, respectively; M_0 and M_{111} are the biaxial moduli before grain growth and of grains with (111) orientation, respectively; h is the FePt layer thickness; and γ_{gb} is the grain boundary energy. In this equation, the second and third terms present the change in interface energy and strain energy, respectively. For facecentered cubic (fcc) metals, minimization of the elastic strain energy generally results in a (100) texture, which is different from the (111) texture that typically

occurs with surface/interface energy minimization. Therefore, the strain energy change and the surface/interface energy change competes to define the final texture resulting from grain growth.¹⁹⁻²¹ It is known that for fcc polycrystalline films, the maximum strain energy density corresponds to those grains with (111) planes oriented parallel to the film plane,²² which indicates that the third term in Eq. (3.3) should be negative. Therefore, as indicated by Eq. (3.3), an increase of compressive strain during grain growth may result in a decrease in the driving force for the (111) grain growth, which would explain the weaker (111) texture of FePt deposited with nitrogen.

3.3.5 Grazing incidence in-plane XRD profiles

It is known that the $L1_0$ ordering of FePt leads to a tetragonal distortion, in which the lattice constant a is equal to b and slightly larger than c . As a consequence, it is expected to observe a split of $(2\bar{2}0)$ and $(20\bar{2})$ peak for ordered FePt in XRD profile. As seen in the in-plane XRD profiles, for AlN(5 nm)/[FePt(4 nm)/AlN(6 nm)]₅ annealed at 500°C, the unsplit $(2\bar{2}0)$ peak (see Fig 3-4) indicates the FePt layer is weakly ordered. With increasing the annealing temperature from 500 to 700°C, it can be clearly observed that the fcc $(2\bar{2}0)$ peak splits into the $L1_0$ $(2\bar{2}0)$ and $(20\bar{2})$ peaks, which signals the presence of significant chemical order. Since both superlattice FePt (110) and AlN (100) peak are located around $2\theta = 33^\circ$,²³ the AlN (002) and FePt (111) texture in FePt/AlN multilayer film give rise to the overlap for this two peaks in the in-plane XRD profile and can hardly be distinguished. Unfortunately, we cannot estimate the degree of order in FePt layer by using in-plane XRD. Besides, it should also be noted that this measurement was conducted under the scanning type of detector scan, suggesting that the FePt grains are randomly distributed in the film

plane without certain in-plane growth direction.

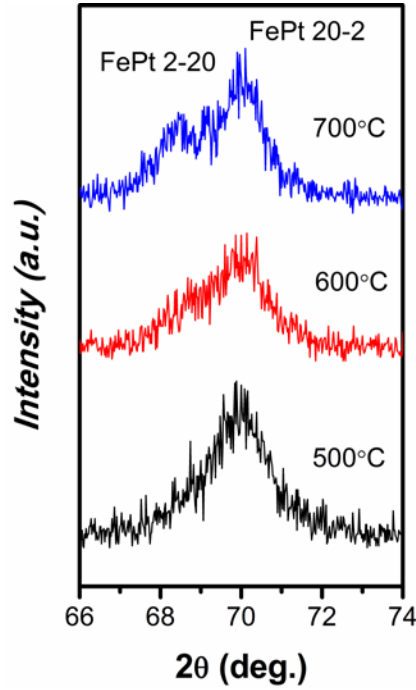


FIG 3-4 Grazing incidence in-plane XRD profiles of AlN(5 nm)/[FePt(4 nm)/AlN(6 nm)]₅ films annealed at different temperatures for 3 h.

3.3.6 Calculation of long range order parameter S ^{24,25}

The degree of chemical ordering is defined as a long range order parameter S which is linearly proportional to $(r_\alpha + r_\beta)$, where r_α and r_β denote the α -site and β -site occupied by the right atom, respectively. $S = 0$ for a completely random arrangement, and $S = 1$ if the composition is stoichiometric and $r_\alpha = r_\beta = 1$. Expressing the linear dependence by $S = a + b(r_\alpha + r_\beta)$, the first condition gives $0 = a + b(x_A + x_B) = a + b$, and the second condition gives $1 = a + 2b$. Eliminating the constants a and b , the long range order parameter is expressed in this form:

$$S = r_\alpha + r_\beta - 1 = r_\alpha - w_\beta = r_\beta - w_\alpha \quad (3.4)$$

Where w_α and w_β are the fraction of α -site and β -site occupied by the wrong atom.

There are also some conditions we should note that the fraction of the sites occupied

by A-atoms must equal the fraction of A-atoms, and the fraction of the sites occupied by B-atoms must equal the fraction of B-atoms. These two equivalent conditions are expressed by:

$$y_{\alpha}r_{\alpha} + y_{\beta}w_{\beta} = x_A \quad y_{\beta}r_{\beta} + y_{\alpha}w_{\alpha} = x_B \quad (3.5)$$

The parameter S can reach its maximum value of the unity only for a stoichiometric composition, for a nonstoichiometric composition even the best distribution of the available atoms gives a parameter value, which is less than unity. With this definition for S , the structure factors for the super structure reflections turn out to be proportional to S even for nonstoichiometric compositions, and hence a general parameter S^2 is obtain from experiment.

The structure factor involves a sum over all the atomic positions in the unit cell. This can be divided into a sum over the α -positions and a sum over the β -positions using the average scattering factor for each kind of site:

$$F = \sum_{\alpha} (r_{\alpha}f_A + w_{\alpha}f_B) \exp[2\pi i(hx_n + ky_n + lz_n)] \\ + \sum_{\beta} (r_{\beta}f_B + w_{\beta}f_A) \exp[2\pi i(hx_n + ky_n + lz_n)] \quad (3.6)$$

For the case of partial long range order, we now apply Eq (3.6) to the FePt ordered structures without assuming stoichiometric compositions. Simplification of the expressions is made by using Eqs (3.4) and (3.5):

Fe-site = 0 0 0, 1/2 1/2 0; Pt-site = 1/2 0 1/2, 0 1/2 1/2; $y_{Fe} = 1/2$; $y_{Pt} = 1/2$

$$F = (r_{Pt}f_{Pt} + w_{Pt}f_{Fe}) \left\{ \exp[\pi i(h+l)] + \exp[\pi i(k+l)] \right\} \\ + (r_{Fe}f_{Fe} + w_{Fe}f_{Pt}) \left\{ 1 + \exp[\pi i(h+k)] \right\} \quad (3.7)$$

For the Fundamental peak, hkl are unmixed. Therefore, F_f can be expressed as:

$$F_f = \left[(r_{Pt}f_{Pt} + w_{Pt}f_{Fe}) + (r_{Fe}f_{Fe} + w_{Fe}f_{Pt}) \right] = 4(x_{Fe}f_{Fe} + x_{Pt}f_{Pt}) \quad (3.8)$$

For the superlattice peak, hkl are mixed. F_s can be expressed as:

$$F_s = 2[(r_{Pt}f_{Pt} + w_{Pt}f_{Fe}) - (r_{Fe}f_{Fe} + w_{Fe}f_{Pt})] = 2S(f_{Pt} - f_{Fe}) \quad (3.9)$$

Reflections that are independent of the degree of the order are called fundamental reflections, and reflections which vanish if the order vanishes are called superstructure reflections. The existence of superstructure reflections is the evidence for ordering, and it is from the integrated intensities of the superstructure reflections that we measure the long range order parameter S .

Before the determination of S , an assumption has been made in our multilayer structures. We suppose that the films are relatively thick with a sufficiently smooth surface. Therefore, the absorption correction can be regarded as no angular dependence and the area of a peak is expressed as:

$$A = Km(LP)FF^* \quad (3.10)$$

Here K is a constant; m is multiplicity; (LP) is Lorentz-polarization factor, F and F^* are the structure factor and its complex conjugate. By Substituting Eqs (3.8) and (3.9), respectively, the product of FF^* for the fundamental and superlattice peak are represented by:

$$(FF^*)_f = 16\{[x_{Fe}f_{Fe} \exp(-M_{Fe}) + x_{Pt}f_{Pt} \exp(-M_{Pt})]^2 + [x_{Fe}\Delta_{Fe} \exp(-M_{Fe}) + x_{Pt}\Delta_{Pt} \exp(-M_{Pt})]^2\} \quad (3.11)$$

$$(FF^*)_s = 4S^2\{[f_{Pt} \exp(-M_{Pt}) - f_{Fe} \exp(-M_{Fe})]^2 + [\Delta_{Pt} \exp(-M_{Pt}) - \Delta_{Fe} \exp(-M_{Fe})]^2\} \quad (3.12)$$

Where x_{Fe} and x_{Pt} are the atomic fraction of Fe and Pt; f_{Fe} and f_{Pt} are the atomic scattering factor with dispersion correction; Δ_{Fe} and Δ_{Pt} are the imaginary parts of atomic scattering factor of Fe and Pt atoms; $\exp(-M_{Fe})$ and $\exp(-M_{Pt})$ are the Debye factors of Fe and Pt atoms.

For our FePt layers, we use superlattice peak (110) and fundamental peak (220) to determine the chemical order parameter S . By utilizing Eqs (3.10), (3.11) and (3.12), the chemical order parameter S can finally formulized as

$$S^2 = \frac{A_{(110)}(LP)_{(220)} FF_{(220)}^*}{A_{220}(LP)_{(110)} FF_{(110)}^*} \quad (3.13)$$

3.4 Magnetic properties of FePt/AlN multilayer films

3.4.1 Annealing temperature dependence of coercivity and degree of FePt order in FePt/AlN multilayer films

The ordered phase of FePt is characterized by XRD scans with the film normal tilted by 36.264° with respect to the x-ray incident plane (denote as tilting scan), as shown in Fig 3-5a. Because our FePt layers exhibit strong (111) texture, the superlattice peaks of $L1_0$, such as (110), cannot be detected by conventional $\theta/2\theta$ XRD. To show the quantitative results of the chemical order in the FePt layers, the degree of chemical order, namely, long range order parameter S is estimated by using Eq (3.13) and some parameters have been listed in Table (3-1). The integrated

Table 3-1 Parameter used to estimate the long range order parameter S of FePt.

Peak	$Q(\text{\AA}^{-1})$	LP	M_{Fe}	f_{Fe}	Δ_{Fe}	M_{Pt}	f_{Pt}	Δ_{Pt}
(110)	2.295	11.21	0.01	19.61	3.4	0.01	61.37	8
(220)	4.682	2.06	0.04	13.54	3.3	0.04	47.39	7

intensities of the superlattice and fundamental peaks are extracted using pseudo-Voigt fitting, as shown in Fig 3-5b. Note that since fcc (220) and $L1_0$ (220) and (202) cannot

be distinguished in Figs 3-5a and 3-5b, the calculated S here is a product of the degree of chemical order in the ordered regions and the volume fraction of the ordered phase. Figure 3-5c depicts the dependence of the in-plane coercivity (H_c) and the long-range order parameter (S) upon the annealing temperature for AlN(5 nm)/[FePt(4 nm)/AlN(6 nm)]₅ films, where the FePt layer is deposited without nitrogen. When the annealing temperature increases from 500 to 700°C, S rapidly increases from 0.337 to 0.743, which is similar to the annealing temperature dependence of H_c . It has been

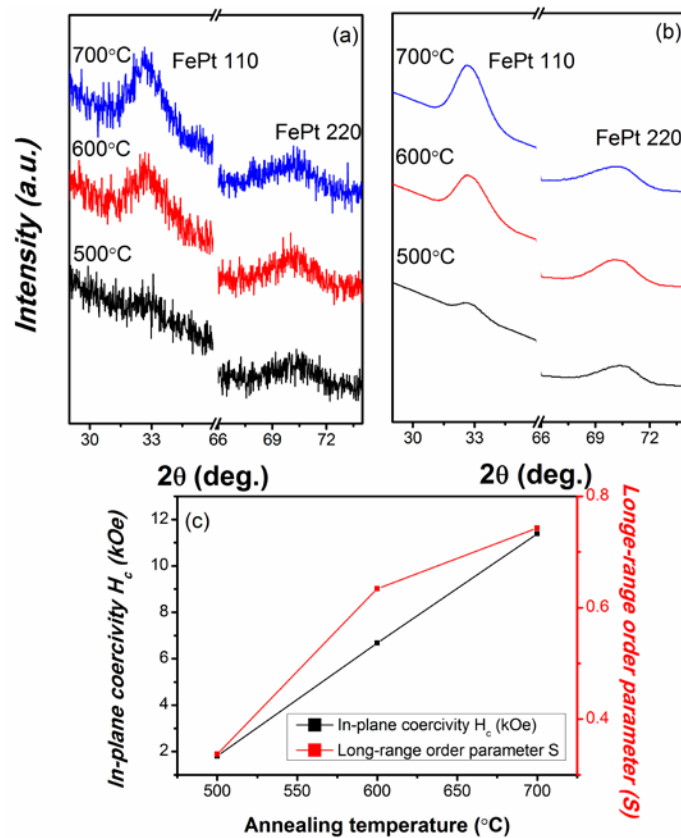


FIG 3-5 (a) XRD profiles by tilting (36.264°) scan and (b) Pseudo-Voigt fitting curves of AlN(5 nm)/[FePt(4 nm)/AlN(6 nm)]₅ films annealed at different temperatures for 3 h, where the FePt layers are deposited without nitrogen. (c) The long-range order parameter and in-plane coercivity as a function of the annealing temperature.

previously demonstrated that the coercivity of FePt films increases with the volume fraction of the ordered phase with respect to the disordered phase.^{15,26} These results

prove that H_c can be used to qualitatively estimate the ordering of FePt. Because the introduction of nitrogen results in a weaker (111) texture and more randomly oriented grains, the XRD by tilting scan is not sufficient to evaluate S for entire layers in this case. Therefore, we mainly use coercivity to qualitatively estimate the ordering for FePt deposited with and without nitrogen.

3.4.2 Effect of nitrogen on magnetic properties for FePt layer in FePt/AlN multilayer films

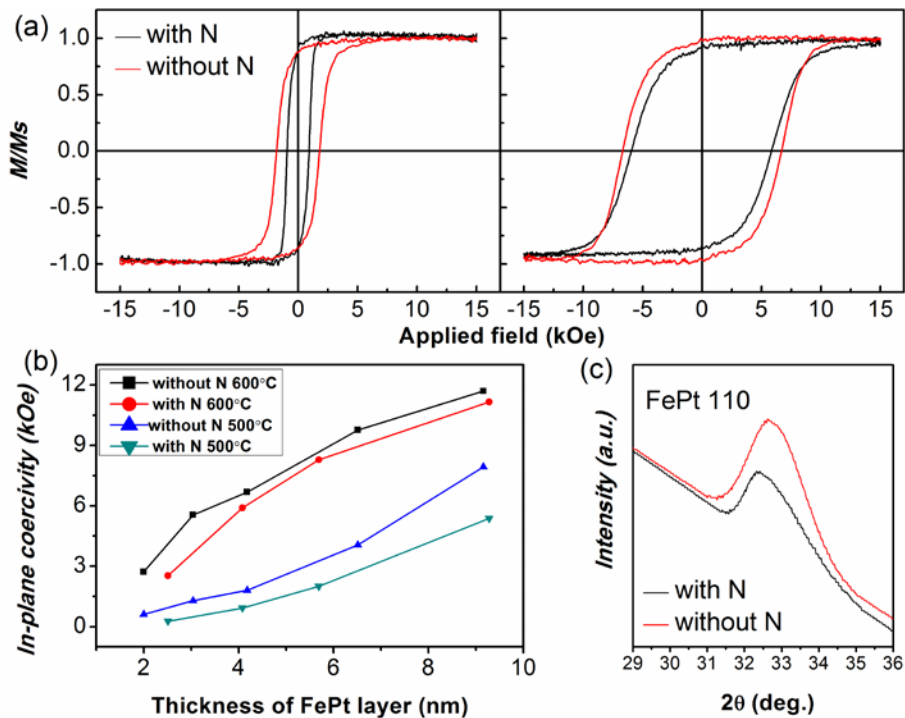


FIG 3-6 (a) Magnetic hysteresis loops of AlN(5 nm)/[FePt(4 nm)/AlN(6 nm)]₅ films annealed at 500 and 600°C for 3 h. (b) In-plane coercivity of AlN(5 nm)/[FePt(t nm)/AlN(6 nm)]₅ films annealed at 500 and 600°C for 3 h as a function of FePt layer thickness. (c) Pseudo Voigt fitting curves of AlN(5 nm)/[FePt(4 nm)/AlN(6 nm)]₅ films annealed at 600°C for 3 h, where the FePt layers are deposited without and with nitrogen.

Figure 3-6a shows the magnetic hysteresis loops of AlN(5 nm)/[FePt(4

nm)/AlN(6 nm)]₅ films annealed at 500 and 600°C for 3 h. After annealing, the coercivity is enhanced and increased with the annealing temperature owing to the ordering of FePt. For comparison, collecting the data from Figs 3-6a, 3-7, 3-8, 3-9, and 3-10, the in-plane coercivity of FePt deposited with and without nitrogen for various layer thicknesses are summarized in Fig 3-6b, where the multilayer films are again annealed at 500 and 600°C for 3 h. It can be observed that, in the entire thickness range, the H_c of FePt deposited with nitrogen is lower than that deposited without nitrogen. One possible explanation for the enhanced coercivity of the FePt thin films is the presence of pinning sites, including pinning at the boundaries between fcc and fct phases²⁶ or at planar defects.²⁷ It has been reported that a more random structure would result in a large-angle grain boundary, which can act as a pinning site.¹⁵ However, as seen in Fig. 3-6a, the FePt deposited with nitrogen possesses much more randomly oriented grains. Therefore, the relatively lower coercivity of FePt deposited with nitrogen is more likely owing to the smaller volume fraction of the ordered phase.

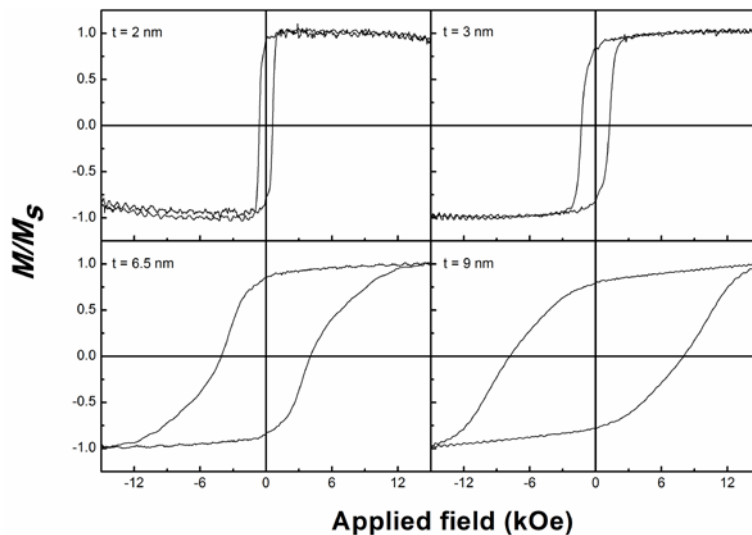


FIG 3-7 In-plane hysteresis loops of AlN(5 nm)/[FePt(t nm)/AlN(6 nm)]₅ films with varying FePt layer thickness. The multilayer films were annealed at 500°C for 3 h and FePt layer was deposited without nitrogen.

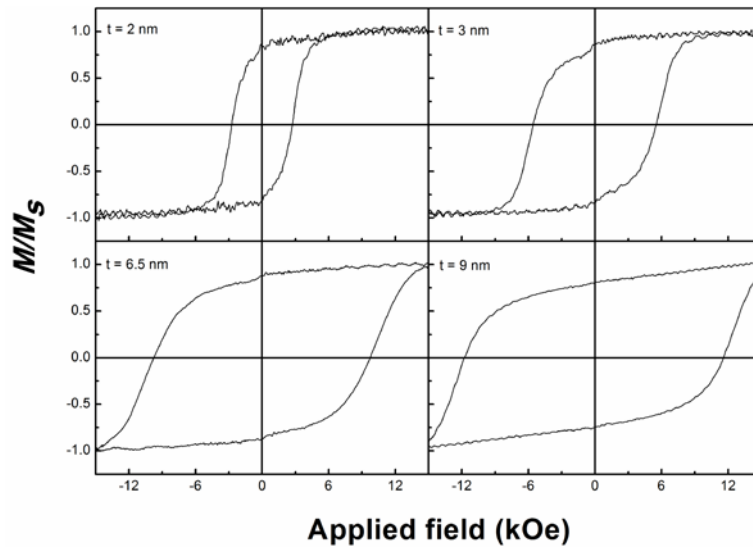


FIG 3-9 In-plane hysteresis loops of AlN(5 nm)/[FePt(t nm)/AlN(6 nm)]₅ films with varying FePt layer thickness. The multilayer films were annealed at 600°C for 3 h and FePt layer was deposited without nitrogen.

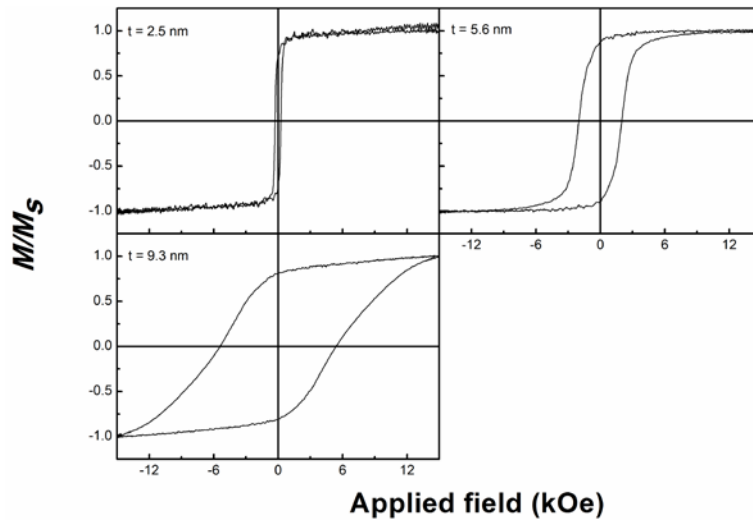


FIG 3-8 In-plane hysteresis loops of AlN(5 nm)/[FePt(t nm)/AlN(6 nm)]₅ films with varying FePt layer thickness. The multilayer films were annealed at 500°C for 3 h and FePt layer was deposited with nitrogen.

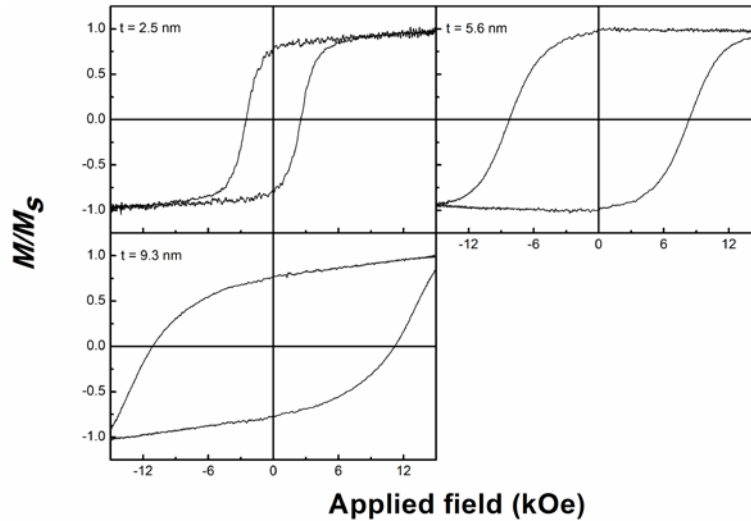


FIG 3-10 In-plane hysteresis loops of AlN(5 nm)/[FePt(*t* nm)/AlN(6 nm)]₅ films with varying FePt layer thickness. The multilayer films were annealed at 600°C for 3 h and FePt layer was deposited with nitrogen.

It is well known that the disorder–order transformation in FePt is a first-order reaction, proceeding from a nucleation and growth mechanism.^{28,29} In addition, Takahashi and Hono reported that the ordering of FePt thin films was thought to progress by abnormal grain growth below a $T_m/2$ (where T_m is the disorder–order transformation temperature in the solid Fe–Pt binary system) of $\sim 600^\circ\text{C}$.³⁰ Because of the characteristics of ultrathin multilayer structures, the ordering of FePt in our case is also thought to progress by abnormal grain growth for films annealed at 500 and 600°C. The driving force may arise from the excess free energy associated with grain boundaries, interface energy and strain energy. Because our FePt layers exhibit a strong (111) texture, recrystallization chiefly progresses via (111) oriented grains consuming unfavored grains. For FePt deposited with nitrogen, a decrease of the driving force for (111) grain growth can be expected, and some L1₀-ordered regions may not continue to grow owing to the lack of a driving force, which can be confirmed by the weaker superlattice peak seen in Fig. 3-6c. This effectively explains

the smaller volume fraction of the ordered phase with N addition. Since abnormal grain growth is dominant for low-temperature ordering in FePt continuous films,³⁰ a larger discrepancy of coercivity can be observed in films annealed at 500°C, as shown in Fig. 3-6b. Meanwhile, Hsiao *et al.* also reported that the large initial compressive stress suppresses the ordering of FePt,³¹ and they attributed the decrease of the chemical order to an increase in the activation energy of the ordering phase transformation.

3.5 Summary

In summary, the changes in the structural and magnetic properties of FePt/AlN multilayer structures with the addition of N during growth are studied, and the mechanism of the N effect is discussed. The nitrogen atoms are believed to exist as interstitial atoms in the FePt layers, which induce a large in-plane compressive strain during grain growth and ordering phase transformation. The results suggest that this strain creates a weaker FePt (111) texture and a smaller volume fraction of the ordered phase because of the decrease in the driving force for (111) grain growth. Because the changes in the strain and surface/interface energies compete to define the final texture, one promising way to achieve a (001) texture and low-temperature ordering via the nonepitaxial method would be to reduce the surface/interface energy and to introduce a large in-plane tensile strain during the ordering phase transformation.

References

- ¹C. Feng, B.-H. Li, Y. Liu, J. Teng, M.-H. Li, Y. Jiang, and G.-H. Yu, *J. Appl. Phys.* **103**, 023916 (2008).
- ²K. Barmak, J. Kim, L. H. Lewis, K. R. Coffey, M. F. Toney, A. J. Kellock, and J.-U. Thiele, *J. Appl. Phys.* **98**, 033904 (2005).
- ³C. Feng, Q. Zhan, B. Li, J. Teng, M. Li, Y. Jiang, and G. Yu, *Appl. Phys. Lett.* **93**, 152513 (2008).
- ⁴Y. Xu, J. S. Chen, and J. P. Wang, *Appl. Phys. Lett.* **80**, 3325 (2002).
- ⁵Z. L. Zhao, J. S. Chen, J. Ding, J. B. Yi, B. H. Liu, and J. P. Wang, *Appl. Phys. Lett.* **88**, 052503 (2006).
- ⁶T. Ichitsubo, S. Tojo, T. Uchihara, E. Matsubara, A. Fujita, K. Takahashi, and K. Watanabe, *Phys. Rev. B* **77**, 094114 (2008).
- ⁷T. Narisawa, T. Hasegawa, S. Ishio, and H. Yamane, *J. Appl. Phys.* **109**, 033918 (2011).
- ⁸S. N. Hsiao, S. H. Liu, S. K. Chen, F. T. Yuan, and H. Y. Lee, *J. Appl. Phys.* **111**, 07A702 (2012).
- ⁹A. Moser, K. Takano, D. T. Margulies, M. Albrecht, Y. Sonobe, Y. Ikeda, S. Sun, and E. E. Fullerton, *J. Phys. D: Appl. Phys.* **35**, R157 (2002).
- ¹⁰M. F. Toney, W.-Y. Lee, J. A. Hedstrom, and A. Kellock, *J. Appl. Phys.* **93**, 9902 (2003).
- ¹¹Y. Hodumi, J. Shi, and Y. Nakamura, *Appl. Phys. Lett.* **90**, 212506 (2007).
- ¹²Y. Yu, J. Shi, and Y. Nakamura, *Acta Mater.* **60**, 6770 (2012).
- ¹³V. Phatak, A. Gupta, V. R. Reddy, S. Chakravarty, H. Schmidt, and R. Ruffer, *Acta Mater.* **58**, 979 (2010).
- ¹⁴H. Y. Wang, W. H. Mao, X. K. Ma, H. Y. Zhang, Y. B. Chen, Y. J. He, and E. Y.

- Jiang, J. Appl. Phys. **95**, 2564 (2004).
- ¹⁵C. Y. You, Y. K. Takahashi, and K. Hono, J. Appl. Phys. **98**, 013902 (2005).
- ¹⁶B. D. Cullity, Elements of X-Ray Diffraction (Addison-Wesley, Reading, MA, 1956).
- ¹⁷P. Rasmussen, X. Rui, and J. E. Shield, Appl. Phys. Lett. **86**, 191915 (2005).
- ¹⁸R. Carel, C. V. Thompson, and H. J. Frost, Acta Mater. **44**, 2479 (1996).
- ¹⁹C. V. Thompson and R. Carel, Mater. Sci. Eng., B **32**, 211 (1995).
- ²⁰C. V. Thompson and R. Carel, J. Mech. Phys. Solids **44**, 657 (1996).
- ²¹L. B. Freund and S. Suresh, Thin Film Materials: Stress, Defect Formation and Surface Evolution (Cambridge University, Cambridge, 2003).
- ²²J.-M. Zhang, K.-W. Xu, and V. Ji, Appl. Surf. Sci. **185**, 177 (2002).
- ²³Wupeng Cai, Ji Shi, Yoshio Nakamura, Wei Liu, and Ronghai Yu, J. Appl. Phys. **110**, 073907 (2011).
- ²⁴B. E. Warren, X-Ray Diffraction (Dover, New York, 1990).
- ²⁵A. Cebollada, D. Weller, J. Sticht, G. R. Harp, R. F. C. Farrow, R. F. Marks, R. Savoy, and J. C. Scott, Phys. Rev. B **50**, 3419 (1994).
- ²⁶R. A. Ristau, K. Barmak, L. H. Lewis, K. R. Coffey, and J. K. Howard, J. Appl. Phys. **86**, 4527 (1999).
- ²⁷M. H. Hong, K. Hono, and M. Watanabe, J. Appl. Phys. **84**, 4403 (1998).
- ²⁸D. C. Berry and K. Barmak, J. Appl. Phys. **101**, 014905 (2007).
- ²⁹K. Barmak, R. A. Ristau, K. R. Coffey, M. A. Parker, and J. K. Howard, J. Appl. Phys. **79**, 5330 (1996).
- ³⁰Y. K. Takahashi and K. Hono, Scr. Mater. **53**, 403 (2005).
- ³¹S. N. Hsiao, F. T. Yuan, H. W. Chang, H. W. Huang, S. K. Chen, and H. Y. Lee, Appl. Phys. Lett. **94**, 232505 (2009).

Chapter 4 Off-easy-plane antiferromagnetic spin canting in coupled FePt/NiO bilayer structure with perpendicular exchange bias

4.1 Introduction

The interface interaction between ferromagnetic (FM) and antiferromagnetic (AFM) layers leads to the well-known exchange bias effect.¹ Although intensive research attention has been paid to explain the mechanism for this phenomenon since its discovery half a century ago,² the origin of exchange bias is still under debate. It firstly assumes a perfectly uncompensated AFM interface with collinear FM/AFM exchange coupling at the interface,³ and Mauri *et al.* pointed out that exchange bias occurs due to the formation of AFM planar domain wall as the FM magnetization is reversed.⁴ The reason for large discrepancy between actual and predicted value was further studied with the recognition, such as coupling frustration at FM/AFM interface,^{5,6} only a small percentage of uncompensated AFM spins contributing in the real cases,^{7,8} or partial wall formed in soft FM layer at the interface.⁹ Recently, orthogonal FM-AFM exchange coupling was realized in Fe/CoO^{10,11} and Fe/NiO^{12,13} structures as confirmed by AFM spin switching study using x-ray magnetic linear dichroism (XMLD), and this “spin flop” coupling has already been proposed from theoretical calculation for compensated AFM interface.^{5,14} Since the absence of unidirectional anisotropy,¹⁵ the mechanism of exchange bias in such coupling system cannot be explained by Maui’s model. While based on results of numerical simulation, the AFM spins should deviate slightly away from the easy axis direction (i.e., the

angle between FM and AFM spin is not exact 90°) due to the competing antiferromagnetic exchange between the two sublattices and ferromagnet.^{5,14,16} However, to our knowledge, this small deviating angle has rarely been considered or proved in real orthogonal FM-AFM coupling system. From recent studies, it is known that for the application of exchange bias effect in advanced spintronic devices, perpendicular exchange bias (PEB) is much more desirable.¹⁷⁻¹⁹ The out-of-plane alignment of FM spins can also facilitate the theoretical study of exchange bias, especially how the AFM spins affect the FM spin alignment during magnetization process in domain imaging experiments.^{8,20}

In this chapter, we present the study of perpendicular-exchange-biased FePt/NiO bilayers on MgO(001) single crystal substrate in which the $L1_0$ FePt exhibits strong perpendicular magnetic anisotropy. In this structure, any deviation of Fe spins from the normal direction may be considered caused by FM/AFM coupling. On the other hand, the interfacial spin configuration of NiO can be “visualized” through the magnetization of FePt. This means our structure and experimental approach offer a way to study the interfacial spin structure between FM and AFM. By comparing FePt single layer, FePt/NiO bilayers before and after perpendicular field cooling (FC), we observed that only the bilayer before FC experiences a small-angle magnetization rotation as it is magnetized near to saturation in normal direction. Meanwhile, after FC the bilayer shows a significant enhancement of perpendicular magnetic anisotropy. These findings provide experimental evidence that, for FM/AFM orthogonal coupling, the angle between FM and AFM spin is not exact 90° as predicted by theoretical calculation,^{5,14} which is expected to induce a unidirectional anisotropy in FM layer after FC.

4.2 Preparation of FePt/NiO bilayer structure on MgO(001) single crystal substrate

MgO(001) single crystal substrates were cleaned in ultrasonic baths of acetone and methyl alcohol and surface thermal cleaning was implemented in an ultrahigh vacuum system by annealing at 840 K for 90 min. Then samples of FePt(2.5 nm) single layer and FePt(2.5 nm)/NiO(21 nm) bilayers were grown epitaxially on MgO(001) substrates. The 2.5 nm thick FePt layer was grown by DC magnetron sputtering on top of MgO(001) substrate held at 620 K, followed by an in situ annealing at 840 K for 3 h to induce the $L1_0$ ordering. Our two-step preparation method is expected to prevent the island growth of FePt at high substrate temperatures.²¹ For FePt/NiO bilayers, a NiO(21 nm) layer was subsequently deposited on top of FePt layer at 500 K by DC reactive sputtering in a mixture atmosphere of Ar and O₂ gases (2% O₂). The structure of FePt single layer and FePt/NiO bilayers was characterized by X-ray diffraction (XRD) and X-ray reflectivity (XRR). Microstructural characterization was carried out by transmission electron microscopy (TEM). The magnetic properties were characterized by superconducting quantum interference device (SQUID) magnetometer. The magnetic domain imaging was performed at 300 K by magnetic force microscopy (MFM).

4.3 Determination of crystallographic orientation of FePt/NiO bilayer structure

4.3.1 Preferred growth orientation and chemical order in FePt layer

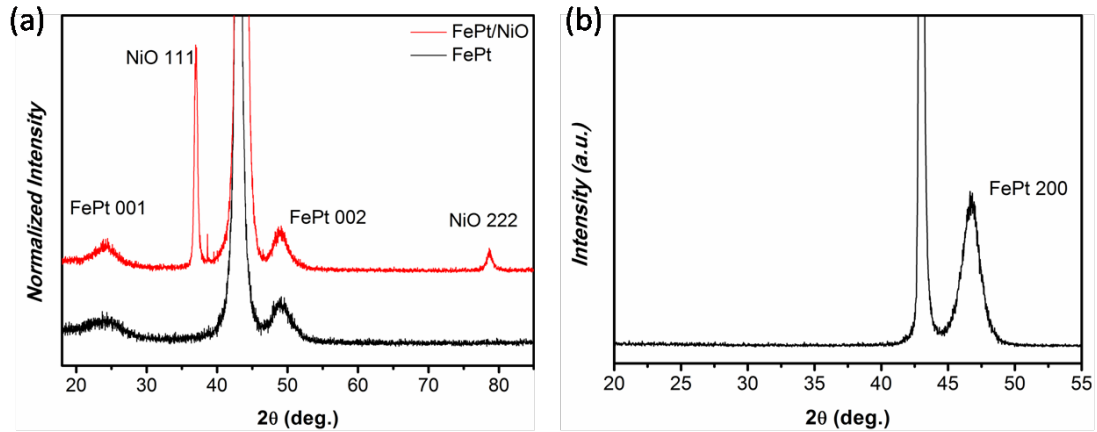


FIG 4-1 (a) Conventional $\theta/2\theta$ XRD profiles of FePt(2.5 nm) single and FePt(2.5 nm)/NiO(21 nm) bilayer structure grown on MgO(001) single crystal substrate. The XRD profiles are normalized to the FePt(002) peak. (b) Grazing incidence in-plane XRD profile of FePt(2.5 nm)/NiO(21 nm) bilayer structure and the x-ray scattering plane is nearly perpendicular to the FePt(200) plane.

Figure 4-1a shows conventional $\theta/2\theta$ XRD profiles of FePt(2.5 nm) single and FePt(2.5 nm)/NiO(21 nm) bilayer structure. For the FePt layer either in single or bilayer structure, the FePt(001) and FePt(002) peaks can be only observed, indicating a strong (001) texture. While for the NiO layer in FePt/NiO bilayer structure, a (111) texture is identified by the observed NiO(111) and NiO(222) peaks. In addition, the appearance of FePt(001) superlattice peak shows evidence of FePt ordering. The degree of order was estimated via ratio of integrated intensity of FePt(001) peak to that of (002) peak, and its value is 0.51 and 0.53 for the FePt in single and bilayer structure, respectively, suggesting that these two systems should possess same uniaxial magnetic anisotropy (K_u).²² To further study the growth orientation of FePt

layer, the in-plane XRD measurement was carried out as shown in Fig 4-1b. The absence of FePt(001) peak indicates that the c axis of FePt layer is well aligned in the film normal direction. This can also be confirmed by the relatively low 2θ position of FePt(200) peak compared with that of FePt(002) peak in Fig 4-1a.

4.3.2 In-plane crystallographic orientation of FePt/NiO bilayer structure and the cross-section TEM image

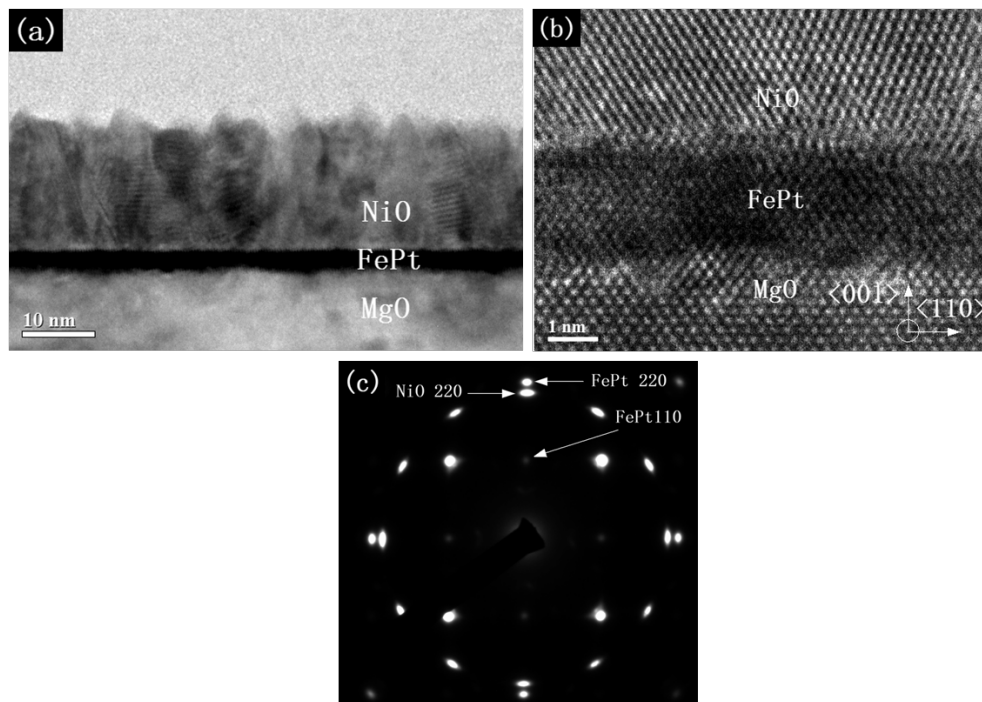


FIG 4-2 (a) Low magnification TEM micrograph of cross-sectional FePt/NiO bilayer structure. (b) Corresponding high resolution TEM image taken with MgO [110] as zone axis. (c) Plan-view selected-area electron diffraction pattern of FePt/NiO bilayer structure taken with FePt [001] as zone axis

Figure 4-2a shows a low magnification cross-section TEM image of FePt(2.5 nm)/NiO(21 nm) bilayer structure, which reveals that a continuous FePt layer with sharp FePt/NiO interface was formed. The interface condition was further confirmed by the corresponding high-resolution TEM image, and there is no sight of interface

diffusion or Fe oxidization as shown in Fig 4-2b. The electron diffraction shows that NiO(111) has been grown on FePt(001), which is in accordance with XRD results. From plane-view electron diffraction pattern taken with FePt[001] as zone axis shown in Fig 4-2c, the epitaxial relationship between FePt and NiO is established: $(001)[1\bar{1}0]_{\text{FePt}} // (111)[1\bar{1}0]_{\text{NiO}}$. In the film plane NiO has two epitaxial orientations with the 6-fold $\{110\}$ rotated by 30° (or 90°) against each other.

4.3.3 Further confirmation of in-plane epitaxial relationship

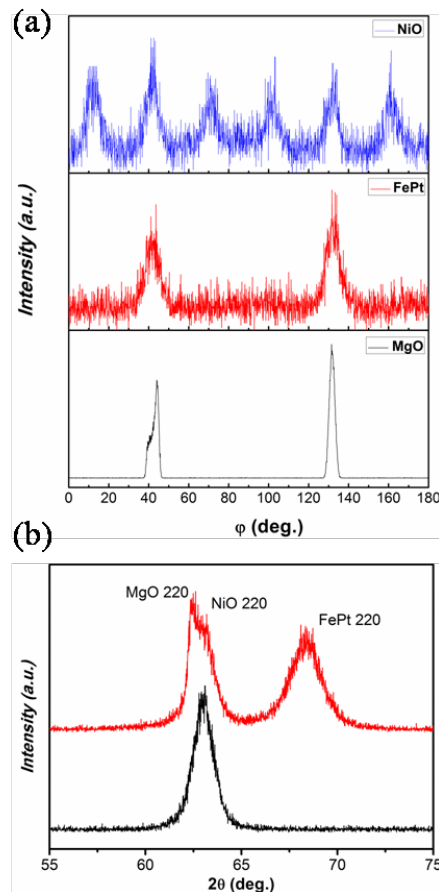


FIG 4-3 (a) XRD 180° ϕ -scan plot for FePt(2.5 nm)/NiO(21 nm) bilayer structure. (b) In-plane grazing incidence XRD profiles of FePt/NiO bilayer structure. The red profile corresponds to the x-ray scattering plane perpendicular to the MgO(220) plane. While the black profile corresponds to the film rotated around to its surface normal by 60° .

To further confirm the in-plane crystallographic orientation of FePt/NiO bilayer structure, the XRD 180° ϕ -scans were performed. The ϕ -scan plots for {113} family of FePt and {113} family of NiO are shown in Fig 4-3a. It is seen that 2 symmetrical peaks from FePt {113} reflections located at same ϕ angle as MgO {113} reflections, suggesting the FePt layer well epitaxially grown on MgO(001) substrate. On the other hand, for NiO layer, it exhibits 6 peaks with an azimuthal interval of 30° , indicating an in-plane 12-fold symmetry. Obviously, this result suggests the same epitaxial relationship as SADP. To provide more evidences on the in-plane epitaxial relationship, the in-plane grazing incidence XRD measurement was also carried out as shown in Fig 4-3b. When the x-ray scattering plane is nearly perpendicular to the MgO(200) plane, the {220} reflections from MgO, FePt and NiO can be all observed. After rotating the film around its surface normal by 60° , only NiO(220) peak can be observed. Since the in-plane twined microstructures of NiO have the same feature, the results from in-plane XRD also prove that the epitaxial relationship determined by SADP is very reliable.

4.4 Discussions on the relationship between the magnetic structure of NiO and epitaxial strain

In epitaxial thin film, the anisotropy of NiO is dominated by magnetoelastic effect resulting from epitaxial strain.^{12,23} While at FePt/NiO interface in our sample, the epitaxial misfits along NiO [112] and $[1\bar{1}0]$ axis obtained from in-plane XRD are -6.7% and +7.5%, respectively. With the consideration of recently reported FePt(001)/CoO(111) structure, such an in-plane anisotropic strain in CoO leads to the out-of-plane $[\bar{1}\bar{1}1]$ stacking direction favorable, consequently forming a fully compensated AFM interface.²⁴ This provides a useful reference for our FePt/NiO

structure. Since the Ni spins are aligned along $\langle 112 \rangle$ directions within $\{111\}$ planes in the bulk,^{25, 26} it is reasonable to expect that the initial AFM spin alignment at FePt(001)/NiO($\bar{1}\bar{1}1$) interface will be in the film plane containing fully compensated spins.

4.5 Magnetic hysteresis loops and initial magnetization curves

Figures 4-4a and 4-4b show the perpendicular hysteresis loops of FePt single layer, FePt/NiO bilayers before and after FC. FC treatment for bilayer structure was performed in a low vacuum (1.33 Pa) with a perpendicular magnetic field of 5 kOe from 530 K (above the Néel temperature 523 K of NiO) to room temperature. Because for Fe/NiO bilayer structure, the XPS spectra do not show a significant change in chemical state of Fe up to a heat treatment temperature of 540 K.²⁷ While during the FePt ordering, the Pt atoms show a tendency of surface segregation,^{28,29} forming a Pt terminated surface. Thus, the magnetic properties of FePt are considered not affected by our FC treatment.²⁴ From perpendicular hysteresis loops, we can observe that all three samples possess strong perpendicular magnetic anisotropy. The resulting hysteresis loop after FC shows an exchange bias field of -41 Oe at 300 K and increases to -301 Oe at 20 K (Fig 4-4b). Figure 4-4c shows the initial in-plane magnetization curves obtained at 300 K. The greatly increased saturation field for the bilayers after FC indicates that the Fe spins become more stable along the film normal direction. In order to clarify the influence of NiO on the perpendicular magnetization process, the perpendicular initial magnetization curves for as grown FePt single layer and FePt/NiO bilayers were measured at 300 K as shown in Fig 4-4d. The non-zero magnetization at starting point is because that a 200 Oe field was applied to center the sample position in SQUID chamber before the measurement. At the first stage, the

magnetization of FePt/NiO bilayers rapidly increases. However, when it is close to saturation, the magnetization becomes harder and finally intersects with the magnetization curve of FePt film. This observation suggests that the deposition of NiO induces a pinning effect to the magnetization of FePt layer in the as grown bilayer structure as it is magnetized close to the saturation.

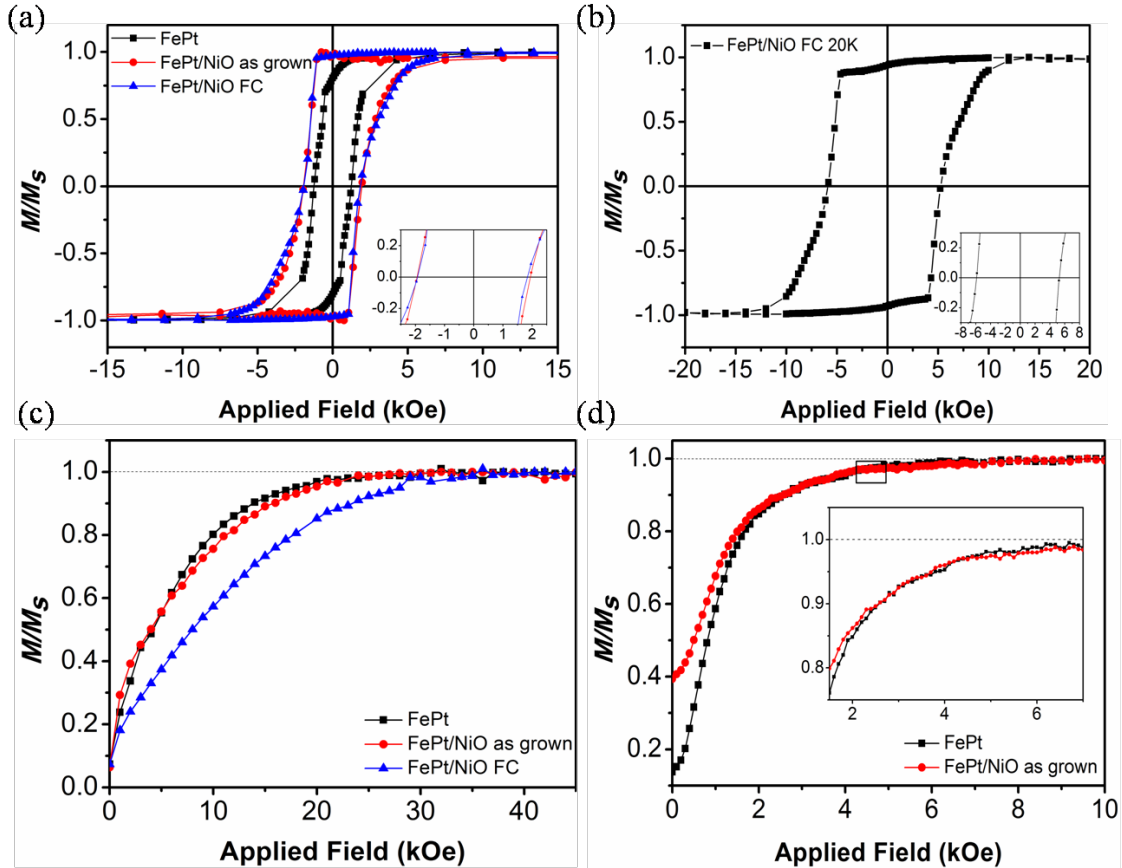


FIG 4-4 Magnetic properties of FePt single layer and FePt/NiO bilayer structures. (a) Perpendicular hysteresis loop measured at 300 K for FePt single layer, and bilayers as grown and after FC. (b) Perpendicular hysteresis loop for bilayers measured at 20 K after FC. The Inset shows the enlarged loop around coercive field for bilayers. (c) Initial magnetization curve at 300 K measured along in-plane direction. (d) Perpendicular initial magnetization curve at 300 K. The inset in panel (d) shows the enlarged curve around cross point.

4.6 Magnetic domain imaging

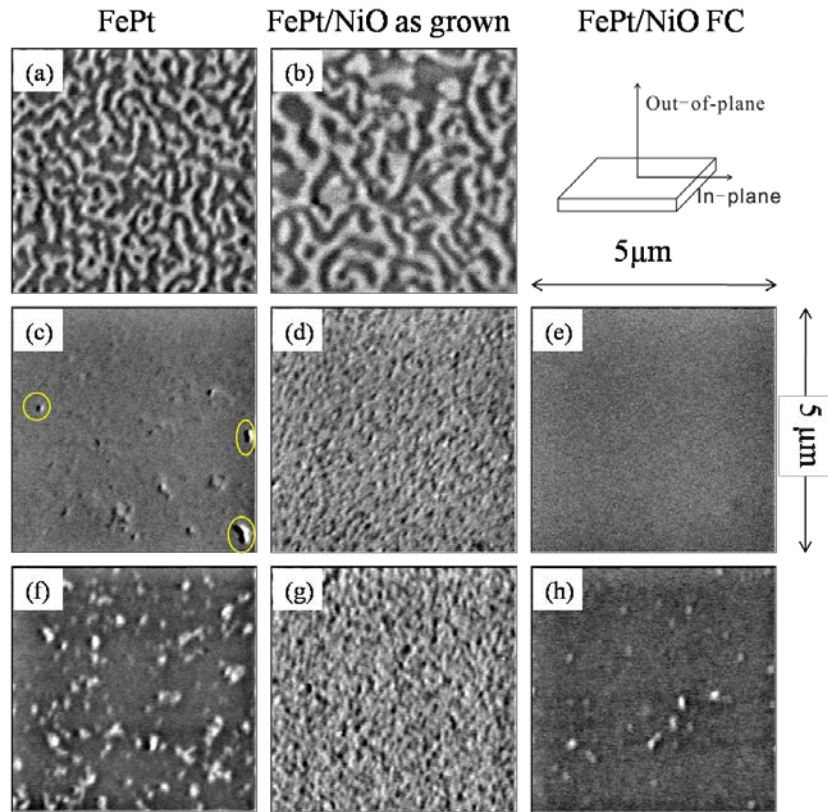


FIG 4-5 Magnetic domain structures in FePt single layer and FePt/NiO bilayers for different remanence. The MFM measurements were performed at 300 K. [(a) and (b)] MFM images of as grown FePt single layer (a) and bilayers (b). [(c) and (d)] MFM images of FePt single layer (c) and bilayers (d) after magnetizing in film normal direction with a field of 5 kOe. (e) MFM image of bilayer structure after perpendicular FC with 5 kOe external magnetic field. [(f)-(h)] A partially demagnetizing field was applied along in-plane direction with a field of 15 kOe to (c)-(e). The corresponding domain images were recorded as (f)-(h).

To further elucidate the impact of NiO on FePt layer, we imaged magnetic domain structures in different remanent states. Figure 4-5 shows MFM images of FePt single layer and FePt/NiO bilayers that were subjected to different field sequences. For as grown structures (see Figs 4-5a and 4-5b), both two samples exhibit stripe domains. The increase of domain width for bilayer structure is due to the induced

anisotropy from FM/AFM coupling, which will be discussed below. After magnetizing along normal direction with 5 kOe applied field, only small unreversed domain can be observed for FePt single layer (see circles in Fig 4-5c). While for bilayers, a faint stray field contrast is visible, indicating the existence of FM magnetization fluctuation slightly off the film normal direction (Fig 4-5d). In the case of bilayer structure after FC, FM layer was saturated and a single domain structure was formed as shown in Fig 4-5e. Subsequently applying a 15 kOe in-plane field to partially demagnetize films, an inhomogeneous nucleation bubble domains in coexistence with irregular stripe domains appears in FePt single layer (Fig 4-5f). However, for bilayers after FC, only bubble domains are observable as shown in Fig 4-5h. Interestingly, for as grown bilayers, the faint stray field contrast is enhanced (Fig 4-5g). From the MFM results presented above, following conclusions can be drawn: (i) During magnetization process, compared with the structure of stripes coexisting with bubble domains, the bubble domain structure is closer to the uniform domain structure (saturation).³⁰⁻³² Therefore, an enhancement of perpendicular magnetic anisotropy for FePt/NiO bilayer structure can be expected after FC. Such enhancement was also reported in orthogonal CoO/Ni coupling structure.³³ (ii) For as grown FePt/NiO bilayer structure, the faint stray field contrast observed in Figs 4-5d and 4-5g reveals that a small angle rotation of magnetization is needed to be further magnetized to saturation. Both these two findings are in good agreement with the results from magnetization curves.

4.7 Proposed interfacial AFM spin of NiO canting mechanism

Here, we turn to discuss the AFM spin configuration at FePt/NiO interface with the consideration of lowest energy coupling configuration proposed from numerical

simulation.^{5,14,16} The idea is that at fully compensated AFM interface, the coupling frustration results in the AFM spins deviate slightly from their easy axis to generate a net magnetic moment. Consequently, the FM spin aligns antiparallel to this induced moment, orienting perpendicular to the AFM easy axis. The resulting configuration is shown in the inset of Fig 4-6. Figure 4-6 shows the out-of-plane canting of AFM spins against adjacent FM spins in different cases. In principle, owing to the large easy plane anisotropy, the Ni spins should be constrained in the (111) plane,³⁴ forming a stable coupling configuration with the FM spin in plane (1). It is known that FC treatment results in the repopulation of AFM magnetic domains,³⁵ and the alignment of AFM spins depends on the local FM order.^{25,36} For as-grown FePt/NiO bilayers, since

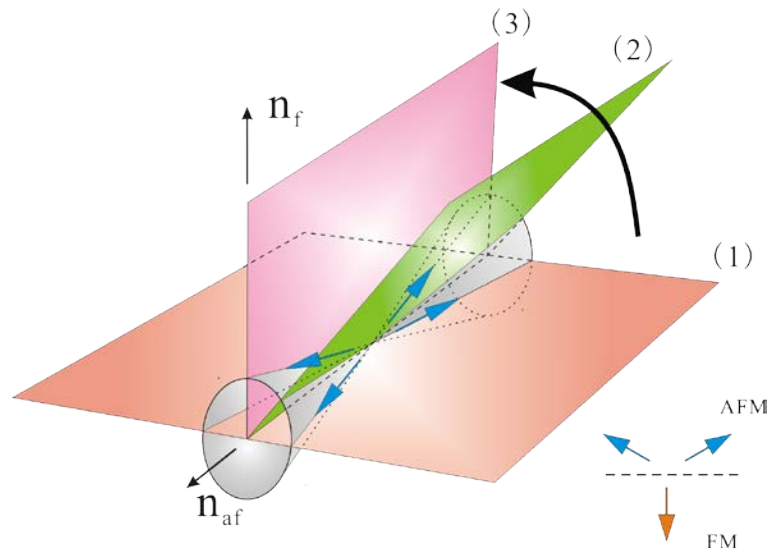


FIG 4-6 Out-of-plane canting of AFM spins response to the adjacent FM spin. Blue arrows represent the AFM spins. Plane 1 and plane 3 represent the FM/AFM interface plane and normal plane, respectively. The inset shows lowest energy coupling configuration, where the deviation of FM/AFM coupling angle from 90° is somewhat exaggerated.

deposition temperature of NiO (500 K) is close to its Néel temperature ($T_N=523$ K), following the deposition of NiO on top of FePt, the competition among strong perpendicular magnetic anisotropy of FePt, FM/AFM coupling and NiO easy plane

anisotropy leads to the out-of-plane canting of Ni spins. Consequently, the Ni spins lie in plane (2). In this configuration, an induced extra uniaxial anisotropy in FePt layer can be expected, which is tilted slightly from the normal direction also in plane (2). As the Fe spins equally align either up or down to the interface during cooling, no unidirectional anisotropy can be obtained. However, for bilayer structure after FC, during FC treatment, the magnetic field is large enough to confine the Fe spins in a certain direction along the film normal as confirmed by MFM measurement (Fig. 4-5e), giving rise to the Ni spins align in the normal plane [plane (3)] to form a lowest energy coupling configuration. It can be easily understood that this type of twist in NiO layer will induce a unidirectional anisotropy in FePt layer as well as an enhancement of perpendicular magnetic anisotropy.

4.8 Calculation of stripe domain width in ultrathin FePt layer

In order to confirm the validity of our proposed mechanism above, the stripe domain width of FePt in as grown FePt single layer and FePt/NiO bilayers (Figs 4-5a and 4-5b) was quantitatively analyzed. The formation of magnetic domain is due to the competing energy of the magnetic exchange interaction, magnetocrystalline anisotropy and magnetic dipolar interaction.³⁷ After NiO deposition, the exchange coupling between NiO and FePt layer can be regarded as an induced uniaxial anisotropy K_{sf} .³³ Assume that both induced K_{sf} and Fe spins are sufficiently close to the film normal direction. This assumption is quite reasonable because of the large perpendicular magnetic anisotropy of FePt layer and high NiO deposition temperature. By using Yafet's model³⁸ and making the same approximation as Y. Z. Wu *et al.*,³⁹ the total energy per unit area can be calculated from magnetic domain structure

$$\varepsilon = \frac{\pi^2 A}{2wL} \cdot \left(\frac{2ta_{//}}{a_{\perp}} \right) - \left(1 - \frac{w}{2L} \right) \cdot (K_u - \Omega_s + K_{sf}) - \frac{2\Omega_L}{\pi L} \ln\left(\frac{6\pi L}{5w}\right) \quad (4.1)$$

where A and K_u stand for the exchange stiffness and uniaxial anisotropy constant of FePt layer, respectively. t (2.5 nm) is the thickness of FePt layer. $a_{//}$ (2.74 Å) and a_{\perp} (3.72 Å) are the FePt in-plane and out-of-plane lattice parameters, respectively. $\Omega_s = 2\pi M_0^2 (2t/a_{\perp}) a_{//}$ is the short range part of dipolar interaction, where M_0 is saturation magnetization of FePt. $\Omega_L = 2\pi M_0^2 (2t/a_{\perp})^2 a_{//}^2$ is the long range part of dipolar interaction. Subsequently, minimizing this energy in relation to the stripe domain width (L) and domain wall width (w), respectively, the L in FePt layer can be written

$$L = \frac{5At(a_{//}/a_{\perp})\pi^2}{6\Omega_L} \cdot \frac{\exp\left\{ \sqrt{\frac{At(a_{//}/a_{\perp})\pi^4}{4\Omega_L^2} (K_u t - \Omega_s + K_{sf}) + 1 + 1} \right\}}{\sqrt{\frac{At(a_{//}/a_{\perp})\pi^4}{4\Omega_L^2} (K_u t - \Omega_s + K_{sf}) + 1 + 1}} \quad (4.2)$$

Taking the value of $M_0 = 1100$ emu/cc, $A = 1 \times 10^6$ erg/cm,²² and adjusted $K_u = 1.4 \times 10^7$ erg/cc, we estimated L of FePt film $L_{FePt} = 0.15$ μm. This value well agree with the experiment value of $L_{FePt} = 0.10-0.17$ μm. Notice that the K_u value used in this calculation is slightly smaller than the experimental value (1.5×10^7 erg/cc) in Ref. 22, which is considered because of the magnetoelastic anisotropy resulting from the epitaxial strain in our ultrathin FePt layer. Introducing the anisotropy energy $K_{sf} = 0.12$ erg/cm² induced by the orthogonal coupling between Fe and NiO,¹³ the stripe domain with L of FePt in FePt/NiO bilayer film was obtained $L_{FePt/NiO} = 0.17$ μm, which is very reasonable compared with the experimental value $L_{FePt/NiO} = 0.15 - 0.22$ μm.

4.9 Summary

In summary, we have studied the magnetic properties of FePt/NiO bilayer structure grown on MgO (001) single crystal substrate. The results have demonstrated that, for as grown bilayer structure, the out-of-plane canting of Ni spins induces an extra uniaxial anisotropy slightly off the film normal direction, giving rise to a small angle magnetization rotation when the magnetization is close to saturation along the film normal direction. After FC, the realignment of Ni spins leads to the formation of lowest energy FM/AFM coupling in normal plane as indicated by theoretical calculation, which induces a unidirectional anisotropy and an enhancement of perpendicular magnetic anisotropy. Furthermore, the calculation results of stripe domain width also support our proposed Ni spin canting mechanism. This finding will shed a particular light on the mechanism of exchange bias, especially, for recent intensively studied orthogonal FM/AFM coupling structures.

References

- ¹J. Nogués and I. Schuller, *J. Magn. Magn. Mater.* **192**, 203(1999).
- ²W. H. Meiklejohn and C. P. Bean, *Phys. Rev.* **102**, 1413, (1956).
- ³W. H. Meiklejohn. *J. Appl. Phys.* **33**. 1328 (1962)
- ⁴D. Mauri, H. C. Siegmann, P. S. Bagus, and E. Kay, *J. Appl. Phys.* **62**, 3047 (1987).
- ⁵R. L. Stamp, *J. Phys. D* **33**, R247 (2000).
- ⁶E. Jiménez, J. Camarero, J. Sort, J. Nogués, N. Mikuszeit, J. M. García-Martín, A Hoffmann, B. Dieny, and R. Miranda, *Phys. Rev. B* **80**,014415 (2009).
- ⁷J. Camarero, Y. Pennec, J. Vogel, S.Pizzini. M. Cartier, F. Fettar. F. Ernult. A. Tagliaferri, N. B. Brookes, and B. Dieny, *Phys. Rev. B* **65**, 140408(R) (2002).
- ⁸P. Kappenberger, S. Martin, Y. Pellmont, H. J. Hug, J. B. Kortright, O. Hellwig, and Eric E. Fullerton, *Phys. Rev. Lett.* **91**, 267202 (2003).
- ⁹R. Morales, Ali C. Basaran, J. E. Villegas, D. Navas, N. Soriano, B. Mora, C. Redondo, X. Batlle, and Ivan K. Schuller, *Phys. Rev. Lett.* **114**, 097202 (2015).
- ¹⁰J. Wu, J. S. Park, W. Kim, E. Arenholz, M. Liberati, A. Scholl, Y. Z. Wu, Chanyong Hwang, and Z. Q. Qiu, *Phys. Rev. Lett.* **104**, 217204 (2010).
- ¹¹Q. Li, G. Chen, T. P. Ma, J. Zhu, A. T. N'Diaye, L. Sun, T. Gu, Y. Huo, J. H. Liang, R. W. Li, C. Won, H. F. Ding, Z. Q. Qiu, and Y. Z. Wu, *Phys.Rev. B* **91**, 134428 (2015).
- ¹²Wondong Kim, E. Jin, J. Wu, J. Park, E. Arenholz, A. Scholl, Chanyong Hwang, and Z. Q. Qiu, *Phys. Rev. B* **81**, 174416 (2010).
- ¹³J. Li, M. Przybylski, F. Yildiz, X. L. Fu, and Y. Z. Wu, *Phys. Rev. B* **83**, 094436 (2011).
- ¹⁴N. C. Koon, *Phys. Rev. Lett.* **78**, 4865 (1997).

- ¹⁵J. Li, A. Tan, S. Ma, R. F. Yang, E. Arenholz, C. Hwang, and Z. Q. Qiu, *Phys. Rev. Lett.* **113**, 147207 (2014).
- ¹⁶M. D. Stiles and R. D. McMichael, *Phys. Rev. B* **59**, 3722 (1999).
- ¹⁷S. Mangin, D. Ravelosona, J. A. Katine, M. J. Carey, B. D. Terris, and E. E. Fullerton, *Nat. Mater.* **5**, 210 (2006).
- ¹⁸S. Ikeda, K. Miura, H. Yamamoto, K. Mizunuma, H. D. Gan, M. Endo, S. Kanai, J. Hayakawa, F. Matsukaru, and H. Ohno, *Nat. Mater.* **9**, 721 (2010).
- ¹⁹Y. Shiratsuchi, H. Noutomi, H. Oikawa, T. Nakamura, M. Suzuki, T. Fujita, K. Arakawa, Y. Takechi, H. Mori, T. Kinoshita, M. Yamamoto, and R. Nakatani, *Phys. Rev. Lett.* **109**, 077202 (2012).
- ²⁰I. Schmid, M. A. Marioni, P. Kappenberger, S. Romer, M. Parlinska-Wojitan, H. J. Hug, O. Hellwig, M. J. Carey, and E. E. Fullerton, *Phys. Rev. Lett.* **105**, 197201 (2010).
- ²¹Y. K. Takahashi, K. Hono, T. Shima, and K. Takanashi, *J. Magn. Magn. Mater.* **267**, 248(2003).
- ²²S. Okamoto, N. Kikuchi, O. Kitakami, T. Miyazaki, Y. Shimada, and K. Fukamichi. *Phys. Rev. B* **66**, 024413 (2002).
- ²³I. P. Krug, F. U. Hillebrecht, M. W. Haverkort, A. Tanaka, L. H. Tjeng, H. Gomonay, A. Fraile-Rodríguez, F. Nolting, S. Cramm, and C. M. Schneider. *Phys. Rev. B* **78**, 064427 (2008).
- ²⁴Anne D. Lamirand, Márcio M. Soares, Aline Y. Ramos, Hélio C. N. Tolentino, Maurizio De Santis, Julio C. Cezar, Abner de Siervo, and Matthieu Jamet. *Phys. Rev. B* **88**, 140401(R) (2013).
- ²⁵H. Ohldag, A. Scholl, F. Nolting, S. Anders, F. U. Hillebrecht, and J. Stöhr. *Phys. Rev. Lett.* **86**, 2878 (2001).

- ²⁶D. Alders, L. H. Tjeng, F. C. Voogt, T. Hibma, G. A. Sawatzky, C. T. Chen, J. Vogel, M. Sacchi, and S. Iacobucci, *Phys. Rev. B* **57**, 11623 (1998).
- ²⁷P. Luches, S. Benedetti, A. di Bona, and S. Valeri, *Phys. Rev. B* **81**, 054431 (2010).
- ²⁸Michael Müller and Karsten Albe, *Phys. Rev. B* **72**, 094203 (2005).
- ²⁹Luyang Han, Ulf Wiedwald, Balati Kuerbanjiang and Paul Ziemann, *Nanotechnology* **20**, 285706 (2009).
- ³⁰J. Wu, J. Choi, C. Won, Y. Z. Wu, A. Scholl, A. Doran, Chanyong Hwang, and Z. Q. Qiu, *Phys. Rev. B* **79**, 014429 (2009).
- ³¹N. Saratz, A. Lichtenberger, O. Portmann, U. Ramsperger, A. Vindigni, and D. Pescia, *Phys. Rev. Lett.* **104**, 077203 (2010).
- ³²Juyoung Jeong, Ilkyu Yang, Jinho Yang, Oscar E. Ayala-Valenzuela, Dirk Wulferding, J.-S. Zhou, John B. Goodenough, Alex de Lozanne, J. F. Mitchell, Neliza Leon, Roman Movshovich, Yoon Hee Jeong, Han Woong Yeom, and Jeehoon Kim, *Phys. Rev. B* **92**, 054426 (2015).
- ³³P. Kuświk, P. L. Gastelois, M. M. Soares, H. C. N. Tolentino, M. De Santis, A. Y. Ramos, A. D. Lamirand, M. Przybylski, and J. Kirschner, *Phys. Rev. B* **91**, 134413 (2015).
- ³⁴M. T. Hutchings, *Phys. Rev. B* **6**, 3447 (1972).
- ³⁵W. Zhu, L. Seve, R. Sears, B. Sinkovic, and S. S. P. Parkin, *Phys. Rev. Lett.* **86**, 5389 (2001).
- ³⁶N. J. Gökemeijer, J. W. Cai, and C. L. Chien, *Phys. Rev. B* **60**, 3033 (1999).
- ³⁷Charles Kittel. *Phys. Rev.* **70**, 965 (1946).
- ³⁸Y. Yafet and E. M. Gyorgy, *Phys. Rev. B* **38**, 9145 (1988).
- ³⁹Y. Z. Wu, C. Won, A. Scholl, A. Doran, H. W. Zhao, X. F. Jin, and Z. Q. Qiu, *Phys. Rev. Lett.* **93**, 117205 (2004).

Chapter 5 Field cooling driven magnetic anisotropy and stripe domain evolution in FePt/NiO/FePt trilayer structure

5.1 Introduction

Exchange bias effect originated from interfacial coupling between ferromagnetic (FM) and antiferromagnetic (AFM) layers has received considerable attention in the last five decades because of its application in magnetic devices.¹ Although several models were developed to explain this effect,²⁻⁶ the complexity of FM/AFM interface in real system renders it difficult to present a general theory for FM/AFM interfacial interaction. Recently, it was experimentally proven that the FM and AFM spins can be coupled orthogonally at compensated AFM interface, for instance, Fe/NiO(001)^{7,8} or Fe/Co(001)^{9,10} coupling structures. However, due to the absence of unidirectional anisotropy, the mechanism of exchange bias in such coupling structures remains a mystery. Thus, in order to address this issue, a detailed study on FM/AFM coupling configuration at compensated AFM interface is highly required.

Realizing that at FM/AFM interface the AFM order can induce various types of magnetic anisotropy,¹¹ or even change the perpendicular magnetic anisotropy in adjacent FM layer,¹² An alternative approach to investigate the FM/AFM coupling configuration is to study how the FM layer responds to the change of AFM order in AFM layer. It was found recently that in Py/FeMn/Ni trilayers,¹³ the in-plane Ni enhances the Py fourfold anisotropy. The authors speculated that the reason for this enhancement is a slight increase of FeMn spin in-plane component caused by direct coupling between Ni and FeMn spins. This result indicates that in such trilayer structure the low anisotropy of FM layer makes it very sensitive to the modification of

AFM spin structure, which may offer an opportunity to make a detailed indirect observation on the FM/AFM coupling configuration. On the other hand, the study of interlayer exchange coupling (IEC) of two FM layers across a non-FM insulating spacer layer has been stimulated since the discovery of tunneling magnetoresistance.¹⁴ Among insulating spacer based structures, it possesses particular interest for the case of FM layers separated by a antiferromagnetic insulating spacer due to its unexpected behavior.¹⁵ For NiO spacer, the occurrence of a 90° in-plane IEC has been observed in Fe₃O₄/NiO/Fe₃O₄,¹⁶ Ni₈₀Fe₂₀/NiO/Co,¹⁷ and Co/NiO/Fe structures.¹⁸ This anomalous interlayer coupling was explained by contradictory mechanisms, either the formation of 90° spiraling spin structure in AFM spacer going from one FM/AFM interface to the other,¹⁶ or the collinear and orthogonal FM/AFM coupling separately presented at two FM/AFM interface¹⁷ resulting from the interface roughness. The focus of all works mentioned was to puzzle out the 90° IEC mechanisms. Moreover, it is well accepted that field cooling (FC) could lead to the repopulation of AFM magnetic domains,¹⁹ and realign the AFM spins depending on the local FM order.^{20,21} Recalling the various results and points of view in this paragraph, it is interesting to propose a trilayer structure, in which regardless of NiO spacer, the interlayer coupling between two FM layers is “naturally” constructed as a 90° coupling. Through a certain FC treatment to realign the AFM spins in NiO layer, it may raise an issue, i.e., whether the modification of AFM spin structure can influence the magnetic behavior of adjacent FM layers.

In this chapter, we present an investigation on FePt/NiO/FePt trilayer structure, in which the bottom and top FePt layer is partially ordered and disordered, respectively. The fascinating feature of this structure is that the strong perpendicular magnetic anisotropy in bottom layer and magnetic dipolar anisotropy in top layer give

rise to a 90° interlayer coupling between two FM layers, while the in-plane magnetic anisotropy of disordered FePt layer can be hardly influenced by the ordered one. Through an in-plane FC with 500 Oe external fields to realign the Ni spins, we find that in-plane magnetic anisotropy in disordered upper FePt layer and the stripe magnetic domain structure in ordered bottom FePt layer were significantly changed. Based on our experimental results, the interfacial FM/AFM coupling configuration has been carefully discussed.

5.2 Details on FePt/NiO/FePt trilayer structure preparation

Reference FePt_{Oop}(4.5 nm)/NiO(4 nm) bilayers (S1) and FePt_{Oop}(4.5 nm)/NiO(t nm)/FePt_{tp}(3.5 nm) trilayers were sputtered on single crystal MgO(001) substrate. The preparation conditions for bilayers has been described in chapter 4, and the only difference is that in order to trigger the L1₀ phase transformation (perpendicular magnetic anisotropy) for relatively thicker FePt layer, an elevated 723 K substrate temperature was used. For trilayer structure, a FePt(3.5 nm) layer was subsequently deposited on top of bilayers at 373 K. With this substrate temperature the top FePt layer remains disordered and the Fe magnetization of FePt layer is in the film plane. The thicknesses of NiO layer were chosen as 2 (S2) and 4 nm (S3). Finally, the trilayer samples were capped by 2 nm of NiO sputtered at RT. An additional sample of FePt_{tp}(3.5 nm)/NiO(4 nm)/FePt_{tp}(3.5 nm) (S4) was also prepared. In this trilayer structure, the two FePt layers were grown in the same condition as the top disordered FePt layer in samples of S2 and S3. Besides that, the other preparation conditions were as same as samples of S2 and S3. The FePt/NiO/FePt trilayer structures grown on MgO(001) single crystal substrate give rise to an extraordinary epitaxial relationship. The structure of the sample was characterized by X-ray diffraction

(XRD). To understand the influence of FM/AFM coupling configuration on two FM layers, the samples were cooled through Néel temperature ($T_N \sim 523$ K) in a low vacuum (1.33 Pa) by using two different FC treatments: i. In-plane FC with 500 Oe external fields along MgO [100] axis to saturate the disordered FePt layer; ii. Out-of-plane FC in 8 kOe fields along film normal direction to align the magnetization of ordered FePt layer in normal direction. The average magnetic properties were measured by vibrating sample magnetometer (VSM) at RT and the flexible sample holder allows the measurements conducted along different in-plane directions. The room temperature domain imaging was performed by magnetic force microscopy (MFM).

5.3 Structural characterization

5.3.1 X-ray diffraction profiles

It is well known that at NiO interface the FM/AFM coupling configuration is dominated by magnetoelastic effect resulting from epitaxial strain.^{7,22} This strain is mainly related to the epitaxial relationship. At first, the structure of different samples was characterized. The XRD patterns for samples of S1, S3 and S4 are shown in Fig 5-1. The unlabeled peaks are from MgO(001) single crystal substrate. For FePt_{Oop}/NiO bilayers, apart from the NiO and MgO reflections from NiO spacer and substrate, only FePt(001) and FePt(002) peaks are observable, suggesting a strong FePt(001) texture. The appearance of FePt(001) superlattice peak indicates the ordering of FePt layer and the degree of order calculated from XRD pattern is 0.52. Correspondingly, the FePt(001) and FePt(002) peaks observed in FePt_{Oop}/NiO/FePt_{ip} trilayers are from bottom partially ordered FePt layer. Note that the ordered and (001)

textured FePt film possesses a strong perpendicular magnetic anisotropy, leading to the magnetization of bottom FePt layer along film normal direction. In the case of

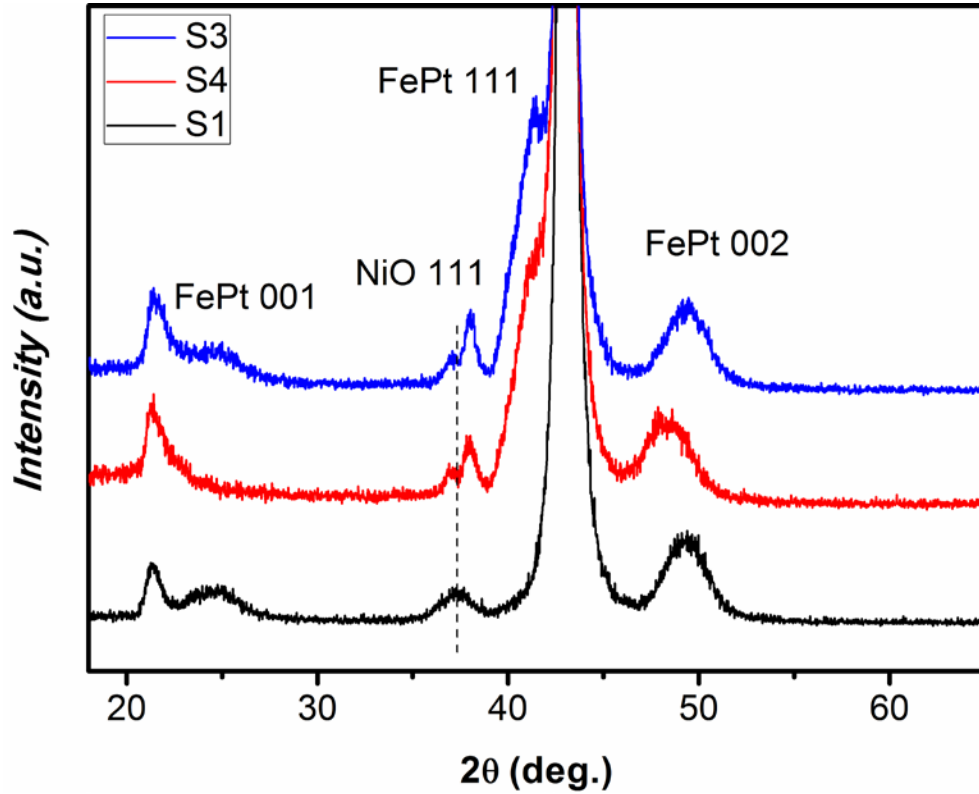


FIG 5-1 (a) The XRD θ - 2θ scans of FePt_{Oop}(4.5 nm)/NiO(4 nm) bilayers (S1) (black pattern), FePt_{Oop}(4.5 nm)/NiO(4 nm)/FePt_{I_p}(3.5 nm) trilayers (S3) (blue pattern), and FePt_{I_p}(3.5 nm)/NiO(4 nm)/FePt_{I_p}(3.5 nm) (S4) (red pattern).

FePt_{I_p}/NiO/FePt_{I_p} trilayers, the absence of (001) and relatively low angle (002) FePt peak means that the bottom FePt layer remains disordered. As mentioned above the structural properties of NiO plays a crucial role to determine the interfacial FM/AFM coupling configuration. Thus, it is important to realize the structure of NiO spacer. Compared with bilayers, it is surprising that for both trilayers there exists split NiO peak at NiO (111) 2θ position, which should be originated from lower sandwiched and upper protective NiO layer. Taking the FePt/NiO bilayers as a reference, the low angle (111) peak corresponds to the sandwiched NiO layer. The nearly same 2θ position indicates the sandwiched NiO layer experiences almost same strain as that in

bilayers, and this strain as given from our proceeding chapter will be an in-plane anisotropic strain. On the other hand, an out-of-plane compressive strain could result in the XRD peak shift to high angle site. The peak shift in NiO protective layer is considered caused by a compression along film normal direction. Since the natural exchange striction leads to a compression along $\langle 111 \rangle$ direction,²³ the NiO protective layer should favor a [111] stacking direction. Consequently, the NiO easy plane will be coplanar with the (111) interface, possessing a fairly low in-plane anisotropy.²² In consideration of low in-plane anisotropy and free upper surface, the influence of protective NiO layer on adjacent FePt layer should be negligible small. Moreover, besides all the peaks discussed above, an additional FePt(111) peak can also be observed in both trilayers. It seems that other than bottom FePt layer, the upper FePt follows the same epitaxial relationship as sandwiched NiO spacer.

5.3.2 X-ray diffraction 180° ϕ -scan plots

To understand the in-plane orientations of two FePt layers in FePt_{Oop}/NiO/FePt_{Ip} trilayer structure, the XRD 180° ϕ -scans were carried out. The ϕ -scan plots for {113} family of FePt_{Oop} and {113} family of FePt_{Ip} are shown in Fig 5-2. It is seen that 2 symmetrical peaks from FePt_{Oop} {113} reflections located at same ϕ angle as MgO {113} reflections, suggesting the bottom FePt layer well epitaxially grown on MgO(001) substrate. Due to the weak signal from NiO layer, the in-plane orientations of NiO could not be obtained by ϕ scans. However, from our pervious study for FePt/NiO bilayers,²⁴ it has shown that the NiO($\bar{1}\bar{1}1$) layer exhibits a 12-fold symmetry along the film normal axis and the epitaxial relationship between FePt and NiO is established: FePt(001) // NiO($\bar{1}\bar{1}1$); FePt[1 $\bar{1}0$] // NiO[1 $\bar{1}0$]. For such epitaxial relationship, an in-plane anisotropic strain will be induced, giving rise to a [$\bar{1}\bar{1}1$] NiO

stacking direction. As a consequence, the Fe and Ni spins should be orthogonally coupled. Shown in the top panel of Fig 5-2, for disordered FePt layer, it exhibits 6 peaks with an azimuthal interval of 30° , indicating an in-plane 12-fold symmetry. These results show that the upper FePt layer follows the same epitaxial relationship as NiO spacer. Finally, the entire epitaxial relationship in FePt_{Oop}/NiO/FePt_{Ip} trilayer structure is established as follows: MgO(001) // FePt_{Oop}(001) // NiO($\bar{1}\bar{1}1$) // FePt_{Ip}($\bar{1}\bar{1}1$); MgO[1 $\bar{1}0$] // FePt_{Oop}[1 $\bar{1}0$] // NiO[1 $\bar{1}0$] // FePt_{Ip}[1 $\bar{1}0$].

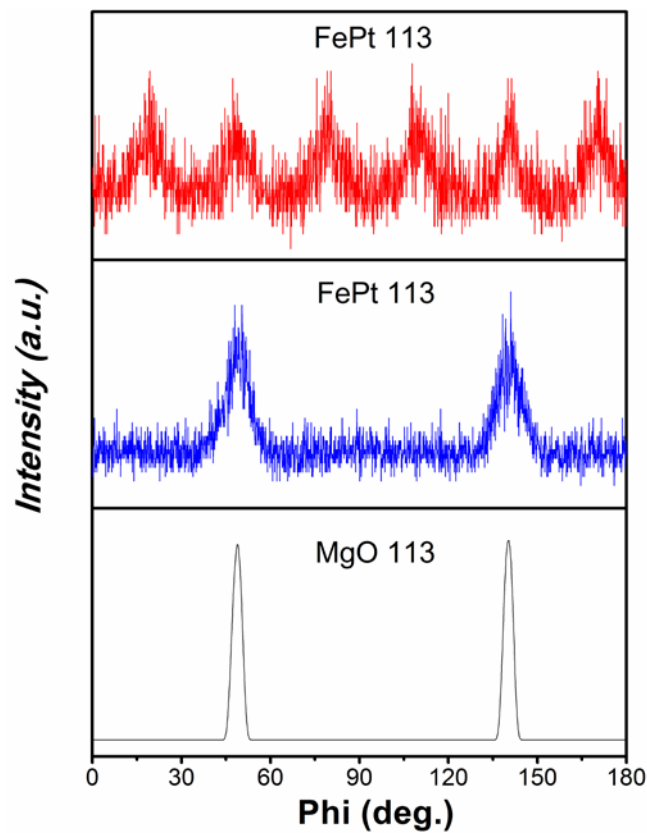


FIG 5-2 XRD 180° ϕ -scan plots for FePt_{Oop}(4.5 nm)/NiO(4 nm)/FePt_{Ip}(3.5 nm) (S3) trilayer structure.

5.4 Magnetic hysteresis loops

5.4.1 Out-of-plane Magnetic hysteresis loops

Figure 5-3 shows the hysteresis loops taken at RT for samples of S1, S3, and S4, and the magnetic fields were applied perpendicular to the film surface. It is seen that the FePt_{Oop}/NiO bilayers exhibit a sharp square loop with 1.46 kOe coercive field as

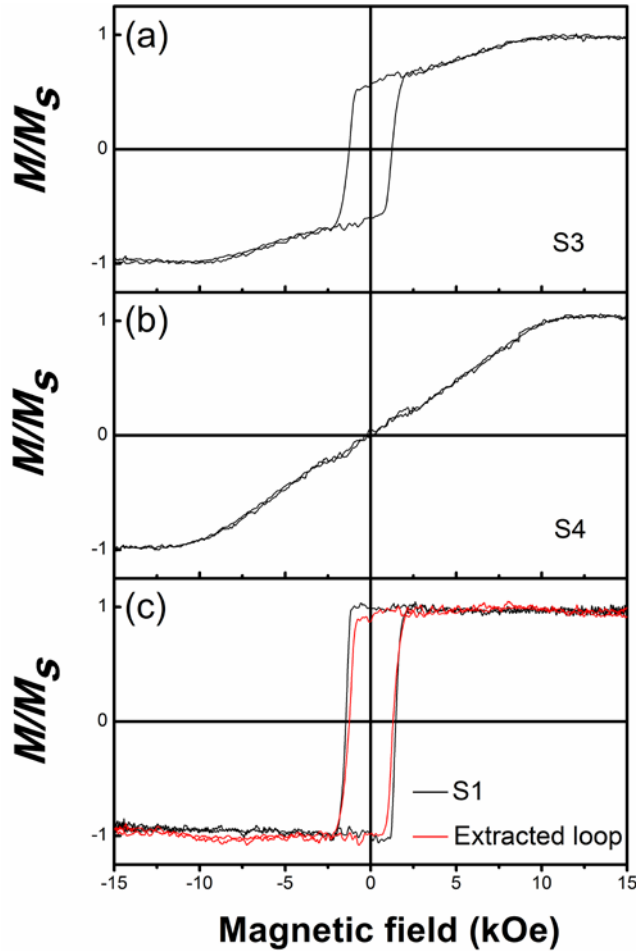


FIG 5-3 Hysteresis loops along film normal direction for (a) FePt_{Oop}(4.5 nm)/NiO(4 nm)/FePt_{Ip}(3.5 nm) (S3), and (b) FePt_{Ip}(3.5 nm)/NiO(4 nm)/FePt_{Ip}(3.5 nm) (S4) trilayers. (c) Perpendicular hysteresis loop of extracted FePt bottom layer (red loop) and that of FePt_{Oop}(4.5 nm)/NiO(4 nm) bilayers (S1) (black loop). The extracted loop was obtained from samples of S3 and S4, through the following relationship: $M_{bottom} = M_{S3} - M_{S4}/2$.

shown in Fig 5-3c (black loop), while for FePt_{ip}/NiO/FePt_{ip} trilayers, along the same direction a remanent magnetization of almost 0% is observed in Fig 5-3b. The strong perpendicular magnetic anisotropy in ordered FePt and magnetic dipolar anisotropy in disordered FePt support that in FePt_{oop}/NiO/FePt_{ip} trilayer structure, owing to the “force of nature”, the magnetization of bottom and upper FePt layer will be restrained along film normal and in-plane direction, respectively. Assuming no direct coupling between two FePt layers, through subtracting the contribution of disordered FePt layer (data of Fig 5-3b), the perpendicular hysteresis loop for bottom FePt layer was extracted from Fig 5-3a as shown in Fig 5-3c (red loop). Compared with the loop of FePt_{oop}/NiO bilayers, the similar square shape for extracted loop confirms that the two FM layers in FePt_{oop}/NiO/FePt_{ip} trilayer structure exhibit a 90° interlayer coupling. On account of the differences, a slight decrease of coercive field can be observed in extracted loop, which is considered resulting from the FM layer coupling mediated by NiO spacer and mainly related to the interfacial FM/AFM coupling configuration.

5.4.2 In-plane magnetic hysteresis loops for FePt_{ip}/NiO/FePt_{ip} structure

After the verification of 90° interlayer coupling in FePt_{oop}/NiO/FePt_{ip} trilayers, the influence of AFM spin alignment of NiO within the (111) easy plane on the in-plane anisotropy of disordered FePt has been subsequently studied. Figure 5-4a shows the in-plane hysteresis loops of FePt_{ip}/NiO/FePt_{ip} trilayers. The magnetic field was applied along MgO [100] and [010] axis, respectively. Worth mentioning that the fcc CoPt possesses a cubic magnetocrystalline anisotropy with easy axis along <111> directions and its value²⁵ is $K_{mc} \sim 6 \times 10^5 \text{ erg/cm}^3$, a similar value is expected in the case of disordered FePt.²⁶ The typical square easy axis loops with nearly same

remnant magnetization are observed in two orthogonal measuring directions, indicating that both bottom FePt(001) and upper FePt($\bar{1}\bar{1}1$) layer possess magnetic isotropy along these two directions. It is well accepted that the FC treatment could modify the AFM spin structure.¹⁹ The experimental evidence shows that, for Fe/Co/MgO(001) bilayers, in-plane uniaxial magnetic anisotropy in Fe layer can be induced by FC treatment.^{10,27} However, due to the low NiO anisotropy in ($\bar{1}\bar{1}1$) plane,^{22,28} there is no significant change on hysteresis loop after in-plane FC along MgO [100] axis, especially for the remanent magnetization as shown in Fig 5-4b. The almost 100% remanent magnetization in both hysteresis loops strongly suggest that at

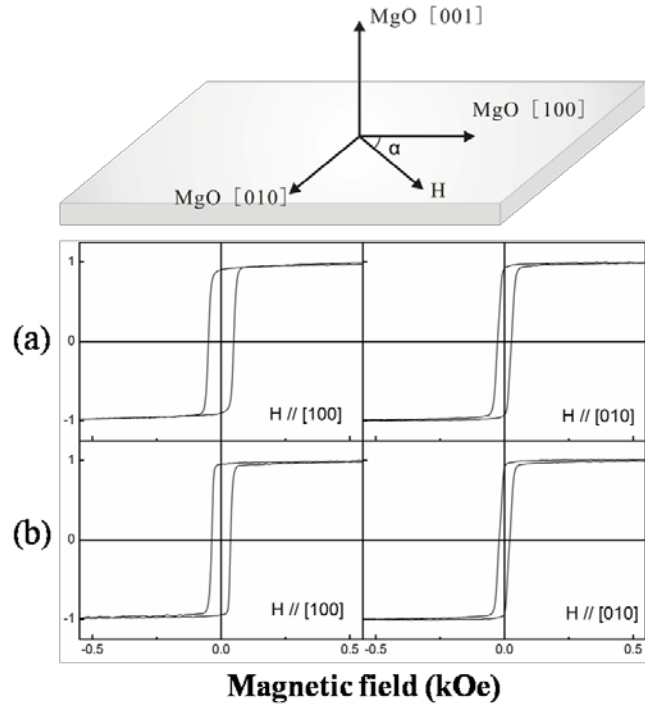


FIG 5-4 In-plane hysteresis loops of FePt_{IP}(3.5 nm)/NiO(4 nm)/FePt_{IP}(3.5 nm) (S4) trilayers (a) before, and (b) after in-plane FC. The FC was performed along MgO [100] axis and measurements were conducted with the field along bottom FePt layer [100] and [010] axis, respectively. The inset shows the measurement geometry, in which the angle α denotes the angle between magnetic field and MgO [100] axis in the film plane.

two FePt/NiO interfaces, the FM/AFM coupling should be the same type, i.e., either collinear or perpendicular coupling. Since the layer thickness of NiO layer is thinner than 6 nm, no exchange bias exists in this work.²⁹ Besides, among hysteresis loops in Fig 5-4a the slight differences of coercive field may also be concerned. Generally, in FM/AFM bilayers the enhancement of coercive field can be understood originated from coupling at FM/AFM interface with rotatable AFM spins.³⁰ The winding and unwinding of the AFM NiO domain walls⁸ during the FePt magnetic switching process may account for these differences, whose analysis is beyond the scope of this work.

5.4.3 In-plane magnetic hysteresis loops for FePt_{Oop}/NiO/FePt_{Ip} structure

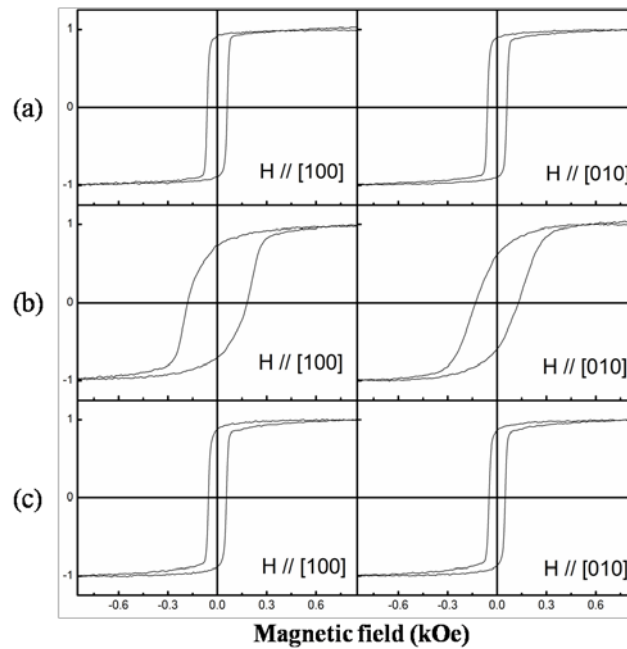


FIG 5-5 In-plane hysteresis loops of upper disorder FePt layer in FePt_{Oop}(4.5 nm)/NiO(4 nm)/FePt_{Ip}(3.5 nm) (S3) trilayers (a) before, (b) after in-plane FC along MgO [100] axis, and (c) subsequent out-of-plane FC along MgO [001] axis. The measurements were conducted with the field along bottom FePt layer [100] and [010] axis, respectively. In this small magnetic field range, due to the large perpendicular magnetic anisotropy, the magnetization contribution from bottom ordered FePt layer is negligible.

To investigate the influence of NiO spacer on magnetic behavior of FePt layer in FM/AFM/FM trilayers, a particular case is a “naturally” 90° interlayer coupling structure as mentioned above. In FePt_{Oop}/NiO/FePt_{Ip} trilayers, to distinguish the magnetization of bottom and upper FePt layer from the hysteresis loop measurement, a relatively small magnetic field of 850 Oe was applied to saturate the upper disordered FePt layer, whereas the magnetization contribution from bottom ordered FePt layer is fairly small because of the strong perpendicular magnetic anisotropy. By using this approach, the in-plane hysteresis loops of upper FePt layer can be obtained as shown in Fig 5-5. For as grown trilayers, along both in-plane directions of measurement, the hysteresis loops exhibit a remanent magnetization of almost 100% with same coercive field in Fig 5-5a. After FC with the external field along MgO [100] axis, it is surprising that a different hysteresis behavior appears which is not observed in the case of FePt_{Ip}/NiO/FePt_{Ip} trilayers. For magnetic field along the direction of the field during FC, the remanent magnetization is reduced to 72% with enlarged coercive field of 182 Oe, while for its orthogonal direction, an even smaller remanent magnetization of 60% and a reduced coercive field of 130 Oe are observed as shown in Fig 5-5b. These results show clearly that the modification of AFM spin structure through in-plane FC induces in-plane magnetic anisotropy in disordered FePt layer. By subsequently performing an out-of-plane FC, the hysteresis loops for both two directions recover to square easy axis loop as shown in Fig 5-5c, which are same as the loops of as grown upper FePt layer. Since the FM/AFM interfacial conditions including roughness and defects determine the types of interfacial coupling,^{31,32} the recovery of hysteresis loops after out-of-plane FC indicates that the heat treatment during FC will not give a significant consequence on the FM/AFM interface, namely, not affect the type of FM/AFM interfacial coupling. To clarify the mechanism of

induced in-plane anisotropy in Fig 5-5b, the FM/AFM interfacial coupling configuration must be realized. Taking the case of FePt_{Ip}/NiO/FePt_{Ip} trilayers as a reference, in FePt_{Op}/NiO/FePt_{Ip} trilayers, the FM/AFM coupling should exhibit the same type at two FM/AFM interfaces. As discussed in chapter 4, the in-plane anisotropic strain in NiO leads to the out-of-plane $[\bar{1}\bar{1}1]$ stacking direction favorable, forming a compensated AFM interface. As a consequence, an orthogonal coupling configuration can be expected at FM/AFM interface. However, in such coupling configuration, the perpendicular Fe in bottom FePt layer has no effect on in-plane anisotropy of upper FePt layer. This is understood that the bottom FePt layer cannot provide extra pinning for the in-plane rotation of Ni spins. Thus, similar results should be expected as Fig 5-5b. Obviously, a new FM/AFM coupling configuration should be proposed to explain the induced in-plane anisotropy of upper FePt layer in FePt_{Op}/NiO/FePt_{Ip} trilayers.

5.5 Discussions on interfacial FM/AFM coupling configuration

As given from chapter 4, we have shown experimental evidence that at compensated AFM interface for spin flop coupling configuration the angle between FM and AFM spins may be not exact 90°. In fact, such spin flop has already been predicted from theoretical calculation. A more detailed description is that at fully compensated AFM interface, the coupling frustration results in the AFM spins deviate slightly from its easy axis to generate a net magnetic moment. Consequently, the FM spin aligns antiparallel to this induced moment, orienting perpendicular to AFM easy axis as shown in the inset of Fig 5-6a.⁴⁻⁶ For FePt_{Op}/NiO bilayers, due to this spin flop coupling, the perpendicular Fe magnetization leads to a slightly slanted Ni spins at the interface off the $(\bar{1}\bar{1}1)$ easy plane as shown in Fig 5-6a (dashed green arrows).²⁴

Correspondingly, the Fe magnetization will also deviate slightly from the film normal direction. Following the idea of FM and AFM spin alignment in spin flop coupling as

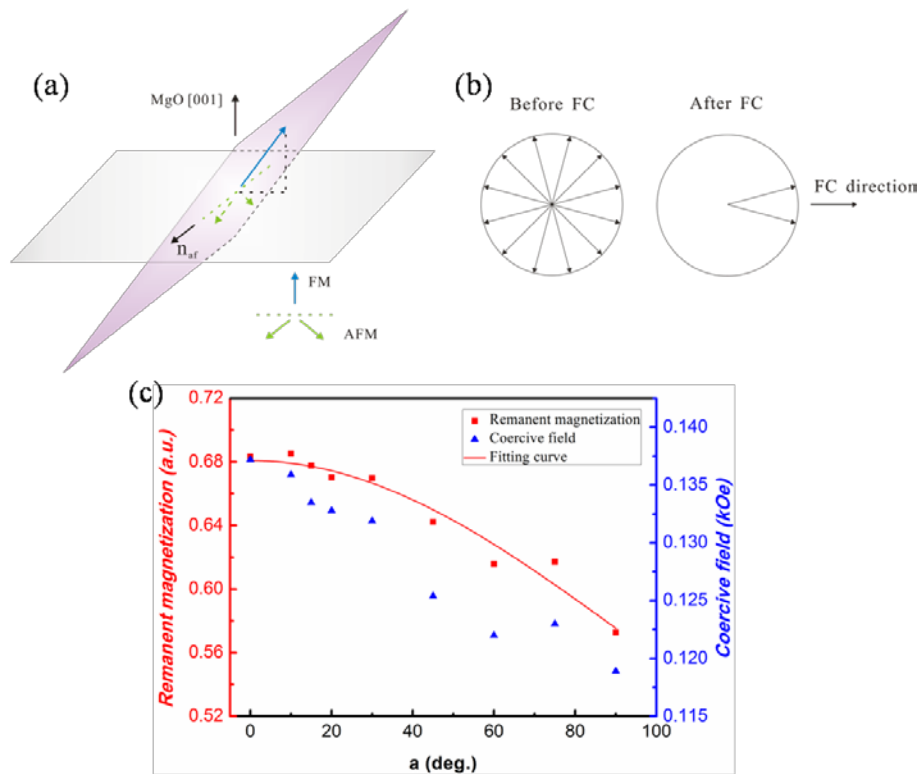


FIG 5-6 (a) Schematic drawing of spins canting in FePt_{Oop}(001)/NiO($\bar{1}\bar{1}1$) bilayers, the blue arrow and dashed green arrow present the FM and AFM spin, respectively. The inset shows spin flop coupling configuration, where the deviation of FM/AFM coupling angle from 90° is somewhat exaggerated. (b) The proposed in-plane projection of net magnetic moment generated from AFM spins before and after in-plane FC. (c) The remanent magnetization (square symbol) and coercive field (triangle symbol) versus measuring angle α for upper disordered FePt layer in FePt_{Oop}(4.5 nm)/NiO(2 nm)/FePt_{Ip}(3.5 nm) (S2) trilayers. And α denotes the angle between measurement direction and in-plane FC MgO [100] direction.

given above, this FM/AFM coupling geometry will provide an extra pinning effect on the rotation of AFM spins in the film plane. For FePt_{Oop}/NiO/FePt_{Ip} trilayers, it is reasonable to assume the same FM/AFM coupling configuration as FePt_{Oop}/NiO

bilayers. In this case, the in-plane FC can enhance the coupling at NiO/FePt_{ip} interface by canting the AFM spins closer to the $(\bar{1}\bar{1}1)$ NiO plane. This will induce effectively stronger in-plane anisotropy in disorder upper FePt layer because of the pinning provided by the out-of-plane aligned Fe spins in bottom FePt layer, which cannot be expected by exact 90° FM/AFM coupling configuration.

To further account for the FC induced in-plane anisotropy in upper FePt layer, we investigated the angular dependence of remanent magnetization of upper FePt layer. Here, the angle refers to the angle between direction of the field during the in-plane FC and measurement direction. In order to enhance the pinning from bottom FePt layer and avoid the formation of spiral domain wall in NiO, we decreased the NiO spacer thickness to 2 nm. It is known that magnetic ordering temperature of AFM thin films strongly decrease as the film thickness decrease.^{33,34} For the case of NiO thin film, the Néel temperature going from 520 K for the bulk to 295 K for 5 monolayer film has been reported.³⁵ Therefore, the NiO spacer of 2 nm used in this work should keep the AFM order at RT. In addition, the measurement sequence was randomly arranged to eliminate the contribution from possible training effect. As seen in Fig 5-6c, with increasing the angle α , both remanent magnetization and coercive field show strong tendency to decrease, indicates the in-plane anisotropy of upper FePt layer. Then the data was quantitatively analyzed. For spin flop coupling configuration, as explained in last paragraph, the induced in-plane anisotropy in upper FePt layer is mainly related to the projection of net magnetic moment generated from AFM spins. In the following, we will focus on this in-plane component. Since the NiO spacer shows twelvefold symmetry around film normal direction, twelve equivalent in-plane components of AFM net moment can be expected. Each direction is perpendicular to one of six easy axis directions in the NiO($\bar{1}\bar{1}1$) plane. The idea is

that the in-plane FC could induce a modification of Ni spin structure,¹⁹ leading to those twelve components tend to be along two directions (stable contribution), which are close to the FC direction as shown in Fig 5-6b. Meanwhile, an increase for the in-plane projection can also be expected. Due to the thermal fluctuation at RT, another contribution from randomly distributed in-plane components (unstable contribution) should also exist. Based on this idea, the remanent magnetization of upper FePt layer should follow the expression

$$I_r = \frac{2b}{\pi} \int_0^{\pi} I_s \cos \alpha d\alpha + \frac{c}{2} I_s \left[\cos \left(\alpha - \frac{\pi}{6} \right) + \cos \left(\alpha + \frac{\pi}{6} \right) \right] \quad (5.1)$$

where I_r and I_s are remanent magnetization and saturation magnetization, respectively; α denotes the angle between measurement and direction of the field during in-plane FC; b and c are the portion of induced anisotropy from stable and unstable contribution, respectively. By fitting the data in Fig 5-6c (square symbol), we find that Eq. (5.1) well describe the experimental data. The b and c values obtained from data fitting are 90% and 11%, respectively. Notice that the sum of b and c values is 1% larger than unit. Since the perpendicular Fe magnetization in bottom FePt layer slightly deviate from film normal direction, this discrepancy may be attributed to the in-plane projection of bottom Fe magnetization.

5.6 Magnetic domain imaging for FePt_{Oop}/NiO/FePt_{Ip} structure

The magnetic domain structure of FePt_{Oop}(4.5 nm)/NiO(4 nm) bilayers and FePt_{Oop}(4.5 nm)/NiO(4 nm)/FePt_{Ip}(3.5 nm) trilayers was studied by magnetic force microscopy (MFM) at RT. For FePt_{Oop}/NiO/FePt_{Ip} trilayers, the in-plane magnetization of ultrathin upper FePt layer generates a fairly weak stray field, which is hardly detected by the magnetized tip. Thus, it is reasonable to expect that the

observed domain structure is from the bottom FePt layer. As shown in Fig 5-7a, the FePt_{Oop}/NiO bilayers exhibit stripe domain structure with random alignment, which is the feature of out-of-plane aligned magnetization. With the deposition of upper disordered FePt layer, no significant change can be observed unless a minute decrease of stripe width from approximately 147 nm to 134 nm [Fig. 6(b)]. To study the effect of the modification of AFM spin structure on domain structure, we performed in-plane FC on the sample of S3. Note that the FC temperature (525 K) is well below the reported Curie temperature (700 K) of partially ordered FePt film.³⁶ Thus, regardless

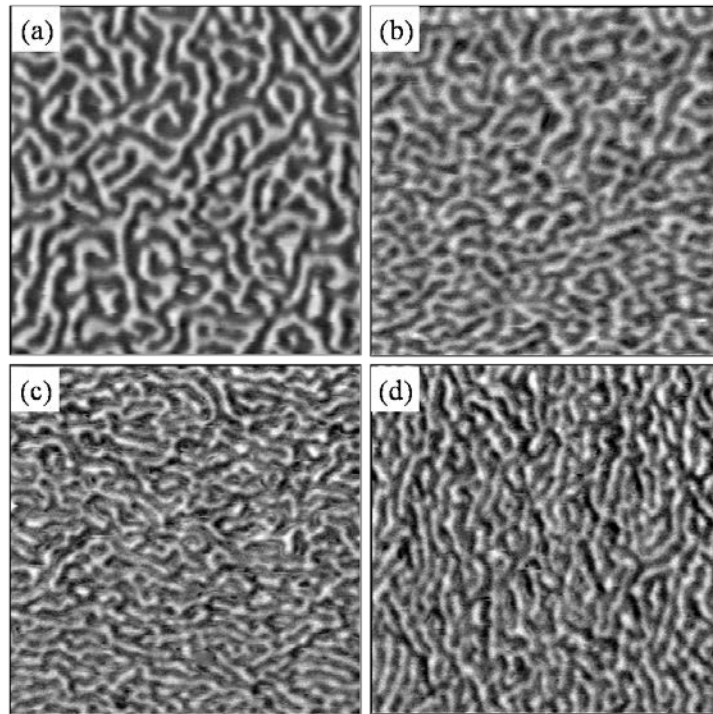


FIG 5-7 Magnetic domain structure at remanence in (a) FePt_{Oop}(4.5 nm)/NiO(4 nm) (S1) bilayers, (b) FePt_{Oop}(4.5 nm)/NiO(4 nm)/FePt_{Ip}(3.5 nm) (S3) trilayers. (c) Image of FePt_{Oop}(4.5 nm)/NiO(4 nm)/FePt_{Ip}(3.5 nm) trilayers after in-plane FC. (d) Rotating the scanning direction of (c) around film normal direction by 90°.

of influence from NiO spacer and upper FePt layer, the FC treatment should have no effect on domain structure of bottom FePt layer. Figure 5-7c shows domain structure of bottom FePt layer in FePt_{Oop}/NiO/FePt_{Ip} trilayers after in-plane FC. It is clearly

seen that the stripes tend to be parallel to the direction of the field during FC. After rotating the scanning direction around MgO [001] axis by 90°, the alignment of stripe structure also changes its direction by 90°, which is a strong indication that the Fe magnetization slightly deviate from film normal direction. Moreover, comparing with the as grown FePt_{Oop}/NiO/FePt_{Ip} trilayers, the stripe width decreases to an even smaller value (107 nm). Taking into account the FM/AFM spin flop coupling configuration used in this work, the observed decrease of stripe width can be well explained. For the sample of S3, the in-plane Fe magnetization in upper FePt layer aligns the AFM spin of NiO slightly closer to the film plane. Consequently, the in-plane component of net magnetic moment generated from AFM spins will be enhanced. It is known that an in-plane magnetization in coupled magnetic layers leads to a decrease of perpendicular magnetic anisotropy in the other layer, in which the magnetization is out-of-plane aligned.³⁷ Therefore, compared with the case of FePt_{Oop}/NiO bilayers, it is not surprising for the decrease of stripe width in FePt_{Oop}/NiO/FePt_{Ip} trilayers. As discussed in proceeding section, the in-plane FC could results in a further enhancement of in-plane projection from AFM spins. This explains why the modification of AFM spin structure in NiO spacer through in-plane FC could affect the stripe width in bottom FePt layer.

5.7 Summary

In summary, we have studied structural and magnetic properties of FePt_{Oop}/NiO/FePt_{Ip} trilayer structure, where the bottom and upper FePt layer are partially ordered and disordered, respectively. Magnetic hysteresis loop measurement shows that the Fe magnetization in upper FePt layer is in the film plane, while that in bottom layer is parallel to the film normal. This feature gives rise to a “naturally” 90°

interlayer coupling, regardless of NiO spacer. The merit of our study is that we only modify the NiO spin structure through FC to affect the magnetic behavior of two FM layers. For as grown FePt_{Oop}/NiO/FePt_{Ip} trilayers, the upper FePt layer exhibits an in-plane isotropy. However, after in-plane FC, we find that the remanent magnetization is dependent on the measuring angle relative to the FC direction, which is an indication of in-plane anisotropy. Realizing the effect on upper FePt layer, the bottom FePt layer was further studied by magnetic domain imaging. After in-plane FC, the stripe domain shows realignment and tends to be parallel to the FC direction, confirming the existence of small deviation angle of Fe magnetization from film normal direction. While a decrease of stripe width can also be observed. In consideration of FM/AFM interaction, the interesting results observed in this work can be well explained by spin flop coupling configuration, in which the angle between FM and AFM spin is not exact 90°.

References

- ¹W. H. Meiklejohn and C. P. Bean, Phys. Rev. **102**, 1413 (1956).
- ²D. Mauri, H. C. Siegmann, P. S. Bagus, and E. Kay, J. Appl. Phys. **62**,3047 (1987).
- ³A. P. Malozemoff, Phys. Rev. B **35**, 3679 (1987).
- ⁴N. C. Koon, Phys. Rev. Lett. **78**, 4865 (1997).
- ⁵R. L. Stamps, J. Phys. D **33**, R247 (2000).
- ⁶M. D. Stiles and R. D. McMichael, Phys. Rev. B **59**, 3722 (1999).
- ⁷Wondong Kim, E. Jin, J. Wu, J. Park, E. Arenholz, A. Scholl, Chanyong Hwang, and Z. Q. Qiu, Phys. Rev. B **81**, 174416 (2010).
- ⁸J. Li, A. Tan, S. Ma, R. F. Yang, E. Arenholz, C. Hwang, and Z. Q. Qiu, Phys. Rev. Lett. **113**, 147207 (2014).
- ⁹J. Wu, J. S. Park, W. Kim, E. Arenholz, M. Liberati, A. Scholl, Y. Z. Wu, Chanyong Hwang, and Z. Q. Qiu, Phys. Rev. Lett. **104**, 217204 (2010).
- ¹⁰Q. Li, G. Chen, T. P. Ma, J. Zhu, A. T. N'Diaye, L. Sun, T. Gu, Y. Huo, J. H. Liang, R. W. Li, C. Won, H. F. Ding, Z. Q. Qiu, and Y. Z. Wu, Phys. Rev. B **91**, 134428 (2015).
- ¹¹J. Li, Y. Meng, J. S. Park, C. A. Jenkins, E. Arenholz, A. Scholl, A. Tan, H. Son, H. W. Zhao, Chanyong Hwang, Y. Z. Wu, and Z. Q. Qiu, Phys. Rev. B **84**, 094447 (2011).
- ¹²Bo-Yao Wang, Jhen-Yong Hong, Kui-Hon Ou Yang, Yuet-Loy Chan, Der-Hsin Wei, Hong-Ji Lin, and Minn-Tsong Lin, Phys. Rev. B **110**, 117203 (2013).
- ¹³A. Tan, J. Li, C. A. Jenkins, E. Arenholz, A. Scholl, C. Hwang, and Z. Q. Qiu, Phys. Rev. B **88**, 104404 (2013).
- ¹⁴J. S. Moodera, L. R. Kinder, T. M. Wong, and R. Meservey, Phys. Rev. Lett. **74**, 3273 (1995).

- ¹⁵Z. Y. Liu and S. Adenwalla, Phys. Rev. Lett. **91**, 037207 (2003).
- ¹⁶P. A. A. van der Heijden, C. H. W. Swüste, W. J. M. de Jonge, J. M. Gaines, J. T. W. M. van Eemeren, and K. M. Schep, Phys. Rev. Lett. **82**, 1020 (1999).
- ¹⁷J. Camarero, Y. Pennec, J. Vogel, M. Bonfim, S. Pizzini, F. Ernult, F. Fettar, F. Garcia, F. Lançon, L. Billard, and B. Dieny, Phys. Rev. Lett. **91**, 027201 (2003).
- ¹⁸J. Wu, J. Choi, A. Scholl, A. Doran, E. Arenholz, Y. Z. Wu, C. Won, Chanyong Hwang, and Z. Q. Qiu, Phys. Rev. B **80**, 012409 (2009).
- ¹⁹W. Zhu, L. Seve, R. Sears, B. Sinkovic, and S. S. P. Parkin, Phys. Rev. Lett. **86**, 5389 (2001).
- ²⁰H. Ohldag, A. Scholl, F. Nolting, S. Anders, F. U. Hillebrecht, and J. Stöhr, Phys. Rev. Lett. **86**, 2878 (2001).
- ²¹N. J. Gökemeijer, J. W. Cai, and C. L. Chien, Phys. Rev. B **60**, 3033 (1999).
- ²²I. P. Krug, F. U. Hillebrecht, M. W. Haverkort, A. Tanaka, L. H. Tjeng, H. Gomonay, A. Fraile-Rodríguez, F. Nolting, S. Cramm, and C. M. Schneider, Phys. Rev. B **78**, 064427 (2008).
- ²³G. A. Slack, J. Appl. Phys. **31**, 1571 (1960).
- ²⁴Tenghua Gao, Nobuhide Itokawa, Jian Wang, Youxing Yu, Takashi Harumoto, Yoshio Nakamura, and Ji Shi, Phys. Rev. B **94**, 054412 (2016).
- ²⁵R. A. McCurrie and P. Gaunt, Philos. Mag. **13**, 567 (1966).
- ²⁶E. Sallica Leva, R. C. Valente, F. Martínez Tabares, M. Vásquez Mansilla, S. Roshdestwensky, and A. Butera, Phys. Rev. B **82**, 144410 (2010).
- ²⁷W. N. Cao, J. Li, G. Chen, J. Zhu, C. R. Hu, and Y. Z. Wu, Appl. Phys. Lett. **98**, 262506 (2011).
- ²⁸C. H. Lai, T. Ming, R. Erwin, and J. Borchers, J. Appl. Phys. **91**, 7751 (2002).
- ²⁹P. Luches, S. Benedetti, A. di Bona, and S. Valeri, Phys. Rev. B **81**, 054431 (2010).

- ³⁰G. Scholten, K. D. Usadel, and U. Nowak, *Phys. Rev. B* **71**, 064413 (2005).
- ³¹J. Camarero, Y. Pennec, J. Vogel, S. Pizzini, M. Cartier, F. Fettar, F. Ernult, A. Tagliaferri, N. B. Brookes, and B. Dieny, *Phys. Rev. B* **67**, 020413 (R) (2003).
- ³²M. Finazzi, M. Portalupi, A. Brambilla, L. Duò, G. Ghiringhelli, F. Parmigiani, M. Zacchigna, M. Zangrando, and F. Ciccacci, *Phys. Rev. B* **69**, 014410 (2004).
- ³³P. J. van der Zaag, Y. Ijiri, J. A. Borchers, L. F. Feiner, R. M. Wolf, J. M. Gaines, R. W. Erwin, and M. A. Verheijen, *Phys. Rev. Lett.* **84**, 6102 (2000).
- ³⁴M. W. Haverkort, S. I. Csiszar, Z. Hu, S. Altieri, A. Tanaka, H. H. Hsieh, H.-J. Lin, C. T. Chen, T. Hibma, and L. H. Tjeng, *Phys. Rev. B* **69**, 020408 (2004).
- ³⁵D. Alders, L. H. Tjeng, F. C. Voogt, T. Hibma, G. A. Sawatzky, C. T. Chen, J. Vogel, M. Sacchi, and S. Iacobucci, *Phys. Rev. B* **57**, 11623 (1998).
- ³⁶S. Okamoto, N. Kikuchi, O. Kitakami, T. Miyazaki, Y. Shimada, and K. Fukamichi, *Phys. Rev. B* **66**, 024413 (2002).
- ³⁷Y. Z. Wu, C. Won, A. Scholl, A. Doran, H. W. Zhao, X. F. Jin, and Z. Q. Qiu, *Phys. Rev. Lett.* **93**, 117205 (2004).

Chapter 6 Conclusions

The ferromagnetic (FM)/antiferromagnetic (AFM) interfacial coupling especially at compensated AFM interface has been studied in $L1_0$ FePt based ultrathin structures. To accomplish this objective, the influential factors (e.g., internal stress) for FePt ordering phase transformation were firstly investigated by introducing nitrogen gas during FePt deposition. With the well understanding of FePt ordering process, we have successfully fabricated perpendicular exchanged biased FePt/NiO bilayer structure with high structural quality. Comparing three different structures: FePt single layer, FePt/NiO bilayers before and after field cooling, we find that the angle between FM and AFM spin at compensated AFM interface may be not exact 90° . Taking into account the favorable FM/AFM coupling configuration, the obtained experimental results and origin of exchange bias can be well understood through our proposed AFM spin canting mechanism. To further verify this finding, we designed a special FePt_{Oop}/NiO/FePt_{Ip} trilayer structure, in which the bottom and upper FePt layer are partially ordered and disordered, respectively, giving rise to a “naturally” 90° FM interlayer coupling configuration. By performing an in-plane field cooling to modify the Ni spin, the magnetic behavior changes on both FePt layers have been observed. Through this approach, it offers a sensitive way to study the FM/AFM coupling.

For each $L1_0$ based FePt ultrathin structure, the detail results and main findings are summarized as follows:

6.1 The FePt/AlN multilayer structure

The preferred growth orientation and ordering of FePt has been controlled

through introducing interstitial nitrogen atoms during FePt deposition. In both two cases, i.e., the FePt deposited with and without N, the FePt layers show strong (111) texture and the crystallinity is improved with increasing annealing temperature. However, compared with these two cases, for the FePt deposited with N, it exhibits a weaker (111) texture and experiences much more in-plane compressive strain during grain growth, e.g., at 600°C the calculated strain is -1.22% and -0.26% for the FePt deposited with and without N, respectively. Taking into account the grain-orientation-specific driving forces for grain growth, the stress condition will definitely affect the preferred growth orientation of the film. In this viewpoint, a decrease in the driving force for the (111) grain growth can be expected in the case of FePt deposited with N.

For the FePt deposited without N, as the annealing temperature increases from 500 to 700°C, the degree of order rapidly increases from 0.337 to 0.743, which shows the same tendency as annealing temperature-dependent coercivity. Making comparison with FePt deposited with N, for the film annealed at 500 or 600°C, it shows a larger coercive field, indicating a more pronounced ordering in this case. Since the ordering transformation is a recrystallization process, same as (111) texture evolution, a decrease of driving force is supposed to be the reason for the weaker ordering of FePt deposited N.

6.2 The FePt/NiO bilayer structure

The perpendicular exchanged biased FePt/NiO bilayer structure has been successfully established. After perpendicular field cooling (FC), for Fe(2.5 nm)/NiO(21 nm) film the exchange field is -41 Oe at RT and increases to -301 Oe at 20 K. Besides, this bilayer structure shows interesting structural features. For FePt layer, it is well epitaxially grown on MgO(001) single crystal substrate with a strong

(001) texture. While the NiO layer exhibits a strong (111) texture and twined microstructures in the film plane, which experiences in-plane anisotropic strain. This stress condition is considered to give rise a compensated AFM interface in FePt/NiO bilayer structure.

Through performing initial magnetization curve measurement and magnetic domain imaging, the results show that for as grown bilayer structure, the FePt layer experiences a small-angle magnetization rotation when it is magnetized near to saturation in film normal direction. After field cooling, the bilayer structure shows a significant enhancement of perpendicular magnetic anisotropy, indicating the field mediated coupling between the spins across FePt/NiO interface. According to Koon's theoretical calculation on the basis of lowest energy ferromagnetic/antiferromagnetic coupling configuration for compensated spins at antiferromagnetic side, the Ni spins at the interface is considered to slightly deviate off the $(\bar{1}\bar{1}1)$ easy plane. Consequently, this spin configuration stabilizes the coupling between FePt and NiO and result in the observed exchange bias. This consideration was further confirmed by stripe domain width calculation.

6.3 FePt/NiO/FePt trilayer structure

A ferromagnetic interlayer coupled FePt/NiO/FePt trilayer structure has been fabricated, in which the bottom and upper FePt layer are partially ordered and disordered, respectively. Owing to the strong perpendicular magnetic anisotropy for ordered FePt and dipolar anisotropy for disordered FePt, this structure shows interesting features that regardless of antiferromagnetic (NiO) layer, it gives rise to a “naturally” 90° ferromagnetic interlayer coupling. From structural characterization, it is noticed that the bottom FePt layer is well epitaxially grown on MgO(001) substrate

with (001) texture, whereas the upper FePt exhibits the same crystallographic orientation as NiO layer.

Performing field cooling to only modify the NiO spin structure, the corresponding effects on two FePt layers were studied. For upper FePt layer, the in-plane field cooling induces an in-plane magnetic anisotropy, showing a dependence of remanent magnetization on the angle between the directions of the measurement and the field during field cooling, which is not observed in as grown trilayers. It is worth noting that this interesting phenomenon also cannot be observed in FePt/NiO/FePt trilayers with two disordered FePt layers. For bottom FePt layer, after in-plane field cooling, the magnetic stripe domain changes from random distribution to a tendency of aligning along the direction of the field during field cooling with decreased stripe width. In the viewpoint of coupling at FePt/NiO interface, the underlying mechanism of observed results can be well explained by the FM/AFM coupling configuration proposed from FePt/NiO bilayer structure.

Publications

- **Tenghua Gao**, Cong Zhang, Takumi Sannomiya, Shinji Muraishi, Yoshio Nakamura, and Ji Shi, “Effect of nitrogen upon structural and magnetic properties of FePt in FePt/AlN multilayer structures”, *J. Vac. Sci. Technol. A* **32**, 051506 (2014).
- Lei Wang, **Tenghua Gao**, and Youxing Yu, “Effects of Ag addition on FePt L1₀ ordering transition: A direct observation of ordering transition and Ag segregation in FePtAg alloy films”, *J. Appl. Phys.* **118**, 235304 (2015).
- **Tenghua Gao**, Nobuhide Itokawa, Jian Wang, Youxing Yu, Takashi Harumoto, Yoshio Nakamura, and Ji Shi, “Off-easy-plane antiferromagnetic spin canting in coupled FePt/NiO bilayer structure with perpendicular exchange bias”, *Phys. Rev. B* **94**, 054412 (2016).
- **Tenghua Gao**, Takashi Harumoto, Yoshio Nakamura, and Ji Shi, “Field cooling Driven magnetic anisotropy and strip domain evolution in FePt/NiO/FePt trilayer structure”, (To be published)

Conference Presentations

- **Tenghua Gao**, Yoshio Nakamura, and Ji Shi, “Effect of nitrogen upon structural and magnetic properties of FePt in FePt/AlN multilayer structures”, The 52th Autumn Meeting of Japan Electronic Materials Society. Nov. 13, 2015. Tokyo, Japan. Oral
- **Tenghua Gao**, Yoshio Nakamura, and Ji Shi, “Impact of stress on texture evolution and ordering transformation of FePt in FePt/AlN multilayer film by N

addition”, The 20th International Vacuum congress. Aug. 21-26, 2016. Busan, Korea. Oral

- **Tenghua Gao** Takashi Harumoto, Yoshio Nakamura, and Ji Shi, “Spin interaction induced in-plane magnetic anisotropy of soft magnetic FePt layer in FePt/NiO/FePt trilayer structure”, The 61th Annual Conference on Magnetism and Magnetic Materials. Oct. 31, - Nov. 4, 2016. New Orleans Marriott, New Orleans, USA. Poster (Accepted)

Acknowledgements

First and foremost I would like to thank my advisor, Professor J. Shi, whose support and guidance made me pass through the rough road to finish this thesis. During the journey on my own research, he was always available to advise me and gave me all the support on my experiment. His patience, encouragement and knowledge on magnetism and material science inspired me to move on. I will not forget that before the doctoral dissertation defense he help me practice my presentation again and again, and gave me much good advice for the improvement. Thanks to him I had the opportunity to study and finish my doctoral work in Tokyo Institute of Technology. I would also like to thank my advisor, Professor Y. Nakamura for providing me patient discussions and insightful suggestions on my research. His immense knowledge on the characterization of crystal structure was the light in the dark, helping me overcome the obstacles.

I would like to thank Assistant Professor T. Harumoto for the help with my experiment and sharing his knowledge on the x-ray diffraction analysis and TEM observation, which made me learn a lot.

I am very thankful to Professor S. Nakagawa, Associate Professor S. Muraishi, and Associate Professor T. Sannomiya for being my thesis committee and giving me much good advice to improve my doctoral thesis.

Thanks to Dr. J. Wang for teaching me using the instrument and giving me support for the SQUID measurements. Thanks to Dr. C. Zhang for helping me adapt my life in Japan. Special thanks to Mr. N. Itokawa, the partner of my research subject, for his effort on experiment. Also, thanks to all the present and past members of Nakamura-Shi lab for their kindness and providing a great working environment.

I would like to thank Professor A. Nishikata and Associate Professor E. Tada for allowing me to use their MFM instrument. Thanks also go to Mr. Y. Suzuki of the center for advanced materials Analysis for his help and support in using D8 Discover x-ray diffraction instrument.

Finally, in particular, I would like to express my gratitude to my parents for their love, understanding and support. I dedicate this thesis to the memory of my grandmother, whose role in my life was, and remains immense. The last word of acknowledgement is for my wife, who came to Japan for me three years ago, away from her family and friends. She trusted in me even in my tough days, which gave me confidence to accomplish this work.